

TECHNISCHE
UNIVERSITÄT
MÜNCHEN

WALTHER-
MEISSNER-
INSTITUT

BAYERISCHE
AKADEMIE DER
WISSENSCHAFTEN

**Vertical Pt/Y₃Fe₅O₁₂/Pt
Heterostructures for Magnon
Mediated Magnetoresistance
Measurements**

Master's thesis
Philipp Schwenke

Supervisor: Prof. Dr. Rudolf Gross

Advisors: Dr. Stephan Geprägs

Garching – November 3, 2021

Contents

1. Introduction	1
2. Theoretical background	3
2.1. Spin currents	3
2.2. Spin Hall effect	3
2.3. Angle dependent magnetoresistance	4
2.3.1. Spin Hall magnetoresistance	5
2.3.2. Magnon-mediated magnetoresistance	7
2.3.3. Anisotropic magnetoresistance	8
2.4. Spin Seebeck effect	9
2.5. Ferromagnetic resonance	10
2.6. Pt/Y ₃ Fe ₅ O ₁₂ /Pt Heterostructures	11
3. Sample fabrication	13
3.1. Optical lithography	13
3.2. Ar-ion milling	15
3.3. Lift-off process	17
4. Fabrication of patterned Pt/Y₃Fe₅O₁₂/Pt heterostructures	19
4.1. Fabrication of patterned Pt/Y ₃ Fe ₅ O ₁₂ /Pt heterostructures by etching	19
4.2. Fabrication of Pt/YIG/Pt heterostructures by using a lift-off technique for the Pt and the YIG layers	21
4.3. Fabrication of Pt/YIG/Pt heterostructures by using a lift-off technique solely on the Pt layers	23
4.3.1. Magnetic properties	29
4.3.2. Magnetotransport properties	33
4.4. Conclusion	36
5. Optimization of the bottom Pt layer	39
5.1. Minimizing interdiffusion between Pt and Y ₃ Fe ₅ O ₁₂ by Ru buffer layers	39
5.1.1. Ru buffer layer between the YIG and the bottom Pt layer	39
5.1.2. Additional Ru buffer layer between YAG and Pt	44
5.2. Addressing electrical shorts between the bottom and top Pt layers	49
5.2.1. Increasing the thickness of the YIG layer	49
5.2.2. Reducing the lateral area of the bottom and top Pt layers	52

5.3. Conclusion	58
6. Magnon-mediated magnetoresistance measurements	59
6.1. Magnon-mediated magnetoresistance measurements on the Pt/YIG/Pt heterostructure with short Pt strips	59
6.2. Magnon-mediated magnetoresistance measurements on Pt/YIG/Ru/Pt heterostructures	63
6.3. Magnon-mediated magnetoresistance measurements on a Pt/YIG bilayer	64
6.4. Conclusion	66
7. Summary and outlook	67
7.1. Summary	67
7.2. Outlook	69
A. Appendix	71
A.1. List of samples	71
A.2. Current reversal method	72
A.3. Deposition techniques	72
A.3.1. Pulsed laser deposition (PLD)	72
A.3.2. Electron beam evaporation (EVAP)	73
A.3.3. Magnetron sputtering	73
A.4. Analysis methods	74
A.4.1. X-ray diffraction	74
A.4.2. Atomic force microscopy	77
A.4.3. Electron-beam lithography	78
A.4.4. SQUID-magnetometry	78
A.4.5. Ferromagnetic resonance (FMR) measurements	79
Bibliography	81
Acknowledgments	90

1. Introduction

The access to knowledge has never been easier than nowadays. This is made possible by the world wide web and the wide spread of computers and smartphones. These devices however are only possible due to the invention of transistors about 70 years ago [1] as well as their steady miniaturization leading to an ever more increasing amount of transistors on the same area, which is described by Moore's law [2]. However, this results in more heat generation due to Joule heating. Moreover, the lower physical limit of these components is soon reached [3]. Thus, alternative and complementary approaches need to be investigated. One way to overcome these issues might be by using electronic devices exploiting the spin of electrons in addition to the charge degree of freedom [4, 5]. For data storage this is already done in e.g. hard disc drives exploiting the giant magnetoresistance (GMR) [6, 7] to precisely read out spin densities [8]. The research field investigating such devices is called spintronics.

In the field of spintronics not only the charge current based solely on moving electrons are used, but we also account for the spin of the electrons. Therefore, spin currents can be created without the effective movement of electrical charges. These spin currents are not currents in the traditional sense of moving electric charges, but rather of moving angular momentum. Thus, spin currents can even be transported in magnetically ordered, electrical insulators via magnons, which are the fundamental magnetic excitation of magnetically ordered materials. This allows for information processing without charge currents and therefore might reduce heating effects. Such magnons can be created by microwave radiation, which leads to a precession of the magnetization [9, 10]. This precession can emit a spin current in heavy metal/magnetically ordered insulator heterostructures via a spin pumping process. Another way to create magnons is by applying a charge current in a heavy metal like platinum (Pt), which creates a spin current via the spin Hall effect (SHE) [11–15]. This in turn excites non-equilibrium magnons in an adjacent magnetically ordered insulator, which can diffuse into the insulator and can be detected at an electrically separated Pt layer via the inverse spin Hall effect (iSHE) [16]. This process results in the so called magnon-mediated magnetoresistance (MMR) [17]. The materials of choice for observation of the MMR are the heavy paramagnetic metal platinum (Pt) and yttrium iron garnet ($\text{Y}_3\text{Fe}_5\text{O}_{12}$, YIG) due to the very low magnetic damping of spin waves [18] and thus long range magnon transport [17, 19]. The MMR was already observed in Pt/YIG bilayers using a horizontal two strip design, where one strip serves as magnon injector and the other as magnon detector [17, 20]. Moreover, the MMR has been modulated by an additional Pt strip (modulator) in between the Pt injector and detector strip [21–23], which

even created a region with zero effective damping [24]. These devices are functional at room temperature [25] and could therefore be used for logic operations [26, 27] or other applied applications. In such structures the distance between the electrodes is always important due to the damping of the magnons and therefore the magnon diffusion length [28, 29]. Therefore, it might be of interest to put the modulator strip underneath the YIG layer for further miniaturization and optimization of such devices. Moreover, this would allow for more design choices and smaller distances between the magnon injector and detector.

Therefore, the goal of this thesis is to establish a fabrication process for vertical Pt/YIG/Pt heterostructures and in the future, possibly different materials, which are suitable for MMR measurements. To this end, a lift-off technique for thin films fabricated via pulsed laser deposition (PLD), where molecules with high kinetic energy hit the photoresist layer, is developed. This opens up multiple possibilities to fabricate more complex structures using PLD processes.

This thesis is organized as follows: In Chapter 2 the theoretical foundations necessary to understand this thesis are introduced. This consists of the introduction to pure spin currents, different magnetization dependent resistance effects and magnetization dynamics. Chapter 3 describes the fabrication of the samples by optical lithography with the laser writer system PicoMaster 200 on optically transparent substrates. Moreover, the concept of Ar-ion milling and lift-off are discussed. The vertical Pt/YIG/Pt heterostructures are realized in Chapter 4 and investigated regarding structural and magnetic properties. Chapter 5 tackles the optimization of the bottom YIG/Pt interface and encountered issues regarding electrical properties. The results of the magnon-mediated magnetoresistance measurements on the fabricated heterostructures are discussed in Chapter 6. This thesis finishes with Chapter 7, which briefly summarizes the most important results and gives an outlook over further research possibilities.

2. Theoretical background

In this chapter the theoretical background of spin-current based experiments performed in the framework of this thesis is discussed. Thus, the concept of pure spin currents is introduced as well as the spin Hall effect and the spin Seebeck effect as methods for generating these spin currents. Moreover, an overview of the spin Hall-, anisotropic- as well as magnon-mediated magnetoresistance is given with their corresponding dependence on the magnetization direction of a ferrimagnetic layer. Finally, recently published results on Pt/Y₃Fe₅O₁₂/Pt heterostructures are discussed.

2.1. Spin currents

An electric current not only consists of moving charges (charge current) but also of a flow of angular momentum (spin current), which introduces an additional degree of freedom. Therefore, in a two spin channel model the electrons are divided into spin up \uparrow and spin down \downarrow electrons with respect to the quantization axis. In this model the electric charge current density \mathbf{J}_c can be written as [30]

$$\mathbf{J}_c = (\mathbf{J}_\uparrow + \mathbf{J}_\downarrow) \quad (2.1)$$

Here \mathbf{J}_\uparrow is the charge current density of spin up and \mathbf{J}_\downarrow the charge current density of spin down electrons. This allows for a spin polarization of the current if there are more spin up (\uparrow) electrons than spin down (\downarrow) electrons at the Fermi energy contributing to the total current flow. Moreover, if the charge currents \mathbf{J}_\uparrow and \mathbf{J}_\downarrow are equal in magnitude but flow in opposite directions, there are two equally large polarized currents flowing in opposite directions, the total charge current \mathbf{J}_c is zero. However, spin information is still transported in one direction, which is then called a pure spin current and can be described by [31]

$$\mathbf{J}_s = -\frac{\hbar}{2e}(\mathbf{J}_\uparrow - \mathbf{J}_\downarrow) \quad (2.2)$$

The factor $-\frac{\hbar}{2e}$ considers the angular momentum transport of \mathbf{J}_s .

2.2. Spin Hall effect

One way to create a spin current is based on the spin Hall effect (SHE). This effect is present in heavy, paramagnetic metals (HM), like Platinum (Pt). When applying a current in this

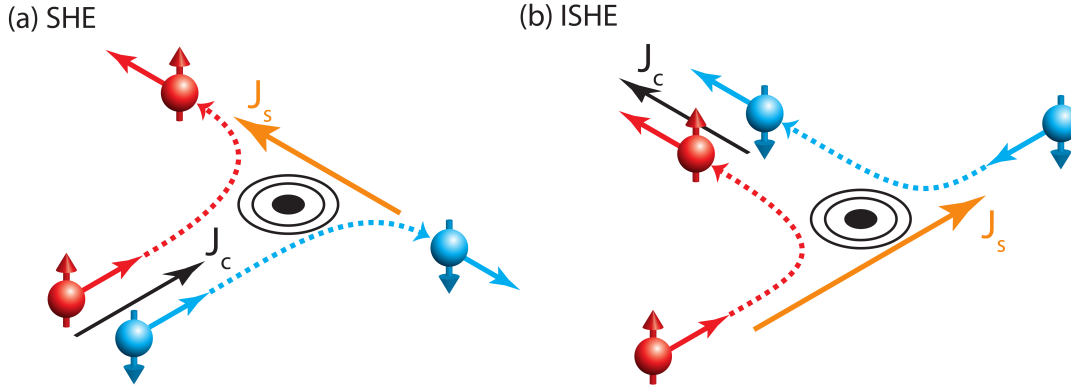


Figure 2.2.1.: Illustration of (a) the spin Hall effect (SHE), where a charge current J_c is converted into a spin current J_s . (b) shows the inverse effect (iSHE) where a charge current is converted into a charge current J_c . Figure taken from Ref. [32]

metal, the charge current J_c can be converted by [33]

$$\mathbf{J}_s = \theta_{\text{SH}} \left(\frac{\hbar}{2e} \right) \mathbf{J}_c \times \mathbf{s} \quad (2.3)$$

into a perpendicular spin current \mathbf{J}_s (see Fig. 2.2.1 (a)). θ_{SH} is the spin Hall angle, which describes the efficiency of the conversion of \mathbf{J}_c into \mathbf{J}_s and \mathbf{s} denotes the dimensionless spin polarization vector. For Pt the spin Hall angle was previously determined to $\theta_{\text{SH}} = 0.11$ [14]. The underlying physics is a spin dependent scattering of the flowing electron spins due to a sufficiently large spin-orbit coupling (SOC). The scattering processes at play originate from intrinsic bandstructure physics [34] and extrinsic effects, e.g. skew scattering or side jump scattering [35–37]. The conversion from \mathbf{J}_c to \mathbf{J}_s can also be reversed, which is then called the inverse spin Hall effect (iSHE). There a spin current \mathbf{J}_s is converted into a charge current \mathbf{J}_c (see Fig. 2.2.1 (b)) by the same mechanisms as mentioned before. This is described by

$$\mathbf{J}_c = \theta_{\text{SH}} \left(-\frac{2e}{\hbar} \right) \mathbf{J}_s \times \mathbf{s} \quad (2.4)$$

and can thus be used as detection of spin currents.

2.3. Angle dependent magnetoresistance

A magnetoresistance is the change of resistivity of a material by applying or changing a magnetic field. In this thesis different magnetoresistance effects are at play that need to be discussed. These are the spin Hall, anisotropic and magnon-mediated magnetoresistance. Due to their different dependencies of the resistivity on the magnetization direction of a magnetic material, they can be distinguished from each other.

2.3.1. Spin Hall magnetoresistance

In a heavy paramagnetic metal (HM), which is attached to a magnetic insulator, a change in resistance with respect to the magnetization M of the magnetic insulator can be observed. This is called the spin Hall magnetoresistance (SMR) [12–15, 38–40]. Since in this work

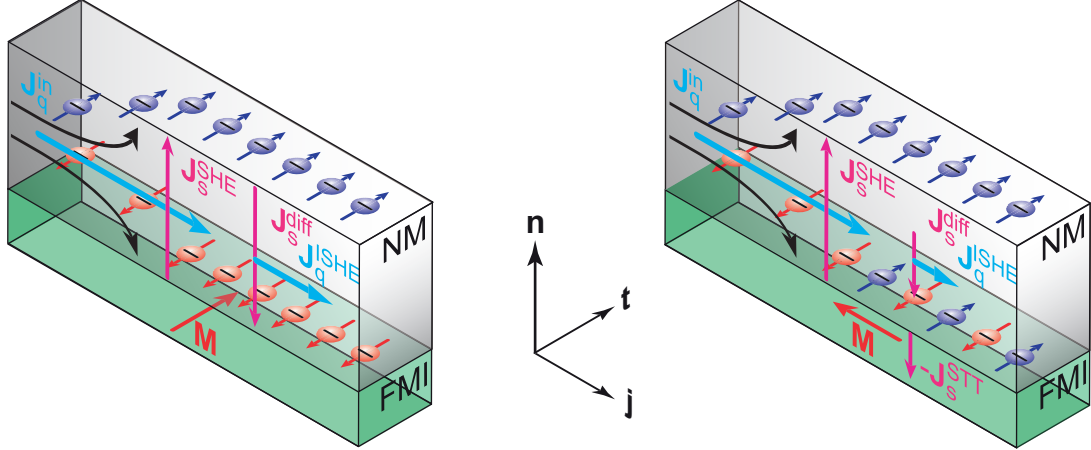


Figure 2.3.1.: Phenomenological mechanism of the spin Hall magnetoresistance. In case of a parallel alignment of the magnetization M of the FMI and the spin polarization s of the spin accumulation at the NM/FMI interface, no spin transfer torque act on the magnetic moments of the FMI, while a finite spin transfer torque is present for $M \nparallel s$. This leads to a different resistance in the NM layer depending on the magnetization direction of the FMI. Figure taken from Ref. [41].

only the ferrimagnetic insulator $Y_3Fe_5O_{12}$ is used as the magnetic insulator we restrict the discussion of the SMR on ferrimagnetic insulators (FMI). By applying a charge current in the NM, a pure spin current density J_s^{SHE} is induced perpendicular to J_c via the SHE (see Eq. 2.3). This spin current leads to a spin accumulation at the NM/FMI interface. Thus, a gradient of the spin accumulation is created, which in turn results in an opposing diffusive spin current backflow J_s^{diff} . For $M \nparallel s$, a part of the initial charge current is absorbed by the FMI via spin transfer torque on the magnetic moments in the FMI, resulting in an additional loss channel, which reduces the diffusive spin current and thus the resistance of the HM increases. However, there is no spin transfer torque on the magnetic moments for $M \parallel s$. In this case, the resistance is in first order equal to the normal resistance of the HM layer.

This leads to an distinct angle-dependence of the resistivity of the NM on the magnetization M of the adjacent FMI layer, which can phenomenologically be described by [14]

$$\rho_{\text{long}}^{\text{SMR}} = \rho_0^{\text{SMR}} + \rho_1^{\text{SMR}}(1 - m_t^2) \quad (2.5)$$

with m_t describing the projection of $\mathbf{m} = \mathbf{M}/M_s$ on \mathbf{t} with the saturation magnetization M_s . Moreover, ρ_0^{SMR} corresponds in first order to the resistivity of the bare NM and ρ_1^{SMR} is

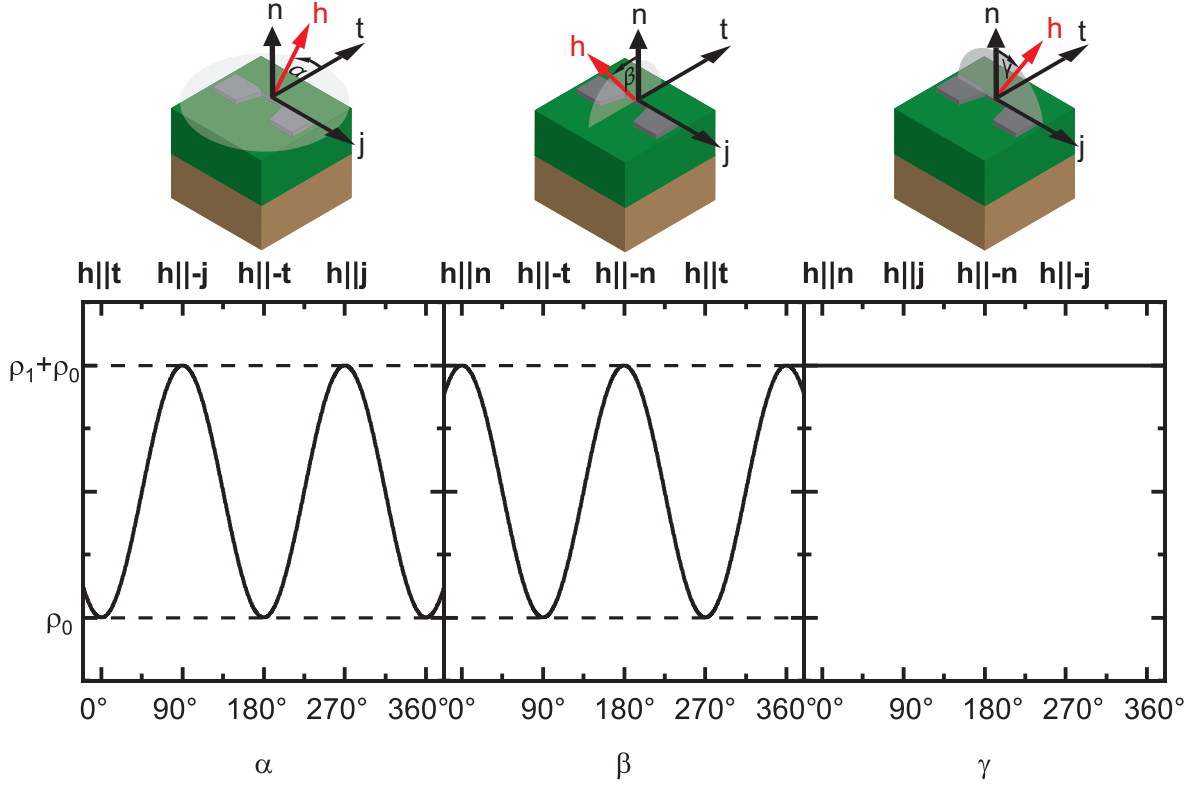


Figure 2.3.2.: Expected angle-dependence of the SMR in a NM/FMI heterostructure when rotating a magnetic field in the film plane (ip), out of the film plane perpendicular to \mathbf{j} (oopj) and out of plane perpendicular to \mathbf{t} (see top panels).

the SMR-induced change in resistivity with $\rho_1^{\text{SMR}} \ll \rho_0^{\text{SMR}}$. By using the rotation planes of the magnetic field direction \mathbf{h} shown in the top panels of Fig. 2.3.2, an angle-dependence of the resistivity of the HM layer as displayed in Fig. 2.3.2 is expected. Here, a magnetic field magnitude larger than the saturation field is assumed, such that the direction of the magnetization of the FMI is collinear to the magnetic field ($\mathbf{m} \parallel \mathbf{h}$). For the ip-rotation a $(1 - \cos^2 \alpha) = \sin^2 \alpha$ dependence on the in-plane angle α is expected. Whereas when rotating the magnetic field in the plane perpendicular to the current density direction \mathbf{j} a $\cos^2 \beta$ dependence is expected. Rotating the field in the plane perpendicular to \mathbf{t} , m_t becomes 0, which leads to a constant resistivity of $\rho_0^{\text{SMR}} + \rho_1^{\text{SMR}}$.

The relative SMR amplitude can be described by [12]

$$\frac{\Delta \rho}{\rho_0} = \frac{\theta_{\text{SH}}^2 (2l_s^2 \rho_e) (t_{\text{NM}})^{-1} g_r^{\uparrow\downarrow} \tanh^2 \left(\frac{t_{\text{NM}}}{2l_s} \right)}{\frac{\hbar}{e^2} + 2l_s \rho_e g_r^{\uparrow\downarrow} \coth \left(\frac{t_{\text{NM}}}{l_s} \right)} \quad (2.6)$$

where ρ_e is the electrical resistivity and l_s the spin diffusion length of the NM and $g_r^{\uparrow\downarrow}$ is the spin-mixing conductance. Thus the SMR is a useful tool to determine $g_r^{\uparrow\downarrow}$ if the other parameters are known [14, 42]. In this thesis, however, the SMR only serves as a characterization tool of the NM/FMI interface quality.

2.3.2. Magnon-mediated magnetoresistance

The principles of the afore-discussed spin Hall magnetoresistance are strictly speaking only valid at low temperatures, since for the magnetization configuration $\mathbf{M} \parallel \mathbf{s}$ magnons can be created or annihilated in the FMI. This leads to the magnon-mediated magnetoresistance (MMR). In order to measure an MMR, at least two electrically separated HM electrodes are necessary. One serves as a magnon injector, while the other is used as a magnon detector [17]. At the injector, a charge current \mathbf{J}_c is applied, which results in a spin accumulation

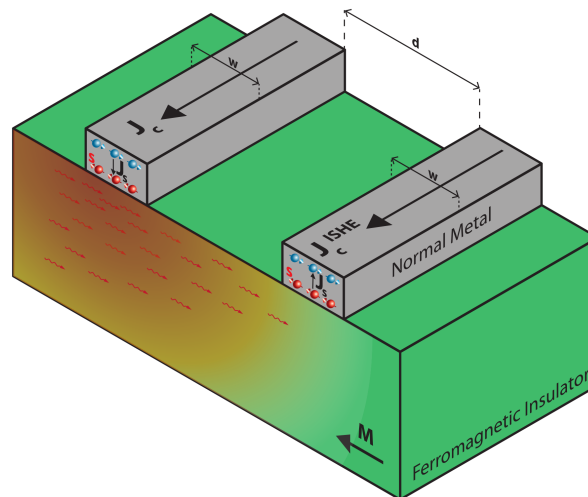


Figure 2.3.3.: Picture of a well-established two strip structure used for MMR measurements. By applying a charge current density \mathbf{J}_c through the left strip, a spin current density \mathbf{J}_s is induced perpendicular to \mathbf{J}_c and the spin polarization \mathbf{s} . \mathbf{J}_s creates a spin accumulation at the NM/FMI interface, which induces a magnon accumulation (wavy red arrows) in the FMI. This decays with increasing distance to the NM strip. In an electrically separated NM strip, the magnons can induce a spin current which is converted by the iSHE into a charge current $\mathbf{J}_c^{\text{iSHE}}$. Figure taken from Ref. [32].

at the HM/FMI interface, analogously to Chapter 2.3.1. When $\mathbf{M} \parallel \mathbf{s}$ the spin accumulation in the NM creates or annihilates magnons in the FMI, which diffuse away from the HM strip [17, 19, 43]. This effect is assumed to be small and is therefore ignored in the discussion of the SMR. However, a second HM strip nearby to the first one can detect the non-equilibrium spin accumulation at the HM/FMI interface via the iSHE creating a charge current \mathbf{J}_c (Eq. (2.4) from Chapter 2.2). For $\mathbf{M} \perp \mathbf{s}$ the charge current in the detector electrode is expected to be significantly reduced due to the spin transfer torque suppressing the spin accumulation in the injector electrode and the propagation in the FMI. Thus, the injection as well as the detection of the magnons is dependent on the angle between the magnetization of the FMI and the spin polarization at the interface. This leads to a \cos^2 dependence. Thus, rotating a magnetic field in the film plane leads to a $\cos^2 \alpha$ dependence, rotating in the oopj rotation plane gives a $\sin^2 \beta$ dependence and we do not expect any signal in the detector strip for oopt magnetic field rotations (see Fig. 2.3.4).

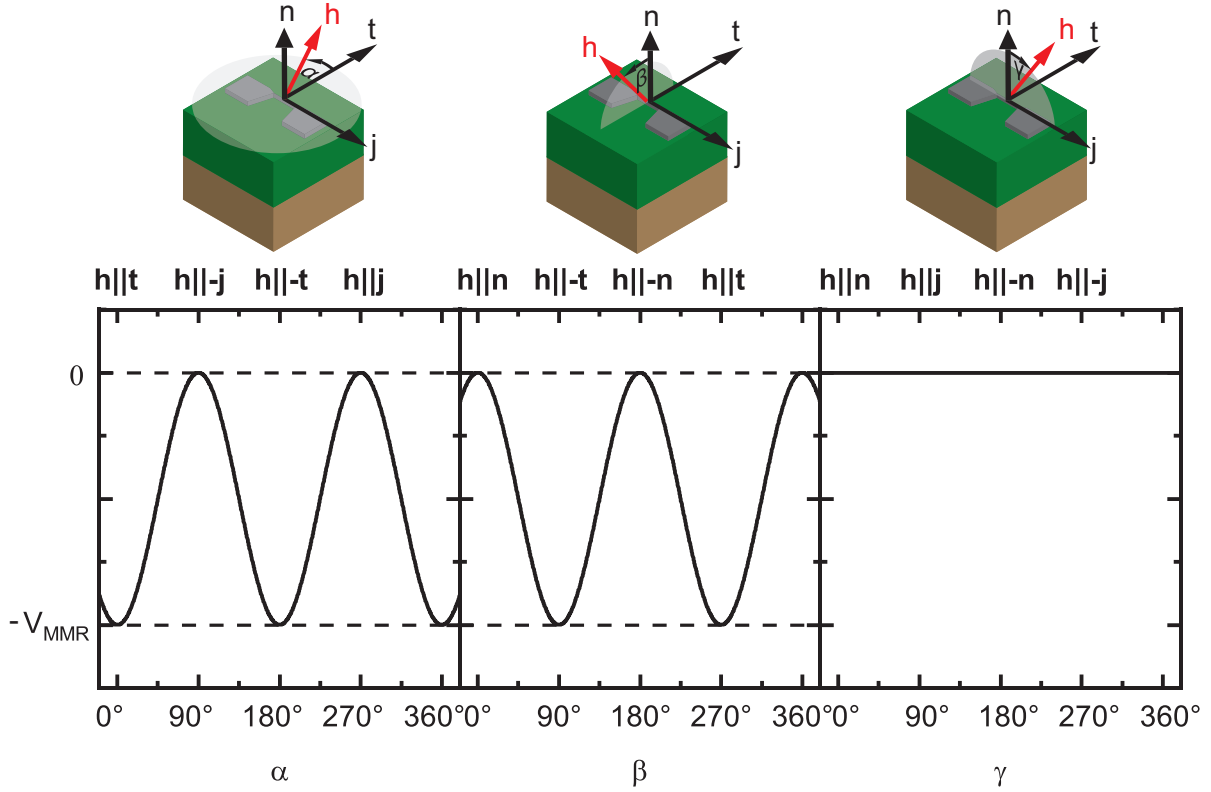


Figure 2.3.4.: Expected angle-dependence of the MMR in a two strip horizontal NM/FMI heterostructure when rotating a magnetic field in the film plane (ip) ($\cos^2 \alpha$), out of the film plane perpendicular to j (oopj) ($\cos(\beta + 90^\circ)$) and out of plane perpendicular to t (0). The rotation planes on top are defined as they are later on used in the thesis.

2.3.3. Anisotropic magnetoresistance

The anisotropic magnetoresistance (AMR) originates from partially filled d-shells in ferromagnetic metals. These are not centrosymmetric, leading to a coupling to the magnetization \mathbf{M} due to the spin-orbit coupling. Thus, the s-d scattering depends on the \mathbf{M} orientation. Since in this work we only use Pt, which is a paramagnetic metal, we do not expect an AMR in our experiments. Thus we discuss only briefly the angle dependence of this magnetoresistive effect. The longitudinal resistivity can be described by [44]

$$\rho_{\text{long}}^{\text{AMR}} = \rho_0^{\text{AMR}} + \rho_1^{\text{AMR}} m_j^2 \quad (2.7)$$

with m_j the projection of the magnetization on the current direction. ρ_0^{AMR} is given by the resistivity perpendicular (ρ_{\perp}) to \mathbf{M} . ρ_1^{AMR} can be calculated from the difference of the resistivity parallel (ρ_{\parallel}) and perpendicular (ρ_{\perp}) to \mathbf{M} as $\rho_1^{\text{AMR}} = \rho_{\parallel} - \rho_{\perp}$. Thus, the AMR can be determined by rotating a sufficiently large magnetic field. For this rotation it is obvious from Eq. (2.7) that the magnetic field should not be rotated in a plane that is perpendicular to the applied current direction for detection of an AMR. In Fig. 2.3.5 the expected angle dependence for different field rotations is shown.

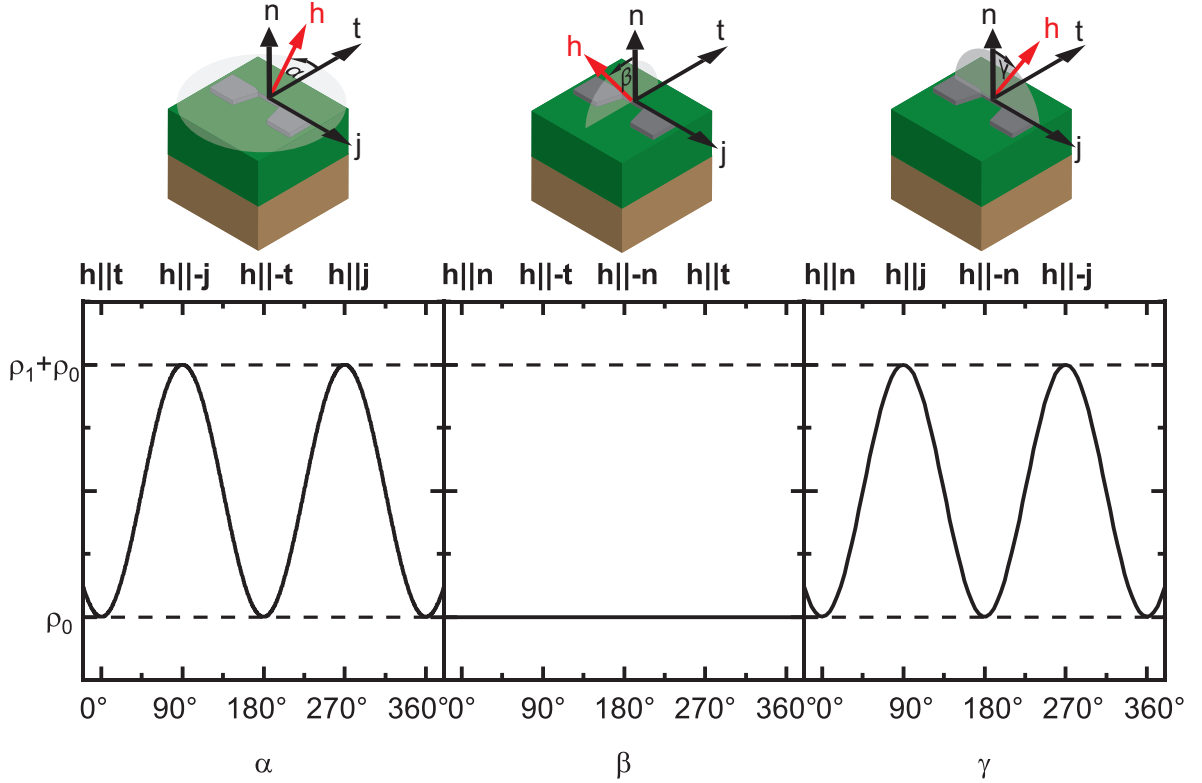


Figure 2.3.5: For the AMR a $\sin^2 \alpha$ dependence of the resistivity is expected when rotating a magnetic field in the film plane (ip). Rotating the field out of the film plane perpendicular to \mathbf{j} (oopj) gives a constant resistivity, whereas when rotating the field out of plane perpendicular to \mathbf{t} we expect again a $\sin^2 \gamma$ dependence. Schematics of the rotation planes are shown on the top panels.

2.4. Spin Seebeck effect

Up until now we ignored that a charge current is always accompanied with Joule heating due to the finite resistance of the electric lead. This creates a temperature gradient perpendicular to the NM/FMI interface, which in turn can create a spin current \mathbf{J}_s in the FMI, that is pumped into the HM layer. There it is converted into a charge current \mathbf{J}_c via the iSHE. This effect is called the spin Seebeck effect (SSE) [33, 45–48]. In this work we use a HM strip as heater and the SSE voltage induced by the arising longitudinal temperature gradient is measured at an electrically separated detection strip as discussed in Chapter 2.3.2. Thus the temperature gradient is proportional to the electric heating power

$$P_{\text{JH}} = RI_c^2 \quad (2.8)$$

with R being the resistance of the NM. The SSE follows a $\cos \alpha$ dependence, with α the angle between the magnetization \mathbf{M} and the \mathbf{t} axis, due to $\mathbf{J}_c^{\text{iSHE}} \propto \mathbf{J}_s \times \mathbf{s}$. Thus the sign changes when rotating the magnetization by $\alpha = 180^\circ$. Moreover, at $\alpha = 90^\circ$ the charge current $\mathbf{J}_c^{\text{iSHE}}$ flows perpendicular to \mathbf{j} . Thus, no voltage can be measured at this magnetization direction. Therefore, the SSE can easily be distinguished from the MMR by the

different periodicity with respect to magnetic field rotations.

2.5. Ferromagnetic resonance

Ferromagnetic resonance (FMR) experiments detect the precessional motion of the magnetization of a magnetic material, when this magnetization is oriented by an external magnetic field [9, 10, 49]. The resonance phenomena occurs, when the frequency of an external oscillating field, applied transversely is equal to the precession frequency (Lamor frequency). However, in real samples an anisotropy and demagnetization field need to be taken into account. Thus the magnetization does not precess solely around the external magnetic field \mathbf{H}_{ext} but rather around an effective field \mathbf{H}_{eff} defined by

$$\mathbf{H}_{\text{eff}} = \mathbf{H}_{\text{ext}} + \mathbf{H}_{\text{aniso}} - \mathbf{H}_{\text{demag}}. \quad (2.9)$$

Moreover, the precession will eventually stop and the magnetization align parallel to \mathbf{H}_{ext} . This magnetization dynamic is phenomenologically described by the Landau-Lifshitz-Gilbert (LLG) equation [50]

$$\frac{\partial \mathbf{m}}{\partial t} = -\mu_0 \gamma \mathbf{m} \times \mathbf{H}_{\text{eff}} + \alpha \mathbf{m} \times \frac{\partial \mathbf{m}}{\partial t} \quad (2.10)$$

with α being the Gilbert damping parameter and $\gamma = g\mu_B/\hbar$ the gyromagnetic ratio with the Landé-factor g , the Bohr magneton μ_B and the normalized magnetization vector $\mathbf{m} = \mathbf{M}/M_s$ with the saturation magnetization M_s . The precession frequency is given by

$$\omega = \gamma \mu_0 |H_{\text{eff}}|. \quad (2.11)$$

By applying an additional external oscillatory field perpendicular to \mathbf{H}_{eff} , the magnetization precession is driven by the additional torque $-\mathbf{M} \times \mathbf{h}_{\text{rf}}$. The energy absorbed is highest, when the resonance condition is met. In the case that \mathbf{H}_{eff} is applied in out of plane (oop) condition the relation between the resonant field H_{res} and the frequency f of the oscillatory field is given by the Kittel equation [9]

$$H_{\text{res}} = M_{\text{eff}} + \frac{h}{(\gamma \mu_0 \mu_B)} f. \quad (2.12)$$

The from the FMR measurement obtained data resembles a complex Lorentzian function. From this H_{res} as well as the linewidth ΔH can be extracted for each frequency of the oscillating field. From the frequency dependence of the resonance field, the g -factor as well as the effective magnetization M_{eff} can be determined by fitting the data with [51]

$$\mu_0 H_0 = f \cdot \frac{h}{g \mu_B} + \mu_0 M_{\text{eff}}. \quad (2.13)$$

Moreover, by fitting the frequency dependence of the linewidth by [51]

$$\mu_0 \Delta H = \frac{2\alpha h}{g\mu_B} \cdot f \mu_0 H_{\text{inh}} \quad (2.14)$$

the Gilbert damping α and the inhomogeneous linewidth broadening H_{inh} can be extracted. Therefore, broad-band FMR is a useful technique to determine the dynamic properties of magnetic materials and devices.

2.6. Pt/Y₃Fe₅O₁₂/Pt Heterostructures

The main task of this thesis is the fabrication of vertical HM/FMI/HM heterostructures with a high spin current transparency at the HM/FMI interfaces. In the recent years, different vertical HM/FMI/HM heterostructures have been realized including Au/Y₃Fe₅O₁₂/Au, Fe₃O₄/Pt based heterostructures as well as Pt/Y₃Fe₅O₁₂/Pt trilayers [52–55]. In this work we concentrate on Pt/Y₃Fe₅O₁₂/Pt heterostructures due to the large spin-orbit coupling of Pt and therefore high spin Hall angle as well as because of the extraordinary microwave and electric properties of Y₃Fe₅O₁₂ (YIG). In such trilayers a finite magnon-mediated magnetoresistance has been recently reported [56]. However, the fabrication of Pt/YIG/Pt trilayers is not trivial since high crystalline YIG thin films deposited on top of a Pt layer are needed with a good interface quality, which has shown to be challenging [57, 58, 62]. One promising method to fabricate Pt/YIG/Pt heterostructures is by using rapid thermal annealing to crystallize the YIG thin film, as has been shown by Nozue *et. al* [55]. This has also already been investigated at WMI and further improved [58, 62] by introducing a two step annealing process as introduced in Ref. [59]. Therefore, this is used as starting point for the fabrication of such vertical heterostructures in this thesis.

3. Sample fabrication

This chapter describes the sample fabrication via optical lithography using the laser writer system PicoMaster 200, which is optimized for optical transparent materials with only a lateral size of $5\text{ mm} \times 5\text{ mm}$ in this study. Moreover, the technique of Ar-ion milling and the lift-off process are discussed. During this study, a lift-off process is developed for pulsed-laser thin film deposition.

3.1. Optical lithography

The samples in the framework of this thesis are fabricated by multiple steps of optical lithography, different deposition techniques as well as lift-off and Ar-ion etching processes. Arguably the most important technique in this thesis is the optical lithography to define mesa structures on the sample. Therefore, it is crucial to understand the principle of optical lithography. The sample, which undergoes optical lithography, is first cleaned in acetone and isopropanol in an ultrasonic bath for 2 min. Afterwards an optical-resist layer (AZ MIR 701 from microchemicals) is spincoated on the sample surface and baked afterwards at 90°C for 90 s. The resist layer is then checked for imperfections under a microscope with a red LED, since the resist is only sensitive to blue light. The sample is then placed on the vacuum chuck of the laser writer system PicoMaster 200.

The PicoMaster 200 system has a red and a blue laser. The blue laser functions as the writing module, which exposes the resist whereas the red laser is used for the focus capture. The focus is measured by a so called focus-sum-voltage originating from the reflection on the sample. In order to get a good writing result, a value of the focus-sum-voltage between 3 V and 4 V is optimal. Therefore, the red laser power needs to be adjusted for each sample individually to achieve a good focus-sum voltage. For highly reflective samples a red laser power of around $100\ \mu\text{W}$ is sufficient, whereas for optical transparent substrates used in this study, it has to be increased to around $350\ \mu\text{W}$. Not only the correct red laser power but also a very good resist quality and uniformity is crucial for accurate and reproducible results. However, the uniformity of the resist always becomes slightly worse towards the sample edges. Thus, the auto sum-voltage setting is useful when writing structures over a large area of the sample. This allows the PicoMaster 200 system to automatically adjust the red laser power during the writing process to always get the desired focus-sum-voltage. Moreover, this is very helpful when writing on different materials at once which causes different reflections of the red laser and therefore requires different red laser powers. Before starting the actual writing process the laser writer needs initial parameters. First the

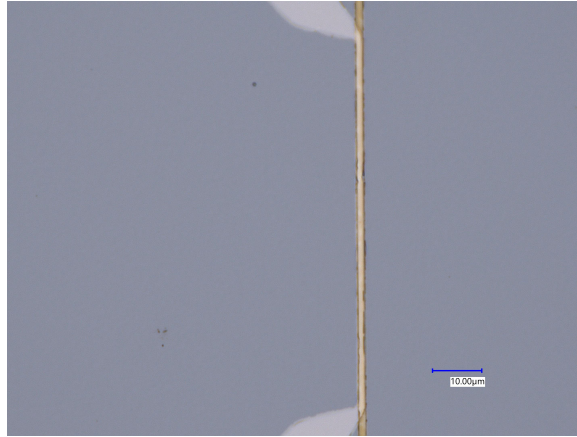


Figure 3.1.1.: Optical microscope picture of the alignment of the bottom and top Pt layers using alignment markers. The alignment error is < 200 nm.

dimensions of the sample have to be set. The system is designed to be able to write on a variety of sample dimensions from 5×5 mm² up to 200×200 mm². Secondly, the writing method needs to be selected. The main writing mode is a line-by-line mode where the structure design is rasterized and the write-head will write the design as the name suggests one line after the other. There the rasterization size, which corresponds to the dimensions of each "pixel" is set in the options as well as the scan speed which determines how fast the write head will move over the sample. However, the scan speed is limited to a few distinct settings with the slowest being 20 mm s^{-1} , which is used in this work. The second write mode is a vector write mode. Therefore the structure design first needs to be converted to a gerber file. This conversion determines the route the laser write head will take while moving over the sample. In this mode the speed of the write head needs to be adjusted as well. In this work a speed of 10 mm s^{-1} is used. Which of those writing modes is beneficial depends on the structure design as well as on the subsequent fabrication steps and the used resist. When using a positive resist, as is done in this work, the line by line mode is beneficial if a large area of the sample needs to get exposed, since there is no speed advantage by the laser write head taking an optimized route. If only small areas of the sample need to get exposed, the vector write mode is beneficial. This is due to a smaller possible write speed in the vector write mode. However, the conversion into gerber files can cause issues if a large number of structures is in one design file. Therefore it is advisable to create an individual gerber file for each structure.

Before starting the writing process the exact sample position needs to be determined. Therefore, the position of the top left corner is saved using a camera in the write head. If alignment markers are on the sample, the PicoMaster 200 system can align the sample automatically using an alignment recipe. In this recipe the design of the alignment markers as well as the positions on the sample where the alignment markers should be are saved. During the alignment it moves over the expected marker positions and determines their actual position using image recognition. This corrects for any alignment error due to an

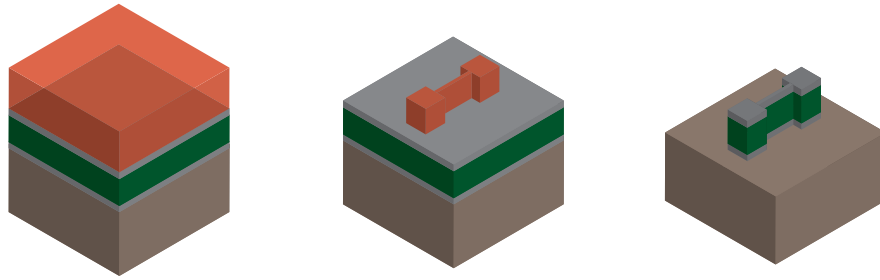


Figure 3.2.1.: Schematic of the Ar-ion milling process. The red layer corresponds to the photoresist and the green as well as the grey layer to the YIG and Pt layers, respectively.

imperfect alignment by placing the sample in the chuck and determining the top-left corner position by hand, allowing for very good alignment of different layers as shown in the optical microscope picture in Fig. 3.1.1. The alignment-error in this work is consistently smaller than 200 nm. For the writing process additional settings, such as the size of the laser spot and the attenuation need to be set depending on the accuracy needed. For the samples fabricated in this thesis a laser spot of 300 nm is used as well as the high attenuation setting providing the highest accuracy. Moreover, an energy density of 120 mJ cm^{-2} is used for the writing process. When these parameters are given to the laserwriting system, the laser is focused on the middle of the sample. During this step, the adjustment of the red laser power as well as the adjustment of the lens height is done. Then the position on the sample of the desired structure can be adjusted. Before starting the writing process the write head will search for the focus in a but slightly shifted position compared to the start position.

Then the desired structure is written into the optical resist by exposing certain parts of the sample to UV light. During the writing process the red laser is kept on the whole time. This allows for an auto-focus and therefore small adjustments during the writing process.

After the exposure the sample is removed from the laserwriter and a post-exposure bake is performed at 110°C for 90 s in order to remove standing wave effects from interference effects caused by the use of monochromatic light during the exposure [60]. Subsequently, the sample is developed in the AZ 726 MIF developer from microchemicals for 60 s with two subsequent dips in a water bath for 20 s each. In this step the exposed resist gets removed whereas the not exposed resist remains on the sample surface. Next either a lift-off process or Ar-ion milling is performed.

3.2. Ar-ion milling

If using Ar-ion milling the material is deposited before the optical lithography and etched afterwards so that only the material on the not exposed parts of the sample remains. The remaining resist can be removed with Acetone afterwards. In Fig. 3.2.1 a schematic of the whole process is shown. A Pt/YIG/Pt trilayer on a substrate is coated as described in Chapter 3.1 by a photoresist (left picture). The photoresist is then exposed and developed leaving only photoresist at the desired position of the sample (middle picture)). Then

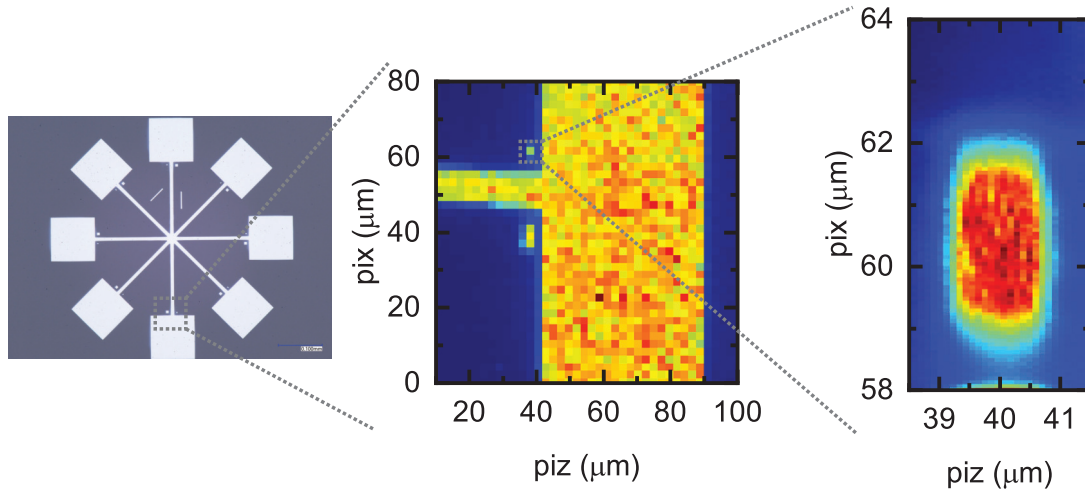


Figure 3.2.2.: Optical microscope picture and scanning x-ray diffraction data of a Pt/GdIG//GGG sample, patterned by optical lithography and subsequent Ar-ion milling. The x-ray diffraction experiment was conducted at the ID01 beamline of the European Synchrotron Radiation Facility with a beam size of $140 \times 120 \text{ nm}^2$ at a photon energy of $E = 7.938 \text{ keV}$ at the GdIG (444) Bragg peak.

Ar-ion milling is performed with subsequent removal of the remaining photoresist which leaves only the substrate and the desired Pt/YIG/Pt strip structure.

To optimize the optical photolithography process using the PicoMaster 200 as well as the Ar-ion milling process, several Pt/Gd₃Fe₅O₁₂ (GdIG) bilayer samples were fabricated using different crystallographic orientations of the Gd₃Ga₅O₁₂ (GGG) substrate (see Tab. A.1.2 in Appendix A.1). In Fig. 3.2.2 an optical microscope picture of a thus obtained structure patterned by Ar-ion milling is shown (left image). The width of the strips connecting the pads is $8 \mu\text{m}$ and the pads itself are $100 \mu\text{m} \times 100 \mu\text{m}$. Furthermore, small structures are located close to the pads and the strips. These samples are used for a resonant elastic x-ray scattering (REXS) experiment at the ID01 beamline of the European Synchrotron Radiation facility (ESRF) raster-scanning the sample using a x-ray nanobeam with dimensions of $140 \times 120 \text{ nm}^2$. A x-ray diffraction recorded at the GdIG (444) Bragg reflection with an x-ray energy of 7.938 keV , which corresponds to the Gd L₂ absorption edge [61], of the highlighted area of the sample is shown in Fig. 3.2.2 (middle image). Next to the strips is a $2 \times 3 \mu\text{m}^2$ large rectangle which is in more detail investigated in the picture on the right. The data reveals a good crystalline quality of the GdIG thin film in the center of the rectangle with slightly decreased intensity of the GdIG (444) reflection towards the edges of the structure. This might be due to the finite beam area or due to the Ar-ion milling and a worse resist quality at the edges. However, Fig. 3.2.2 demonstrates a high crystalline quality of epitaxial thin films even after Ar-ion milling processes lasting more than 10 min. Furthermore, structures with a few μm in size exhibiting sharp edges can be realized with optical lithography using the PicoMaster 200 and subsequent Ar-ion milling.

3.3. Lift-off process

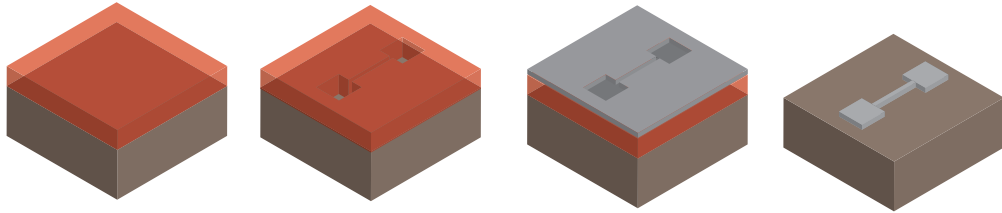


Figure 3.3.1.: Schematic of the lift-off process. The red layer corresponds to the photoresist.

The lift-off process differs to the Ar-ion milling process in the way that the material is not deposited before the optical lithography but afterwards. Therefore, the material is deposited on top of the resist layer except for regions on the sample which are exposed by UV. This process is schematically shown in Fig. 3.3.1. First the sample is cleaned and coated by the resist (left image). Thereafter parts on the resist necessary for the desired structure are exposed by UV light and subsequently developed (left middle image). Then the material is deposited on the sample. Thus, the material is only deposited on the sample surface on parts that have been exposed (right middle image). After deposition the lift-off process is performed by putting the sample in a 70°C hot Acetone bath for 15 min. During this time the resist layer under the deposited material is dissolved. Afterwards the ultrasonic bath is switched on for 1 min. During this time the material is lifted off from the sample and only the desired structure is left on the sample (right image). Within this thesis, this technique is not only used for sputter deposited thin films but also together with pulsed laser deposition.

4. Fabrication of patterned Pt/Y₃Fe₅O₁₂/Pt heterostructures

This chapter deals with the optimization of the fabrication of vertical, patterned Pt/Y₃Fe₅O₁₂/Pt heterostructures. To this end the samples are characterized via their structural and magnetic as well as magnetotransport properties in form of angle dependent magnetoresistance measurements (ADMR) of the top and bottom Pt layers. These findings are then compared to previously reported results and existing literature for further optimization.

4.1. Fabrication of patterned Pt/Y₃Fe₅O₁₂/Pt heterostructures by etching

Starting from the results of the bachelor thesis of Christian Mang [62] patterned Pt/YIG/Pt heterostructures are fabricated by Ar-ion milling of an in-situ deposited Pt/YIG/Pt heterostructure. As a substrate serves Gd₃Ga₅O₁₂ (GGG) oriented in (001) direction, since it has a very low lattice mismatch with Y₃Fe₅O₁₂ (YIG) of only 0.03% [63]. The Pt layers are deposited via electron beam evaporation (EVAP) with a rate of 0.4 Å s⁻¹ (see Appendix A.3.2). The YIG thin film is deposited by pulsed laser deposition (PLD) (see Appendix A.3.1) at room temperature in an Ar atmosphere of $p_{\text{Ar}} = 25 \mu\text{bar}$ to minimize oxidation of the lower Pt layer. 20000 pulses with a frequency of 10 Hz and a target fluence of 2 J cm⁻² are used, which corresponds to a YIG thickness of about 25 nm. Subsequently, the sample is annealed in the PLD chamber using an infrared heating laser, which is performed in the same Ar atmosphere as the PLD process, leading to crystallization of the YIG film. For the annealing of the YIG layer a two step rapid annealing process is used which promises crystallization of YIG on the bottom Pt layer with an expected reduced diffusion of ions at the Pt/YIG interfaces [55, 59]. In Fig. 4.1.1 the time evolution of the temperature during annealing is shown which has already proven to be able to produce crystalline YIG thin films on Pt layers [62]. The sample is first heated within 45 s to a temperature of $T = 350 \text{ }^\circ\text{C}$ where it stays constant for 100 s (first annealing step). During this time the YIG thin film forms seed crystals from which amorphous parts can crystallize in the second step [59]. In the second step the temperature is increased to 600 °C and kept constant for 10 s. All these steps were performed in-situ without breaking the vacuum in our PLD ultra-high vacuum (UHV) cluster. The thus fabricated trilayer is then investigated regarding its structural properties in a high

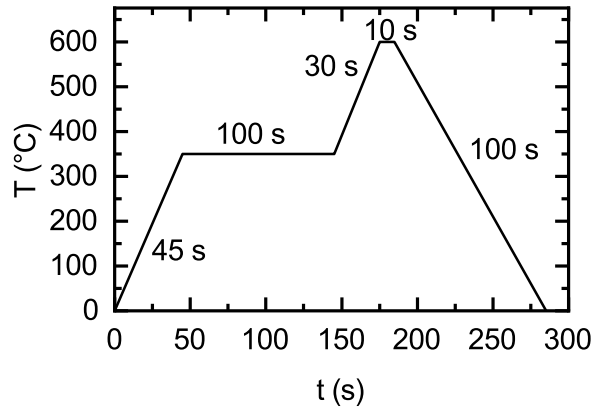


Figure 4.1.1.: Temperature progression during the two step rapid annealing process. The regions with constant temperatures correspond to the two steps.

resolution x-ray diffractometer (see Appendix A.4.1).

In Fig. 4.1.2 the x-ray diffraction (XRD) and x-ray reflectometry (XRR) as well as an XRR simulation are shown. The XRD measurement (cf. Fig. 4.1.2 (a)) shows a clear GGG (004) substrate reflection. However, there is no YIG reflection visible. Thus, there is no indication of a recrystallization of the YIG layer. This is similar to the results for inverted YIG/Pt bilayers fabricated in an Ar-atmosphere by C. Mang [62]. The expected position of the YIG (004) peak indicated by the vertical dashed line in Fig. 4.1.2 (a) is calculated by using the lattice constant $a_{\text{YIG, lit}} = 1.2376 \text{ nm}$ [64]. The XRR data (cf. black line in Fig. 4.1.2 (b)) shows clear Kiessig fringes from which the thickness as well as the roughness of the layers can be determined. To this end the XRR data are simulated using the LEPTOS software package. The main input parameters are the layer sequence with respective layer thickness and roughness as well as the densities of the layer materials. By adjusting the thicknesses as well as the roughnesses of the layers the simulation and the measured data can be matched. In this Pt/YIG/Pt//GGG heterostructure the density of the YIG had to be adjusted as well in order to get a good simulation result. The thus obtained thickness and roughness of the bottom Pt layer are $t_{\text{Pt, bot}} = (1.7 \pm 0.3) \text{ nm}$ and $R_{\text{Pt, bot}} = (0.29 \pm 0.05) \text{ nm}$ respectively. Furthermore, we obtain a thickness of the YIG layer of $t_{\text{YIG}} = (5.5 \pm 0.3) \text{ nm}$ with a roughness of $R_{\text{YIG}} = (0.29 \pm 0.05) \text{ nm}$ and thickness of the top Pt layer of $t_{\text{Pt, top}} = (2.7 \pm 0.2) \text{ nm}$ with a roughness of $R_{\text{Pt, top}} = (0.27 \pm 0.06) \text{ nm}$. Despite of a number of 20000 pulses used during the deposition of the YIG layer, only a thickness of $(5.5 \pm 0.3) \text{ nm}$ is obtained by the simulation of the XRR data, which demonstrates a very small growth rate during the deposition of the YIG layer in this sample.

To perform electrical transport measurements the sample is patterned into mesa-structures using optical lithography and subsequent Ar-ion milling as described in Chapter 3. In Fig. 4.1.3 a schematic as well as an optical microscope picture of the patterned sample are shown. The width of the 300 μm long Pt/YIG/Pt stripes increases from left to right from 1 μm to 5 μm .

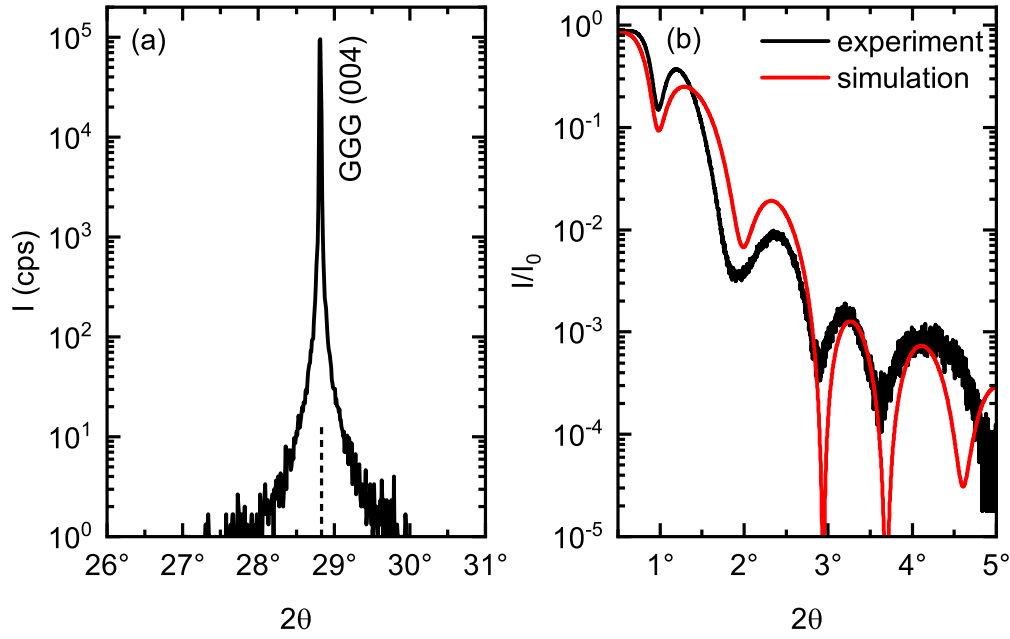


Figure 4.1.2.: Structural properties of a Pt/YIG/Pt//GGG heterostructure. The out of plane 2θ - ω scan is shown in (a). In (b) the x-ray reflectometry scan (black line) is plotted against the 2θ angle. From the simulation (red line) the thickness and roughness of the layers is determined. For the simulation a Pt/YIG/Pt//GGG heterostructure with increased density of the YIG layer is used.

In order to measure the electrical resistance of the strips, Al wire bonding is used for electrical connection. However the Pads connected by the strips had no electrical contact. Therefore, the Pt stripes have an open contact, which might be caused by the Ar-ion milling and/or the in-situ fabrication of the Pt/YIG/Pt heterostructure.

The non-crystalline YIG layer and the discontinuous Pt strips as well as the absence of ferrimagnetic order in similarly fabricated Pt/YIG bilayers by C. Mang [62] call for modification of the fabrication process of patterned Pt/YIG/Pt heterostructures. We therefore used an ex-situ lift-off process discussed in Chapter 3 to fabricate vertical, patterned Pt/YIG/Pt structures. This allows for electrical measurements of the Pt layers after each fabrication step and allows to bring the YIG layer in direct contact with the substrate which might improve the crystalline quality of the YIG layer.

4.2. Fabrication of Pt/YIG/Pt heterostructures by using a lift-off technique for the Pt and the YIG layers

As a first optimization step we use the lift-off technique as described in Chapter 3. This, however leads to a more complex fabrication process and results in breaking of the vacuum for each lift-off process leading to ex-situ interfaces. The fabrication is now divided into 5 steps where between the first 4 steps optical lithography is performed. First, alignment markers made of Pt for subsequent lithography steps are deposited via sputtering and lift-

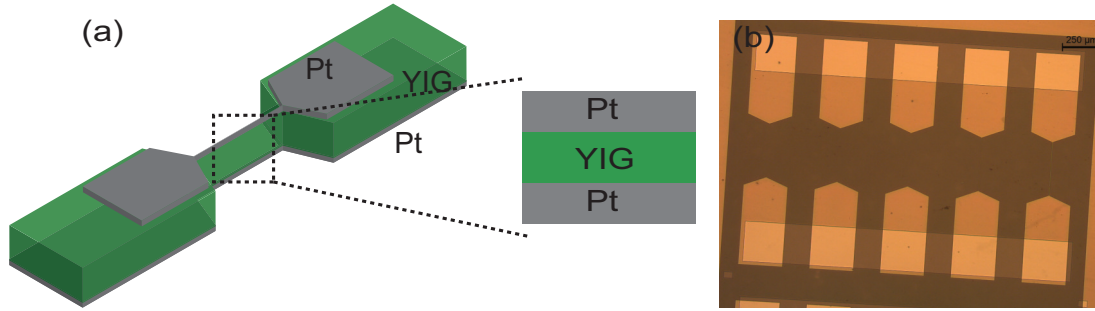


Figure 4.1.3.: (a) Schematic of the structure design used for etching. (b) Optical microscope picture of a finished sample produced by etching. The thickness of the small Pt strips between the contact pads increases from left to right from 1 μm to 5 μm.

off onto the substrate. These are crucial since the top and bottom Pt strip are only a few μm wide and need to be aligned exactly on top of each other. Next the bottom Pt layer is deposited via sputtering in the SUPERBOWL system (see Appendix A.3.3) with a following lift-off step. Afterwards the YIG and top Pt film are deposited via PLD at room-temperature and EVAP in-situ without breaking the vacuum followed by another lift-off process. As a last step the sample is annealed in the PLD chamber via the two step rapid annealing discussed in Chapter 4.1. In Fig. 4.2.1 (a) a schematic drawing of the used structure design is shown. The bonding pads are moved to the side compared to Fig. 4.1.3 which leads to direct contact between the YIG thin film and the substrate. This might lead to a better formation of seed crystals in the first annealing step, from which in the second step the YIG film on top of the Pt strip gets crystallized starting from both bond pads. Moreover an optical microscope picture of the sample before the YIG and top Pt deposition (Fig. 4.2.1 (b)) as well as well as a picture taken after the YIG and top Pt deposition and subsequent lift-off (Fig. 4.2.1 (c)) is shown, proving that lift-off can be performed even after a PLD process where molecules with high kinetic energy hit the resist. This structure, however, does not give a finite XRD signal above the noise level since the deposited material covers only a small area of the sample.

The resistance of the bottom Pt strip is measured before the deposition and annealing of the YIG layer as well as afterwards. The hence calculated resistivity of the bottom Pt strip before annealing is $\rho_{\text{before annealing}} = 6.96 \times 10^{-7} \Omega \text{ m}$ which is similar to previously reported values by Althammer *et. al* [14], whereas it increases significantly to $\rho_{\text{after PLD}} = 1.05 \times 10^{-3} \Omega \text{ m}$ after the PLD process and subsequent annealing. Moreover, the top Pt stripe does not show a finite conductivity between the contact pads. Therefore, further optimization of the structure is required.

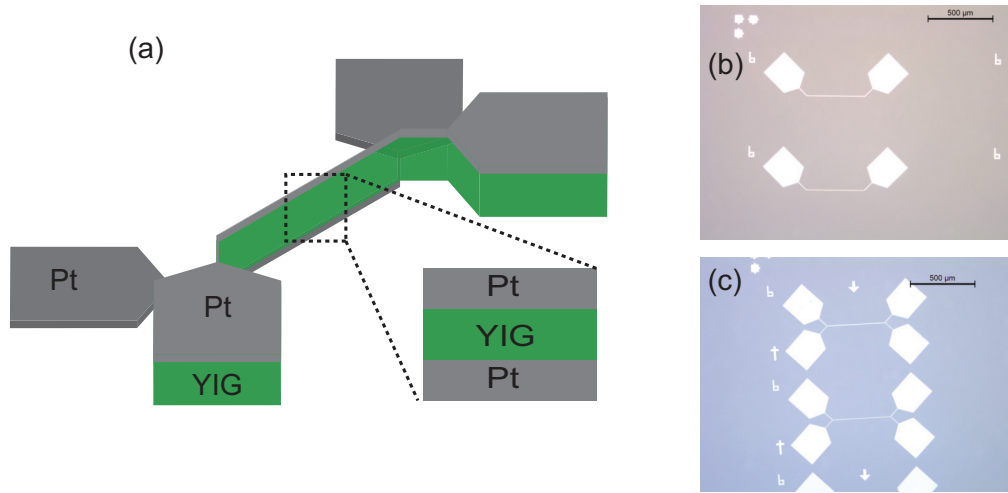


Figure 4.2.1. (a) Schematic drawing of the used sample structure for the samples produced by lift-off process. Optical microscope picture (b) of the bottom Pt layer before YIG deposition as well as (c) of a finished sample after the lift-off process for the YIG and top Pt layer. b indicates the bottom Pt layer and t the top Pt/YIG bilayer.

4.3. Fabrication of Pt/YIG/Pt heterostructures by using a lift-off technique solely on the Pt layers

In order to improve the conductivity of the Pt strips as well as the crystalline quality of the YIG layer, the YIG layer is now deposited over the whole sample surface. This leads to an encapsulation of the bottom Pt layer which might improve the stability during the PLD and annealing process as well as the crystallization of the YIG on top of the Pt strip due to the contact to the substrate along the whole strip length. This further increases the area of the YIG layer in direct contact to the garnet substrate as well as reduces the distance of the crystallization front needed to cover the YIG layer above the bottom Pt strips. This might further increase the crystallinity of the YIG layer. Moreover, the top Pt strip is deposited after the YIG deposition and subsequent annealing. This might improve the conductivity of the top Pt strip. Additionally, covering the whole substrate surface with YIG allows for investigation of the structural properties of the YIG thin film by XRD and XRR measurements. However, this results in an ex-situ interface of YIG and the top Pt strip, due to the necessary optical lithography step for the top Pt layer after deposition and annealing of the YIG layer. To increase the transparency of the spin current between the YIG layer and the Pt strip, the top Pt layer is now deposited via dc-sputtering in the SUPERBOWL system (see Appendix A.3.3) since this deposition technique was proven to result in a high spin Hall magnetoresistance amplitude using ex-situ interfaces [65]. A schematic drawing of the now used structure as well as an optical microscope picture of a finished sample is shown in Fig 4.3.1.

In Fig. 4.3.2 (a) the structural properties investigated by XRD are shown. The substrate GGG (004) reflection is clearly visible. Contrary to before in Fig. 4.1.2 (a) there are small

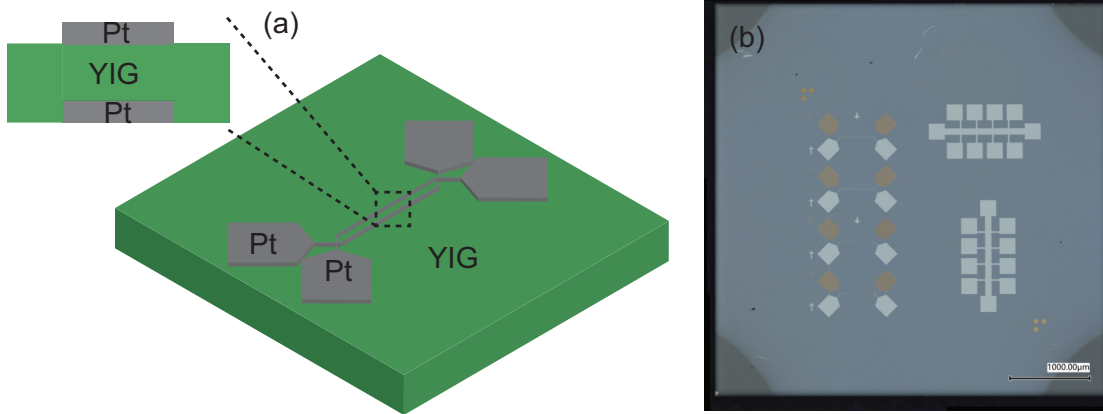


Figure 4.3.1.: (a) Schematic of the sample design used for the heterostructure with the YIG film covering the whole surface. (b) Optical microscope picture of a finished sample with two additional Hall bar mesa structures.

shoulders indicated by arrows visible next to the substrate peak. Moreover, the substrate peak shows a slight asymmetry. This can be attributed to a YIG (004) reflection hidden underneath the substrate reflection, which indicates crystalline growth of the YIG layer. The expected position of the YIG (004) reflection is again indicated by the dashed vertical line. In Fig. 4.3.2 (b) the measured XRR data (black line) as well as a simulation of the data (red line) are shown. For the simulation, a YIG//GGG sample has been used since in the experiment no fringes originating from the 5 nm thin Pt layers are visible due to the very small area covered by Pt compared to the area of the whole sample. From the simulation the thickness of the YIG layer is determined to $t_{\text{YIG}} = (25.7 \pm 0.2)$ nm and the roughness to $R_{\text{YIG}} = (0.48 \pm 0.02)$ nm, respectively. This thickness is reasonable taking the number of pulses during the PLD process into account.

The resistance of the bottom Pt layer is again measured before the YIG deposition and annealing as well as afterwards. The resistivity of the bottom Pt layer before the YIG deposition is $\rho_{\text{before PLD}} = 9.63 \times 10^{-7} \Omega \text{ m}$ which increases to $\rho_{\text{after PLD}} = 2.57 \times 10^{-5} \Omega \text{ m}$ after deposition and annealing. However, the resistivity of the top Pt layer is $\rho_{\text{top}} = 1.60 \times 10^{-7} \Omega \text{ m}$ which is slightly smaller than previous results for similarly thin Pt layers [14]. This indicates that the PLD process or the annealing step are possible causes for the increase in the resistivity of the bottom Pt layer.

To determine which of these two is the reason for the increase in resistivity, the heterostructure is fabricated with the same parameter but without the two step annealing process. In Fig. 4.3.3 (a) the XRD measurement is shown in which only the substrate GGG (004) reflection with no contribution from the YIG layer is visible. This is expected since the YIG layer is deposited at room temperature without subsequent annealing and therefore amorphous. Furthermore, in Fig. 4.3.3 (b) the XRR measurement (black line) is shown as well as the simulation of the data (red line). For the simulation a YIG//GGG sample sequence is used, since the Pt layer is again not visible in the XRR data. Furthermore, the density of the YIG had to be increased to $\rho_{\text{YIG}} = (7.2 \pm 0.2) \text{ g cm}^{-3}$ to get a better match between

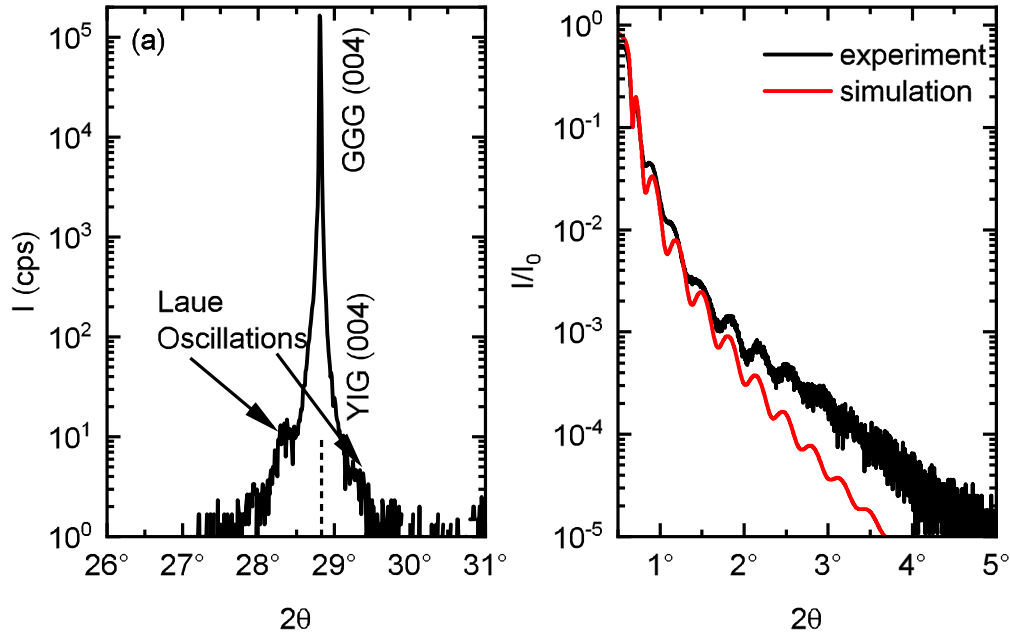


Figure 4.3.2.: Structural properties of a Pt/YIG/Pt//GGG trilayer with the YIG layer covering the whole sample. (a) Out of plane $2\theta - \omega$ scan and (b) x-ray reflectometry scan. From the simulation (red line) the thickness and roughness of the layers is determined. For the simulation a YIG//GGG sample sequence is assumed.

simulation and experimental data. However, it is clearly visible that the measured data show some additional features around 1.5° , which could not be simulated using a single YIG layer. This might be attributed to a finite reflection from the Pt pads and strips on the sample. The thickness and roughness of the YIG layer are extracted from the simulation to $t_{\text{YIG}} = (24.9 \pm 0.1)$ nm and $R_{\text{YIG}} = (0.23 \pm 0.05)$ nm.

The resistance of the bottom Pt strip of this heterostructure is only measured after the YIG deposition since the Pt-resistance before the YIG deposition is expected to have the same value as measured in the heterostructure with annealing. The resistivity of the bottom Pt strip after the PLD process is $\rho_{\text{bot}} = 9.44 \times 10^{-9} \Omega \text{ m}$ which is only slightly higher than we expect for 5 nm thick Pt films [14]. However, this is most likely caused by a higher surface roughness due to the PLD process. Therefore, the annealing step seems to be the main reason for the large increase of the Pt-resistance observed in the bottom Pt strip after annealing. In this regard, the annealing temperature during the second annealing step might be too high, since the temperature of the sample surface measured by an additional pyrometer was reaching 702°C during the second annealing step. This could lead to a deformation of the Pt layer or even discontinuous Pt thin films which has been reported for temperatures higher than 600°C [66, 67]. Therefore the annealing temperature during the second annealing step is reduced from 600°C to 450°C corresponding to a temperature of the sample surface of approximately 570°C .

However, this results in a worse crystalline quality of the YIG layer as there is no sign of a crystalline YIG reflection visible in the XRD measurement shown in Fig. 4.3.4 (a). There

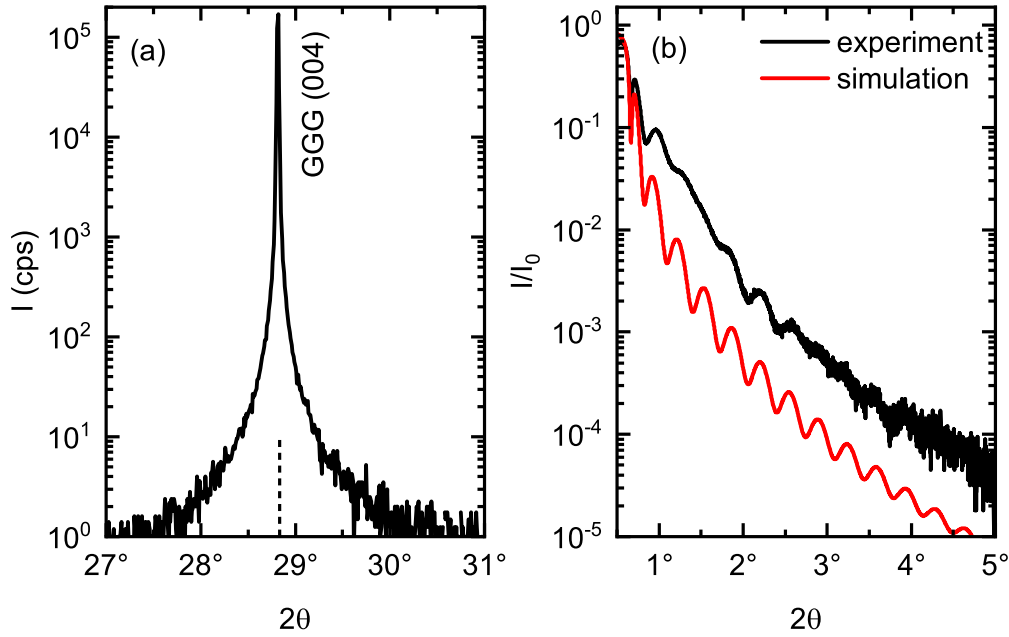


Figure 4.3.3.: Structural properties of a Pt/YIG/Pt//GGG trilayer without annealing of the YIG layer. The out of plane 2θ - ω scan is shown in (a). In (b) the x-ray reflectometry scan is plotted against the 2θ angle. From the simulation (red line) the thickness and roughness of the layers are determined. For the simulation a YIG//GGG sample sequence is assumed.

is only the GGG (004) reflection visible, indicating an amorphous YIG layer. The vertical dashed line indicates the expected position of the YIG (004) reflection. In Fig. 4.3.4 (b) the XRR data (black line) are shown together with the simulation (red line). To match the experimental data the density of the YIG thin film had to be adjusted to $\rho_{\text{YIG}} = (7.3 \pm 0.2) \text{ g cm}^{-3}$ in the simulation. In the experimental data the same feature around 1.5° as in Fig. 4.3.3 is visible, which most likely stems from the Pt layers, which are not taken into account in the simulation. However, the thickness of the YIG film can be determined to be $t_{\text{YIG}} = (24.9 \pm 0.2) \text{ nm}$ and the roughness to be $R_{\text{YIG}} = (0.513 \pm 0.02) \text{ nm}$, which is similar to the obtained thickness of the respective trilayer using a higher annealing temperature of 600°C .

Measuring the resistance of the Pt strips reveals a resistivity of the bottom Pt strip of $\rho_{\text{bot, Pt}} = 9.49 \times 10^{-7} \Omega \text{ m}$ and $\rho_{\text{top, Pt}} = 2.37 \times 10^{-7} \Omega \text{ m}$ of the top strip, which is in the same region as the expected value [14]. However, measuring the resistance between the two Pt strips separated by the YIG layer reveals an electrical short between the two Pt strips, since a similar value in the $\text{k}\Omega$ -range as along one single Pt strip was obtained. This is most likely caused by pinholes within the 24.9 nm thin YIG layer.

Due to the lack in crystallinity of the YIG layer the substrate material is changed from GGG to Y₃Al₅O₁₂ (YAG), since it promises better crystalline quality and lower surface roughness at lower annealing temperatures [63]. By using a (001)-oriented YAG substrate, a patterned Pt/YIG/Pt//YAG heterostructure is fabricated using the same steps as before

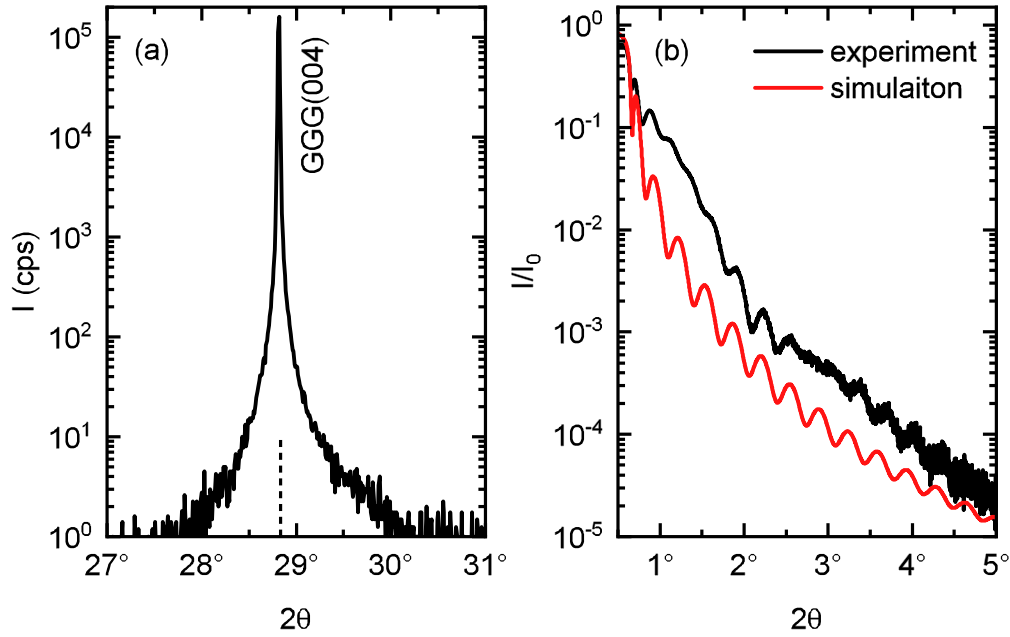


Figure 4.3.4.: Structural properties of a Pt/YIG/Pt//GGG trilayer using a reduced annealing temperatures of 450 °C for the crystallization of the YIG layer. The XRD and XRR data are shown in (a) and (b), respectively. From the simulation of the XRR data (red line) the thickness and roughness of the layers is determined. For the simulation a YIG//GGG layer sequence is assumed.

with a maximum temperature during the annealing step of 450 °C. The structural properties of this patterned Pt/YIG/Pt heterostructure are shown in Fig. 4.3.5. The XRD scan (Fig. 4.3.5 (a)) shows the YAG (004) substrate reflection as well as a clear YIG (004) reflection with Laue oscillations indicating a coherent crystalline growth of the YIG layer. The 2θ angle of the YIG (004) reflection is determined by a Gaussian fit. From this 2θ angle the lattice constant of the YIG layer is calculated to $a_{\text{YIG}} = (1.239 \pm 0.005)$ nm, which is within the margin of error to the literature value of $a_{\text{YIG, lit}} = 1.237$ nm [64]. This demonstrates, that the YIG layer grows fully relaxed on the YAG substrate. The rocking curve shown in the inset of Fig. 4.3.5 (a) displays a double peak structure with a full width at half maximum (FWHM) of $w_{\text{FWHM}} = (0.381 \pm 0.003)^\circ$ whereas the thin peak has a FWHM of $w_{\text{FWHM}} = (0.0172 \pm 0.0009)^\circ$. This indicates a mosaic spread of the YIG thin film, which may be resulting from the large lattice mismatch of YIG to YAG of 3%. It might also be a result of the two step annealing itself since during the first step seed crystals are created which might be polycrystalline on which the YIG crystallizes during the second step [59]. However, the very thin peak of the rocking curve as well as the finite thickness fringes visible in the 2θ - ω scan together with a high intensity of the YIG (004) reflection demonstrate a high crystalline quality of most of the YIG layer. In the reflectometry data shown in Fig. 4.3.5 (b) clear fringes stemming from Pt are visible. The reason why these larger fringes are visible now might be due to the additional Hallbar mesa structures (see Fig. 4.3.1) increasing the area of the Pt on the top surface. Therefore, a Pt/YIG//YAG stack is used for the simula-

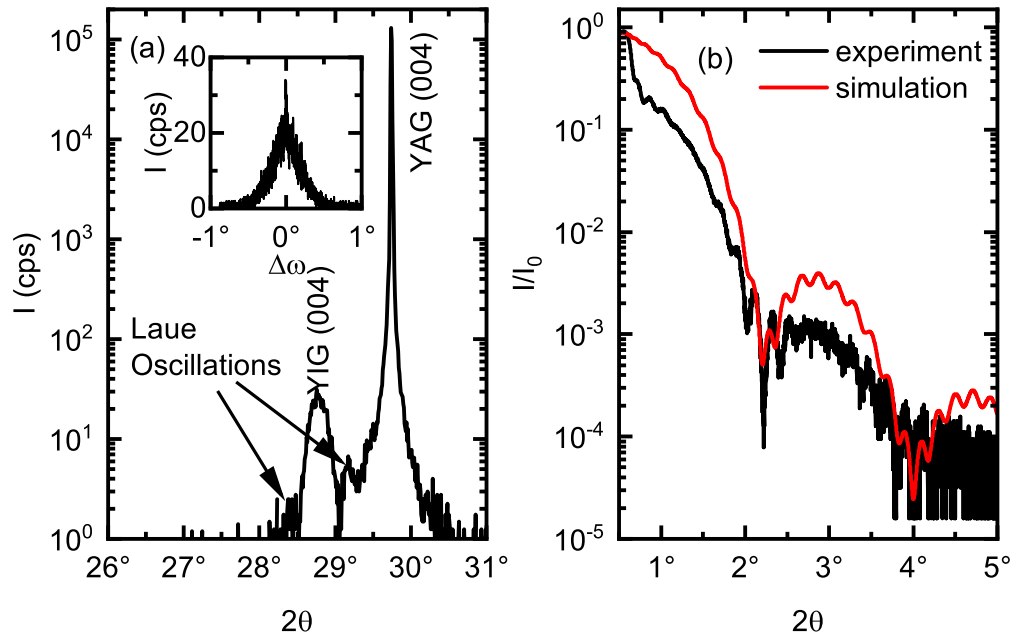


Figure 4.3.5.: Structural properties of a Pt/YIG/Pt//YAG heterostructure fabricated using an annealing temperature of 450 °C for the crystallization of the YIG layer. The out of plane 2θ - ω scan is shown in (a). The inset displays the rocking curve around the YIG (004) reflection. In (b) the x-ray reflectometry scan is plotted against the 2θ angle. From the simulation (red line) the thickness and roughness of the layers is determined. For the simulation a Pt/YIG//YAG heterostructure is assumed.

tion of the XRR data, since the bottom Pt only covers 1.4% of the sample whereas the top layer covers 5.4%. Thus, a larger contribution from the top Pt layer is expected. However, at small angles the simulation and the experimental data show a rather big discrepancy. A sharp decrease in intensity is visible in the experimental data, whereas in the simulation the decrease is much shallower. This can be attributed to the fact that the Pt layer is not covering the whole sample, but only the spots where the pads and strips as well as were the hallbars are located which can't be simulated by the LEPTOS software. Except for this 2θ -range, the simulation matches the experimental data well and the determined values for the YIG and Pt thicknesses as well as the roughnesses are $t_{\text{YIG}} = (37.9 \pm 0.2)$ nm, $t_{\text{Pt}} = (4.6 \pm 0.1)$ nm, $R_{\text{YIG}} = (0.30 \pm 0.02)$ nm, and $R_{\text{Pt}} = (0.27 \pm 0.02)$ nm, respectively. The thickness of the YIG layer is about as thick as expected for the used number of pulses. Moreover, the Pt layer is in good agreement with the set thickness of 5 nm during the sputtering process.

The structural properties of the YIG and top Pt layer are additionally investigated by atomic force microscopy (AFM) (see Appendix A.4.2). In Fig. 4.3.6 the taken AFM image of the top Pt layer (a) and of the YIG layer (b) is shown. The Pt layer shows a relative smooth surface with some grains with a maximum peak height of 8.6 nm and an approximate diameter of 500 nm. The root-mean-square (RMS) roughness of this layer is determined to $R_{\text{RMS, Pt}} = 1.05$ nm. This is quite high compared to the roughness determined by the XRR

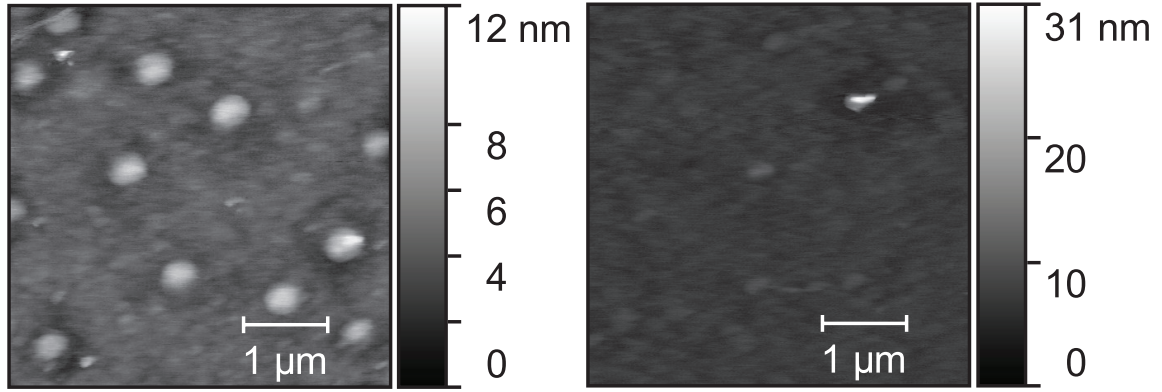


Figure 4.3.6: Atomic force microscopy pictures of (a) the top Pt layer as well as (b) the YIG film of the Pt/YIG/Pt//YAG sample.

measurement. However, this might be attributed to the accuracy of the XRR simulation of the Pt layer since the area covered with Pt is small compared to the whole sample surface. Another reason might be that the AFM measurement shows a very locally limited area, whereas the XRR measurement averages over the whole sample. The AFM image of the YIG film shows a smooth surface with an RMS roughness of $R_{\text{RMS, YIG}} = 966 \text{ pm}$ and a single but quite high peak with a height of 27.4 nm . Compared to the XRR measurement the roughness determined by the AFM measurement is again higher. This might be due to the fact that the grain visible in Fig. 4.3.6 (b) is not detectable via the XRR measurement due to the averaging over a large area. By masking the large grain the RMS roughness is with $R_{\text{YIG without peak, RMS}} = 633 \text{ pm}$ still a factor of 2 larger than the by XRR distinguished value. However, there are still some smaller peaks with a maximum peak height of 5.9 nm . Therefore, these values are not in contradiction with each other, but a result of different measurement techniques.

4.3.1. Magnetic properties

Since the structural properties of the patterned Pt/YIG/Pt//YAG heterostructures are promising, the magnetic properties of the YIG thin film are investigated. Therefore SQUID (superconducting quantum interference device) magnetometry (see Appendix A.4.4) as well as ferromagnetic resonance (FMR) (see Appendix A.4.5) measurements are performed.

In Fig. 4.3.7 the magnetization hysteresis loop measured at room temperature (black curve) as well as at 10 K (purple curve) of a Pt/YIG/Pt trilayer with a YIG thin film fabricated by the two step rapid annealing method are shown after subtraction of the diamagnetic contribution from the YAG substrate. Fig. 4.3.7 (a) shows the field range from -1 T to 1 T from which the saturation magnetization is determined to $M_{\text{S, } 300 \text{ K}} = (100 \pm 2) \text{ kA m}^{-1}$ for the measurement at room temperature. This is in agreement with previous results for YIG layers deposited on a YAG substrate [57, 68]. However, compared to the literature value of bulk YIG at room temperature $M_{\text{S, lit}} = 143 \text{ kA m}^{-1}$ the determined value is slightly lower [69]. This might be due to the lower crystalline quality compared to YIG thin films

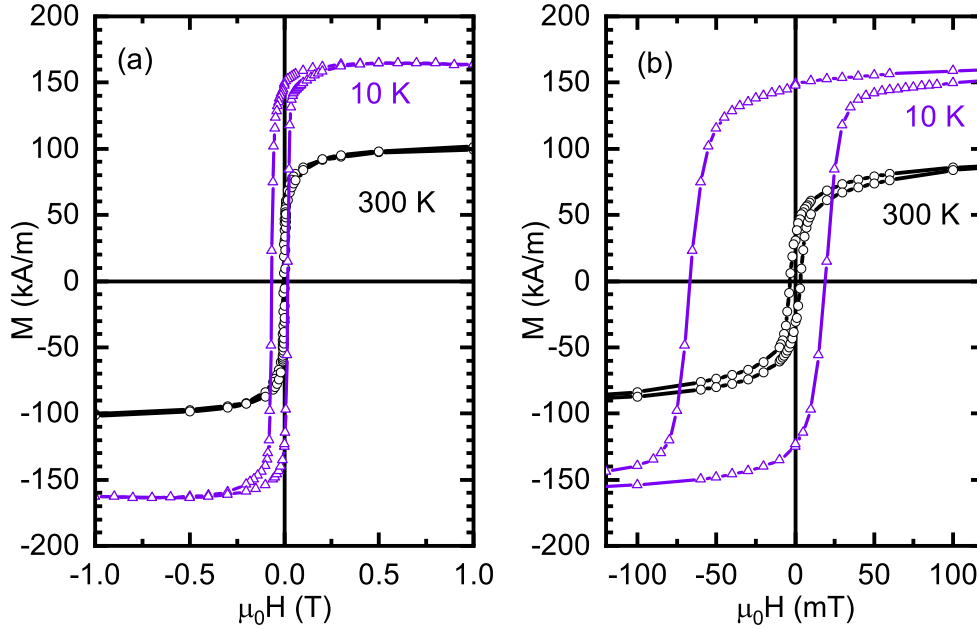


Figure 4.3.7.: (a), (b) Magnetization curves measured at 300 K (black data) and 10 K (purple data) of Pt/YIG/Pt//YAG sample with the YIG layer fabricated with the two step rapid annealing. The field is applied in the film plane and the diamagnetic contribution of the YAG substrate is subtracted.

on lattice matched GGG substrates (c.f. inset in Fig. 4.3.5 (a)) resulting in a higher disorder of magnetic moments. Furthermore, Al-diffusion from the YAG substrate into the YIG thin film during the annealing process might be possible in regions, where the YIG layer is in direct contact with the YAG substrate [57]. Al-doping of YIG leads to an antiferromagnetic ordering which reduces the saturation magnetization. In Fig. 4.3.7 (b) a zoomed in view around the zero field is shown. From this the coercive field is determined to $\mu_0 H_c = (3.3 \pm 2.5)$ mT at 300 K. This is in agreement with reported coercive fields between 1 mT and 15 mT [68]. At 10 K the saturation magnetization increases to (163.6 ± 0.7) kA m⁻¹, which is slightly lower than the saturation magnetization reported for a bulk YIG sphere at 10 K [70], but in good agreement with results for YIG thin films grown on YAG substrates by S. Altmannshofer [68]. Interestingly, at 10 K the hysteresis is shifted towards negative applied magnetic fields resulting in a coercive field for negative fields $\mu_0 H_{c-} = (66.6 \pm 2.5)$ mT and $\mu_0 H_{c+} = (18.9 \pm 2.5)$ mT for positive fields. With these values an exchange bias of $\mu_0 H_{ex} = (23.8 \pm 5)$ mT can be calculated. This might be caused by the aforementioned diffusion of Al from the YAG substrate into the first few YIG monolayers creating a Y₃Fe_{5-x}Al_xO₁₂ phase, which causes antiferromagnetically ordered monolayers at low temperatures in the vicinity of the YIG//YAG interface, which interact with the ferrimagnetic moments of the YIG by pinning them, resulting in an exchange bias [71]. However, the here determined exchange bias is much larger than previously reported values for YIG thin films grown on YAG substrates [68, 71]. It has also been shown by

Geprägs *et. al* that a finite Pt moment is induced by intermixing of YIG with the bottom Pt layer [57]. This might also result in the formation of a Pt₃Fe alloy which has been shown to order antiferromagnetically at low temperatures [72]. However, this would be only a small contribution to the overall measured magnetic moment, due to the small area of the YIG layer in direct contact with Pt.

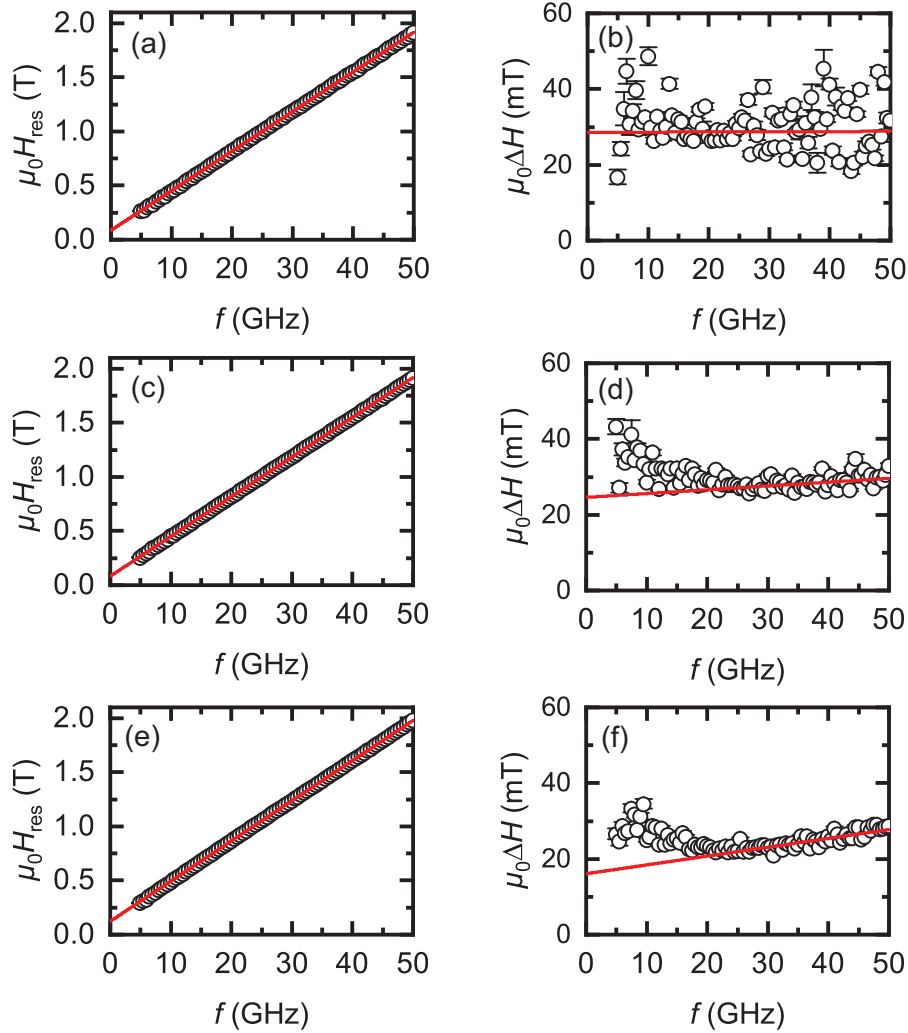


Figure 4.3.8.: Result of broadband FMR measured in out-of-plane geometry of (a), (b) a sample with YIG fabricated via two-step rapid annealing process, (c),(d) a YIG thin film on YAG substrate fabricated via the 'standard' PLD-fabrication process at finite substrate temperature in argon atmosphere as well as (e), (f) on a YAG substrate fabricated via the 'standard' fabrication process in oxygen atmosphere. In (a),(c) and (e) the resonant magnetic field $\mu_0 H_{\text{res}}$ whereas in (b), (d) and (f) the linewidth of the resonance $\mu_0 \Delta H$ is plotted as a function of frequency f .

Additionally, the Pt/YIG/Pt sample is investigated regarding ferromagnetic resonance (FMR) in order to investigate the magnetization dynamics of the YIG thin film. As reference samples a YIG layer fabricated by the two step rapid annealing process and two YIG//YAG samples which were fabricated via the standard PLD-procedure with a substrate temperature of 450 °C in either a pure argon or pure oxygen atmosphere with a pres-

sure of 25 μbar , respectively, are investigated.

The latter two reference samples are necessary, since previous works have shown that the magnetic properties of the YIG thin film can vary depending on the atmosphere used during fabrication [58, 62, 63]. In Fig. 4.3.8 the out-of plane FMR resonance field $\mu_0 H_{\text{res}}(f)$ and linewidth $\mu_0 \Delta H(f)$ as function of frequency f of a sample with a YIG thin film fabricated by (a), (b) the two-step rapid annealing, (c), (d) by the standard PLD-process at finite temperatures in oxygen atmosphere, (e), (f) as well as by the standard PLD-process in argon atmosphere are shown. The frequency dependent resonance fields are shown in Figs. 4.3.8 (a), (c) and (e). These are fitted using the Kittel equation (Eq. (2.13) from Chapter 2.5) (red line) from which the g -factor as well as the effective magnetization $\mu_0 M_{\text{eff}} = \mu_0 M_s - \mu_0 H_{\text{ani}}$, where $\mu_0 M_s$ is the saturation magnetization and $\mu_0 H_{\text{ani}}$ is the anisotropy field, are extracted. This yields a g -factor of (1.951 ± 0.002) and an effective magnetization of $\mu_0 M_{\text{eff}} = (86.4 \pm 0.1)$ mT for the YIG film fabricated by the two-step rapid annealing, a g -factor of (1.946 ± 0.001) and an effective magnetization of $\mu_0 M_{\text{eff}} = (83.0 \pm 0.5)$ mT for the reference sample fabricated in oxygen atmosphere, and a g -factor of (1.924 ± 0.001) and an effective magnetization of $\mu_0 M_{\text{eff}} = (123.2 \pm 0.8)$ mT for the reference sample fabricated in argon atmosphere.

Comparing these values the g -factor stays approximately constant for the different fabrication techniques. However, the effective magnetization shows an increase in the in argon deposited reference sample. This might be due to oxygen vacancies in the YIG thin film, which might lead to a change in anisotropy.

In Figs. 4.3.8 (b), (d), (f) the extracted resonance linewidths $\mu_0 \Delta H(f)$ as well as a linear fit by equation (2.14) from Chapter 2.5 (red line) are shown for the samples with different fabrication processes of the YIG layers: post-deposition two-step rapid annealing process (Fig. 4.3.8 (b)), standard PLD-deposition in oxygen atmosphere (Fig. 4.3.8 (d)) and standard PLD-deposition in argon atmosphere (Fig. 4.3.8 (f)). The reference samples show a clear linear dependency for frequencies greater than 20 GHz and are therefore in good agreement with the fit whereas at lower frequencies they show a non-linearity. From the fit the Gilbert damping α as well as the inhomogeneous linewidth broadening $\mu_0 H_{\text{inh}}$ are determined to be $\alpha_{\text{O}_2} = (1.37 \pm 0.41) \times 10^{-3}$, $\mu_0 H_{\text{inh, O}_2} = (24.6 \pm 1.1)$ mT for the in oxygen atmosphere fabricated YIG layer and $\alpha_{\text{Ar}} = (3.14 \pm 0.28) \times 10^{-3}$, $\mu_0 H_{\text{inh, Ar}} = (16.1 \pm 0.8)$ mT for the YIG layer fabricated in an argon atmosphere, respectively. However, the YIG film fabricated with the two step rapid annealing method shows a rather constant but noisy frequency dependency. From the fit the Gilbert damping is determined to $\alpha = (0.07 \pm 0.61) \times 10^{-3}$ and the inhomogeneous linewidth is $\mu_0 H_{\text{inh}} = (28.6 \pm 1.3)$ mT. Comparing the thus obtained values with the FMR data of the two reference YIG layers shows that the YIG layer fabricated by the two step rapid annealing has a lower Gilbert damping than both reference samples. Due to the rather noisy dataset, care has to be taken in the interpretation of these values. However, the inhomogeneous linewidth broadening is more similar to the film fabricated in oxygen atmosphere than to the one fabricated in argon atmosphere. Therefore, we ex-

pect the sample to have a similar magnetization dynamic than YIG thin films fabricated at a finite substrate temperature in oxygen atmosphere. Comparing the here determined values of the effective magnetization, the Gilbert damping as well as the inhomogenous FMR linewidth, with previous results of YIG films on a GGG substrate, shows an increase in the effective magnetization and the inhomogenous FMR linewidth [21, 24], which might be due to strain in the YIG thin film grown on YAG due to the lattice mismatch of 3.13% between YIG and YAG and the so induced strain in the YIG thin film [73]. The Gilbert damping however is in good agreement with previous results.

4.3.2. Magnetotransport properties

In addition to the bulk magnetic properties of the Pt/YIG/Pt sample, the interface properties between Pt and YIG are investigated by angle-dependent magnetoresistance (ADMR) measurements. For doing so, a current is applied by a Keithley 2400 sourcemeter along the Pt strip or along a Hallbar and the longitudinal voltage is measured using a Keithley 2182 Nanovoltmeter. For the measurement the so called current reversal technique is used, where the applied current polarity is reversed several times. This allows for extraction of the thermal voltage contribution and the electrical voltage contribution. For details about the dc-current reversal technique as well as the extraction of the electrical and thermal voltage contribution see Appendix A.2 The applied external magnetic field is rotated in three different planes which are in-plane (ip), out-of-plane perpendicular to the current direction \mathbf{j} (oopj) and out-of-plane perpendicular to the transverse direction \mathbf{t} (oopt). In Fig. 4.3.9 the electrical voltage of the ADMR measurement performed on a Hallbar on the top Pt layer with a width of 80 μm and length of 600 μm (a)-(c) as well as on the bottom Pt layer (d)-(f) measured along a 1 μm wide and 200 μm long strip via a four-point measurement are shown. An applied magnetic field magnitude of $\mu_0 H = 7 \text{ T}$, well above the saturation field (cf. Fig. 4.3.7) as well as an applied current of $I_{\text{top}} = 100 \mu\text{A}$ at the Hallbar of the top Pt layer and $I_{\text{bot}} = 20 \mu\text{A}$ for the bottom Pt strip was used to reduce heating effects, since the Hallbar on the top Pt layer is much wider than the Pt strips. The measured data are fitted using the angle-dependence of the spin Hall magnetoresistance (SMR) and anisotropic magnetoresistance (AMR) (see Chapter 2.3.1). Where ideally the SMR only contributes in ip and oopj rotations and the AMR only contributes in ip and oopt rotations (see Chapter 2.3.1 and Chapter 2.3.3). However, since Pt is a nonmagnetic material, we do not expect any AMR contributions in an ideal Pt/YIG/Pt heterostructure.

The longitudinal resistivity ρ_{long} is calculated from the electrical voltage contribution and normalized to $\rho_0 = \rho_{\text{long}, H \parallel \mathbf{t}}$. The resistivity of the top Pt layer is determined to $\rho_{\text{top Pt}} = 3.15 \times 10^{-7} \Omega \text{ m}$ whereas the bottom Pt layer shows a slightly increased value of $\rho_{\text{bot Pt}} = 5.27 \times 10^{-7} \Omega \text{ m}$. This might be caused by an increased surface roughness due to the deposition of YIG via PLD. However, both determined values are still in good agreement with previous results [13]. The ADMR measurements of the top Pt layer (Fig. 4.3.9 (a-c)) reveal the in Chapter 2.3.1 described \cos^2 dependence of ρ_{long} while rotating the mag-

netic field in the ip and oopj plane (Figs. 4.3.9 (a) and (b)) of ρ_{long} at all temperatures. However, while rotating the magnetic field in the oopt rotation plane (Fig. 4.3.9 (c)) a small but finite angle-dependence of ρ_{long} is observed above 10 K.

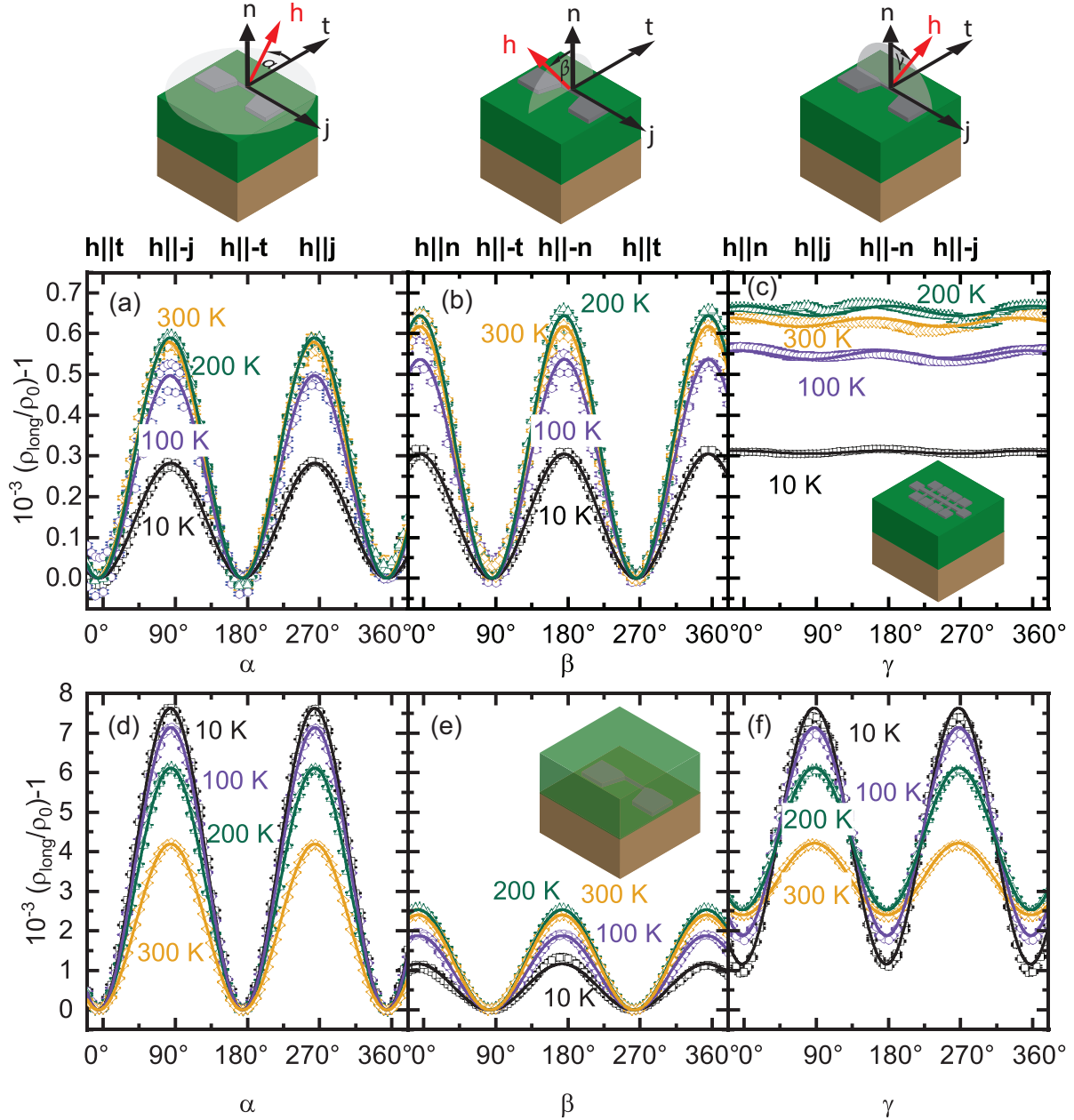


Figure 4.3.9.: Angle-dependent magnetoresistance measurements of a Pt/YIG/Pt/YAG sample on (a)-(c) the top Pt layer and on (d)-(e) the bottom Pt layer using a constant magnetic field magnitude of $\mu_0 H = 7$ T at 10 K, 100 K, 200 K, and 300 K. The magnetic field is rotated in three different planes: (a), (d) in-plane (ip), (b), (e) out-of-plane perpendicular to the current direction \mathbf{j} (oopj) and (c), (f) out-of-plane perpendicular to the transverse direction \mathbf{t} (oopt) as shown above. The data is normalized to $\rho_0 = \rho_{\text{long}, H \parallel \mathbf{t}}$.

Taking into account a small but finite misalignment of the sample during the ADMR

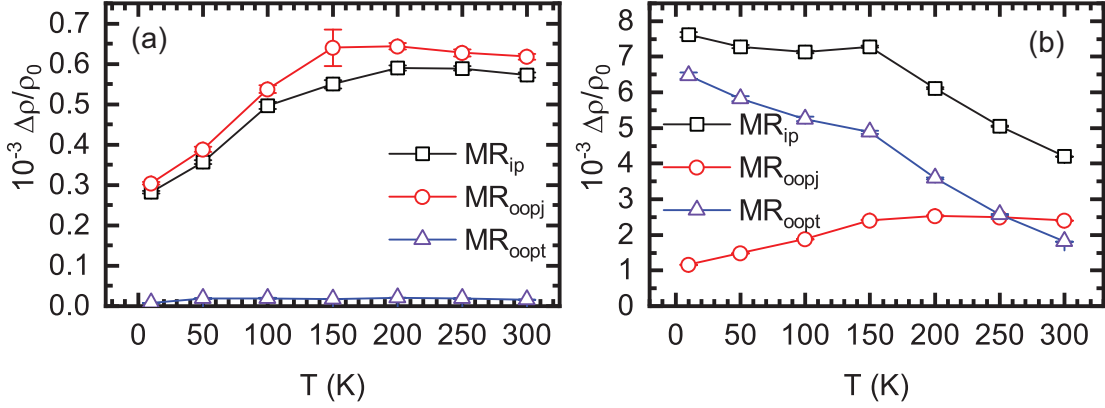


Figure 4.3.10.: MR amplitudes determined from ADMR measurements performed (a) on a Pt Hallbar on the top Pt layer and (b) on a Pt strip on the bottom Pt layer (b) of a patterned Pt/YIG/Pt//YAG heterostructure at $\mu_0 H = 7$ T at different temperatures. The magnetic field is rotated in ip (black squares), oopj (red circles) and oopt (blue triangles) rotation plane. The lines are a guide to the eye.

measurements, the angle-dependence of ρ_{long} can be well described in the framework of the SMR theory (see Chapter 2.3.1). The ADMR data are fitted by \cos^2 functions and the obtained MR amplitudes $\Delta\rho/\rho_0$ are shown in Fig. 4.3.10 (a) as a function of temperature T . The MR amplitude extracted from ip- and oopj-rotations of the magnetic field have a value of $(0.572 \pm 0.006) \times 10^{-4}$ and $(0.617 \pm 0.007) \times 10^{-4}$ at 300 K, respectively, and decrease with decreasing temperatures. This is in agreement with previous results [13, 57]. In particular, the magnitude of the MR amplitude is similar to previous results obtained using Pt/YIG bilayers fabricated by PLD and sputtering with ex-situ interfaces [65]. As obvious from Fig. 4.3.10 (a), the MR-amplitude extracted from ip-magnetic field rotations is slightly decreased compared to that of the oopj rotation, which might be due to the time delay of 2 months between the ip and oopj measurements and therefore a partial oxidation of the top Pt layer. The ADMR measurements of the bottom Pt layer (Figs. 4.3.9 (d)-(f)) shows a distinct angle-dependence of ρ_{long} in all three magnetic-field rotation planes. The data are again fitted using \cos^2 functions (solid lines) and the obtained amplitudes $\Delta\rho/\rho_0$ are shown in Fig. 4.3.10 (b). While the temperature dependence of the MR-amplitude of the oopj-measurement is similar to that measured at the top Pt layer, a clear increase of the MR-amplitude with decreasing temperature with a small change in slope at 150 K is observed in the ip- and oopt-measurements. This might originate from a finite induced magnetic moment in the bottom Pt layer due to intermixing at the interface which is caused by the high kinetic energy of the atoms hitting the surface during deposition of YIG via the PLD process as shown by Gepraegs *et. al* [57] for inverted Pt/YIG bilayers. This leads to a finite AMR contribution and therefore a finite ADMR in oopt-magnetic field rotations. Furthermore, the clear kink observed in the temperature-dependence of the MR-amplitude of the ip measurement can be explained by a superposition of the SMR effect as well as a finite AMR contribution. Therefore, ADMR measurements on the bottom Pt layer reveal a superposition of SMR and AMR demonstrating a finite Pt-magnetic moment, most probably

caused by intermixing at the Pt/YIG interface.

4.4. Conclusion

In this chapter the fabrication of vertical, patterned Pt/YIG/Pt heterostructure was investigated and optimized. As starting point served the work of C. Mang [62]. Therefore, the first Pt/YIG/Pt//GGG heterostructures were fabricated in-situ via electron-beam evaporation as well as pulsed laser deposition followed by a subsequent two-step annealing resulting in in-situ Pt/YIG interfaces. The Pt/YIG/Pt strips are then patterned using Ar-ion milling. However, the YIG thin film was not crystalline and the Pt strips had no electrical contact. Therefore, the fabrication was modified and the lift-off technique was used to define Pt/YIG mesa structures. First, a patterned Pt/YIG/Pt sample was fabricated by using a lift-off process for the bottom Pt layer and then for the top Pt/YIG bilayer. To this end, for the first time a lift-off process was used together with pulsed-laser deposition, where the molecules hit the photoresist with high kinetic energy. This results in an ex-situ interface at the bottom YIG/Pt interface, but allowed for direct contact of the YIG thin film with the GGG substrate. However, the Pt layers had a very high resistance after the PLD process and the subsequent annealing. Therefore, the YIG layer was deposited over the whole sample, further increasing the contact area between the YIG layer and the GGG substrate. Moreover, the annealing step could be ascertained to be the reason for the increase of the Pt resistivity. Thus a lower maximum annealing temperature of the YIG layer was introduced and the top Pt layer was deposited ex-situ after annealing via sputtering. We further changed the substrate material to YAG in order to achieve better crystalline quality of YIG at a lower annealing temperature. This results in Pt/YIG/Pt trilayers with a good crystalline quality of the YIG layer as well as a good conductivity of both Pt layers. From these Pt/YIG/Pt heterostructures the magnetic properties were investigated by SQUID magnetometry and FMR spectroscopy. The saturation magnetization is lower than the bulk value, but still in agreement with previously reported values on YIG layers fabricated via the standard PLD process at finite temperatures. At low temperatures, however, a large exchange bias is found, which might be due to interdiffusion of Al into YIG resulting in an antiferromagnetic Y₃Fe_{5-x}Al_xO₁₂ phase at low temperature. Broad-band FMR measurements reveal a slightly increased effective magnetization as well as of the inhomogeneous FMR linewidth compared to YIG thin films deposited on a GGG substrate using the conventional PLD-process at finite substrate temperatures, which might be mostly due to the lattice mismatch of about 3% between YIG and the used YAG substrate. Moreover, we demonstrated that YIG thin films fabricated at room temperature and subsequent two step rapid annealing in Ar atmosphere are more similar to a reference sample fabricated in oxygen atmosphere than a respective reference sample fabricated in Ar atmosphere using the standard PLD-process at finite substrate temperatures. Furthermore, the interface quality of the top and bottom Pt layers to the YIG layer were investigated by ADMR mea-

4.4. Conclusion

surements. The ADMR measurements of the top Pt layer showed an SMR like behavior and therefore indicated a good interface quality. However, ADMR measurements at the bottom Pt layer revealed an additional AMR most likely due to a FePt-alloy caused by an intermixing at the bottom Pt/YIG interface. Additionally, an electrical short between the bottom and the top Pt strip was measured. These two issues are addressed in the next chapter by further optimization of the properties of the bottom Pt layer as well as changes of the device layout.

5. Optimization of the bottom Pt layer

The previous chapter revealed a finite AMR in the magnetotransport measurements of the bottom Pt layer as well as electrical shorts between the bottom and top Pt layer. To further optimize the YIG/Pt interface, a Ruthenium (Ru) buffer layer is introduced between the bottom Pt layer and the YIG layer as well as between the YAG substrate and the bottom Pt layer to minimize intermixing at these interfaces. In order to reduce electrical shorts between the bottom and top Pt layer, the YIG layer thickness as well as the structure design are modified in the following.

5.1. Minimizing interdiffusion between Pt and $\text{Y}_3\text{Fe}_5\text{O}_{12}$ by Ru buffer layers

In order to reduce the finite intermixing between Pt and YIG (see Fig. 4.3.9 (f)) a Ru buffer layer is introduced first between the bottom Pt layer and the YIG layer and then additionally between the YAG substrate and the Pt layer. This promises to improve the spin mixing conductance [74] and might reduce the AMR signal [62] by reducing the intermixing of Fe from the YIG layer and the Pt layer as well as of Al from the YAG substrate and the Pt layer.

5.1.1. Ru buffer layer between the YIG and the bottom Pt layer

In order to fabricate a patterned Pt/YIG/Ru/Pt//YAG heterostructure, a 1 nm thin Ru layer is sputtered via dc-sputtering in-situ after the deposition of the bottom Pt in the SUPERBOWL sputtering system (see Appendix A.3.3). Subsequently, the remaining patterned Pt/YIG layers are fabricated as described in Chapter 4.3. The structural and magnetic properties of these heterostructures are investigated, followed by magnetotransport measurements.

Structural properties

The structural properties are investigated by XRD and XRR measurements. In Fig. 5.1.1 (a) the XRD data is shown. While the substrate YAG (004) reflection is clearly visible, the YIG (004) thin film reflection with only a small intensity is observable. This indicates a crystalline YIG layer with worse crystalline quality compared to Pt/YIG/Pt//YAG heterostructures without an additional Ru layer. In Fig. 5.1.1 (b) the XRR data are shown (black curve) as well as the simulation by the LEPTOS software. For this simulation the

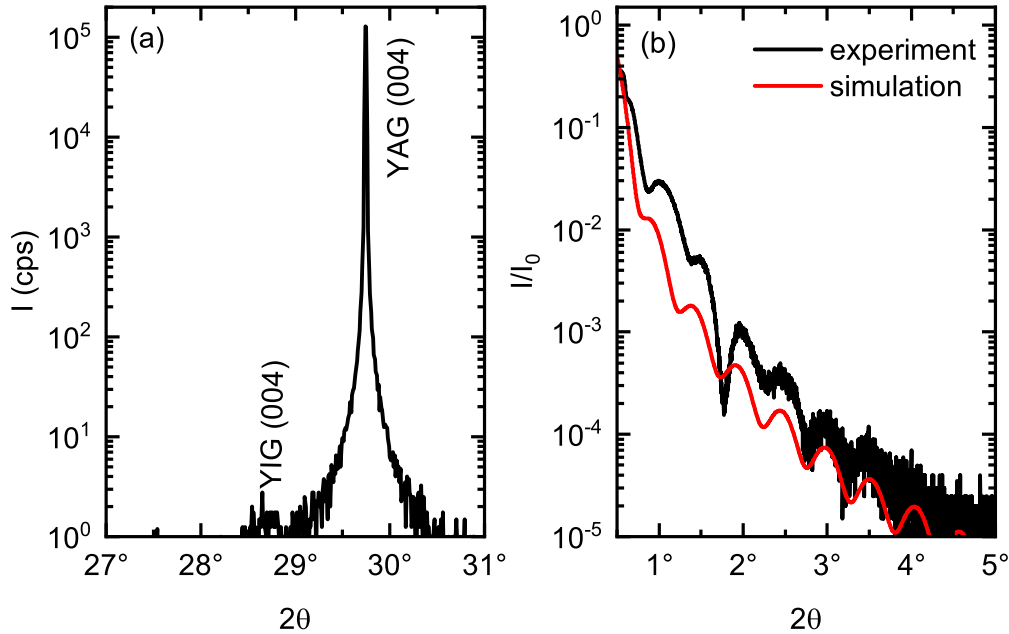


Figure 5.1.1.: Structural properties of a patterned vertical Pt/YIG/Ru/Pt//YAG heterostructure. In (a) the out-of-plane $2\theta - \omega$ scan is shown. In (b) the x-ray reflectometry scan (black curve) is displayed together with the simulation (red curve). From the simulation (red line) the thickness and roughness of the YIG layer is determined. For the simulation a YIG//YAG sample is assumed.

density of the YIG layer has to be increased to $\rho_{\text{YIG}} = (5.7 \pm 0.1) \text{ g cm}^{-3}$ in order to match the experimental data. The reflectometry shows no wide fringes originating from the thin Pt or Ru films most probably due to the small Ru/Pt area on the sample. Therefore, a YIG//YAG layer sequence is assumed for the simulation. The thus obtained thickness of the YIG layer is $t_{\text{YIG}} = (16.3 \pm 0.2) \text{ nm}$ with a roughness of $R_{\text{YIG}} = (0.18 \pm 0.05) \text{ nm}$. The thickness value of the YIG layer is slightly lower than expected for 20000 pulses used for the PLD process. The clear deviation of the experimental data to the simulation at $2\theta \approx 1.5^\circ$ can be attributed to a small but finite contribution from the Ru/Pt layer, which is not taken into account in the simulation.

Magnetic properties

In Fig. 5.1.2 the magnetization curves of a Pt/YIG/Ru/Pt//YAG heterostructure measured at 10 K and at 300 K are shown after the diamagnetic contribution from the YAG substrate is subtracted. It is clearly visible that the saturation magnetization as well as the coercivity increase at low temperatures. Moreover the hysteresis is shifted to negative magnetic fields. At 300 K the saturation magnetization is determined to $M_S = (119.3 \pm 1.5) \text{ kA m}^{-1}$. This is lower than the literature value of $M_{S, \text{lit}} = 143 \text{ kA m}^{-1}$ for bulk-YIG at room temperature [69]. However, it is in agreement with previous results for YIG thin films grown on YAG substrates [57, 63, 68] and slightly higher than the saturation magnetization of Pt/YIG/Pt//YAG samples without Ru buffer layer (see Fig. 4.3.7). From Fig. 5.1.2 (b)

the coercive field at 300 K is determined to $\mu_0 H_c = (6 \pm 2.5)$ mT, which is similar to the coercive field of Pt/YIG/Pt heterostructures (see Fig. 4.3.7). At 10 K the saturation mag-

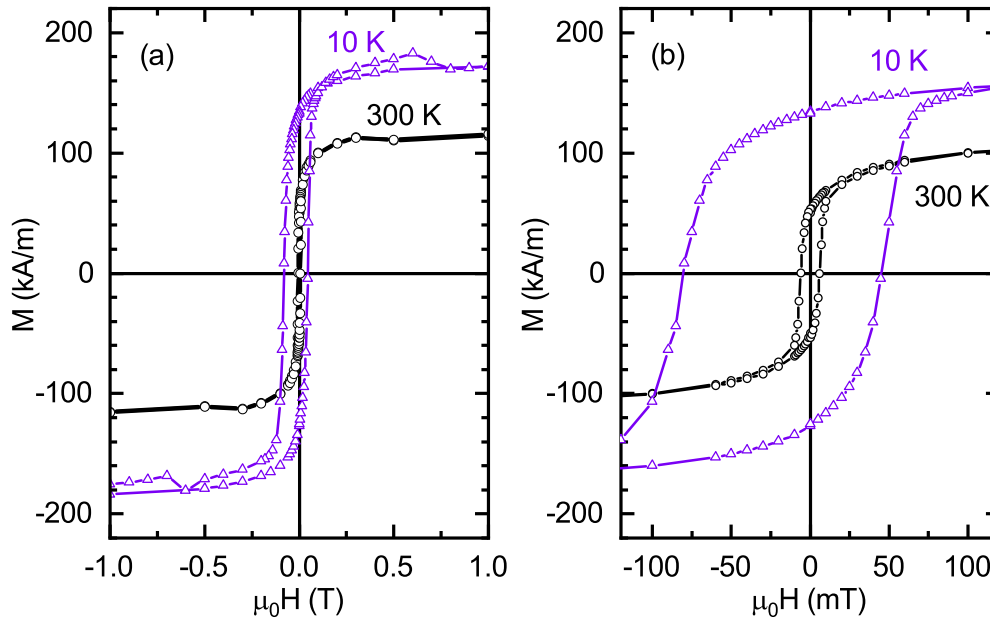


Figure 5.1.2.: (a), (b) In-plane magnetization curves of the Pt/YIG/Ru/Pt//YAG sample. The curves are recorded at 300 K (black curve) and 10 K (blue curve). The field is applied in the film plane and the diamagnetic contribution of the YAG substrate is subtracted.

netization increases to $M_{S,10K} = (189 \pm 2)$ kA m $^{-1}$ which is slightly lower than a previously reported value for a YIG sphere at 10 K of $M_{S,YIG\ sphere} = 194$ kA m $^{-1}$ [70]. However, compared to other YIG thin films deposited on YAG substrates the here measured saturation magnetization is increased [68]. Furthermore, the value is even higher than for the respective Pt/YIG/Pt sample without Ru layer (see Fig. 4.3.7). The hysteresis at 10 K is again shifted towards negative applied fields with $\mu_0 H_{c-} = -(80.8 \pm 2.5)$ mT and $\mu_0 H_{c+} = (45.5 \pm 2.5)$ mT. Thus an exchange bias of $\mu_0 H_{ex} = (17 \pm 5)$ mT can be calculated, which is similar to the exchange bias determined for patterned vertical Pt/YIG/Pt//YAG heterostructures (compare Fig. 5.2.2 (b)). This magnetic field shift is most likely due to an antiferromagnetically ordered layer at low temperatures. As discussed in the previous chapter, it has been reported that Al interdiffusion from the YAG substrate into the first YIG monolayers results in an antiferromagnetically ordered $Y_3Fe_{5-x}Al_xO_{12}$ phase at low temperatures [71]. However, in this case only a small exchange bias in the order of a few mT is reported, while the exchange bias of the Pt/YIG/Ru/Pt//YAG sample is one order of magnitude larger [68, 71]. Another possibility is the formation of RuO_2 , which has been reported to show an antiferromagnetic order [75]. Formation of RuO_2 might be possible due to exposure to air of the Ru/Pt sample after the sputtering deposition to perform the required lift-off process. Oxidation of the Ru layer might be also possible during the PLD

process due to oxygen emanating from the YIG target.

In order to investigate if the additional Ru buffer layer improves the interface quality between the YIG thin film and the bottom Ru/Pt layer, demonstrated in a reduced AMR, magnetotransport measurements are performed.

Magnetotransport properties of the bottom Ru/Pt layer

The magnetotransport properties of the bottom Ru/Pt layer are investigated by angle-dependent magnetoresistance measurements (ADMR). Therefore a hallbar mesa structure on the bottom Ru/Pt layer is connected via Al-wire bonding. The hallbar has a length of $400\ \mu\text{m}$ between two bonding pads and a width of $80\ \mu\text{m}$. The measurements are performed analogous to the ADMR measurements discussed in Chapter 4.3.2.

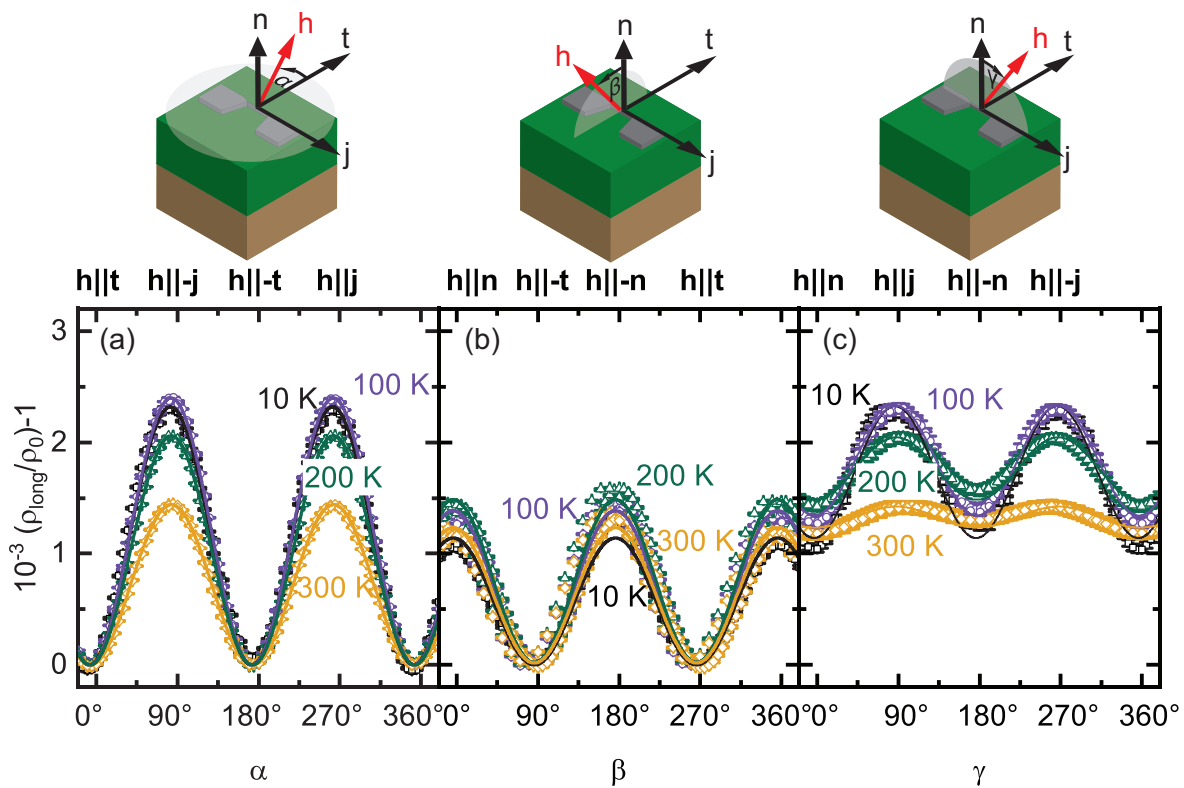


Figure 5.1.3.: Angle dependent magnetoresistance (ADMR) measurements of a vertical Pt/YIG/Ru/Pt/YAG heterostructure on the bottom Ru/Pt bilayer patterned in a Hall bar mesa structure. The measurements are performed at 10 K, 100 K, 200 K and 300 K with an applied magnetic field magnitude of $\mu_0 H = 7\ \text{T}$. The magnetic field is rotated (a) in the film plane (ip), (b) out-of-plane perpendicular to the current direction j (oopj), and (c) out of plane around the transverse direction t (oopt) as shown above.

In Fig. 5.1.3 the data of the ADMR measurements are shown. The applied current is $I_{\text{bot}} = 100\ \mu\text{A}$ and the applied external magnetic field magnitude is $\mu_0 H = 7\ \text{T}$ which is well above the saturation field (see Fig. 5.1.2). The field is rotated in the ip, oopj and oopt planes as shown in the top part of Fig. 5.1.3. From the electrical voltage contribu-

tion (see Appendix A.2) the longitudinal resistivity ρ_{long} is calculated and normalized to $\rho_0 = \rho_{\text{long}, H \parallel t}$. For the Ru/Pt layer ρ_0 is determined to $\rho_{0, \text{Ru/Pt}} = 7.07 \times 10^{-7} \Omega \text{ m}$ which is larger than the resistivity of the bottom Pt layer of the respective Pt/YIG/Pt//YAG sample (see Chapter 4.3.2). To explain this discrepancy a parallel circuit for the resistances of the Pt layer and the Ru layer are assumed in the following. For the Pt layer a resistivity of $\rho_{\text{Pt}} = 3.06 \times 10^{-7} \Omega \text{ m}$ [14] is assumed, whereas for the resistivity of the Ru layer $\rho_{\text{Ru}} = 1.5 \times 10^{-7} \Omega \text{ m}$ [76] is used. This leads to an even lower resistivity of $\rho_{\text{Ru/Pt}} = 2.6 \times 10^{-7} \Omega \text{ m}$. Therefore, the higher resistance of the Ru/Pt layer is most likely caused by a larger resistance of the Ru layer due to oxidation and additional interface scattering.

The ADMR measurements reveal a finite angle-dependence of ρ_{long} while rotating the magnetic field in all three planes (ip, oopj, oopt). Thus, the data are fitted by \cos^2 functions and the extracted MR amplitudes $\Delta\rho/\rho_0$ are shown in Fig. 5.1.4.

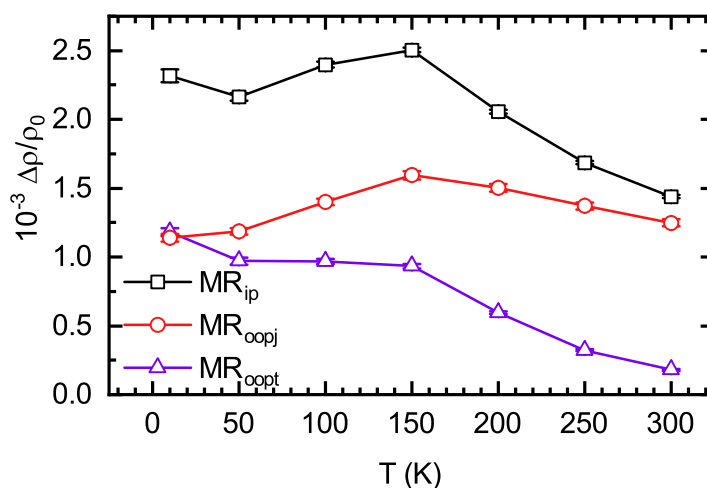


Figure 5.1.4: MR amplitudes extracted by \cos^2 -fits of the ADMR data of a vertical Pt/YIG/Ru/Pt//YAG heterostructure with the Ru/Pt layers patterned into a Hall bar mesa structure measured using a magnetic field magnitude of $\mu_0 H = 7 \text{ T}$ and different temperatures. The magnetic field is rotated in the ip (black squares), oopj (red circles), and oopt (purple triangles) rotation plane. The lines are guides to the eye.

The MR amplitude measured while rotating the magnetic field in the oopj-plane (red curve) shows a slight increase for decreasing temperatures until 150 K and decreases afterwards. This temperature dependence is similar to the expected temperature dependence within the framework of the SMR theory, which we also observed in the respective Pt/YIG/Pt//YAG sample for the bottom and top Pt layer (see Fig. 4.3.10). However, the amplitude is more than a factor of two higher than the expected SMR-amplitude for ex-situ interfaces (cf. Fig. 4.3.10 (a)). This and the slight increase of the amplitude might be due to a finite interdiffusion of YIG in the Ru/Pt layer. This might result in a more complex resistance network and therefore a finite AMR contribution visible also in the oopj-rotation plane of the magnetic field [57]. However, the magnitude of the MR amplitude is lower

than the respective value of the Pt/YIG/Pt//YAG sample without Ru (cf. Fig. 4.3.10 (b)). Therefore, the interdiffusion might be reduced due to the additional Ru layer. The MR amplitude of the oopt-measurement (purple curve) increases with decreasing temperature and therefore fits the expected temperature dependence of a finite AMR. Similar to the trilayer sample without Ru, a kink at 150 K is visible, which might be due to a finite SMR also visible in the oopt-magnetic field rotation plane. As aforementioned, this suggests a more complex resistance network resulting in AMR and SMR contributions to the MR in all three rotation planes of the magnetic field. Compared to the ADMR data of the bottom Pt layer of the Pt/YIG/Pt//YAG heterostructure (see Fig. 4.3.10 (b)) the amplitude is approximately one order of magnitude smaller. A similar small MR amplitude at 300 K has also been reported by C. Mang in a non-patterned YIG/Ru/Pt sample on a GGG substrate [62]. The reduction of the MR amplitude in the oopt-measurement geometry is a clear sign of a reduced intermixing of YIG and Pt due to the additional Ru layer. The MR amplitude of the ip rotation of the magnetic field (black curve) can be understood by a superposition of SMR and AMR. The temperature dependence is similar to that of the bottom Pt layer of a Pt/YIG/Pt//YAG heterostructure (compare Fig. 4.3.9 (b)). Moreover, it shows the same temperature dependence as reported for an inverse, non-patterned YIG/Pt bilayer [57].

Therefore the additional 1 nm Ru buffer layer between YIG and the bottom Pt layer reduces the magnitude of the AMR effect. This might be due to limited interdiffusion from YIG into the Pt thin film.

5.1.2. Additional Ru buffer layer between YAG and Pt

To further optimize the magnetotransport properties of the bottom Pt layer an additional 1 nm thin Ru buffer layer between the YAG substrate and the Pt layer is introduced. This might reduce a possible interdiffusion of Al and oxygen from the YAG substrate into the Pt layer. The Ru/Pt/Ru trilayers are dc-sputtered in-situ without breaking the vacuum in the SUPERBOWL system (see Appendix A.3.3). Subsequently, the Pt/YIG layers on top of the patterned Ru/Pt/Ru trilayer is fabricated as discussed in Chapter 4.3. The thus obtained patterned Pt/YIG/Ru/Pt/Ru//YAG heterostructures are investigated regarding their structural, magnetic and magnetotransport properties.

Structural properties

In Fig. 5.1.5 the structural properties of the patterned Pt/YIG/Ru/Pt/Ru//YAG heterostructure investigated by XRD as well as XRR are shown. The XRD data (Fig. 5.1.5 (a)) reveal the YAG (004) reflection as well as the YIG (004) thin film reflection. From a Gaussian fit, the YIG (004) 2θ angle is determined and the lattice constant is calculated to $a_{\text{YIG}} = (1.231 \pm 0.013)$ nm. This is within the margin of error of the literature value of $a_{\text{YIG, lit}} = 1.2376$ nm [64]. The intensity of the YIG (004) reflection is larger than that of the respective Pt/YIG/Ru/Pt//YAG sample without additional Ru layer. However, it is still

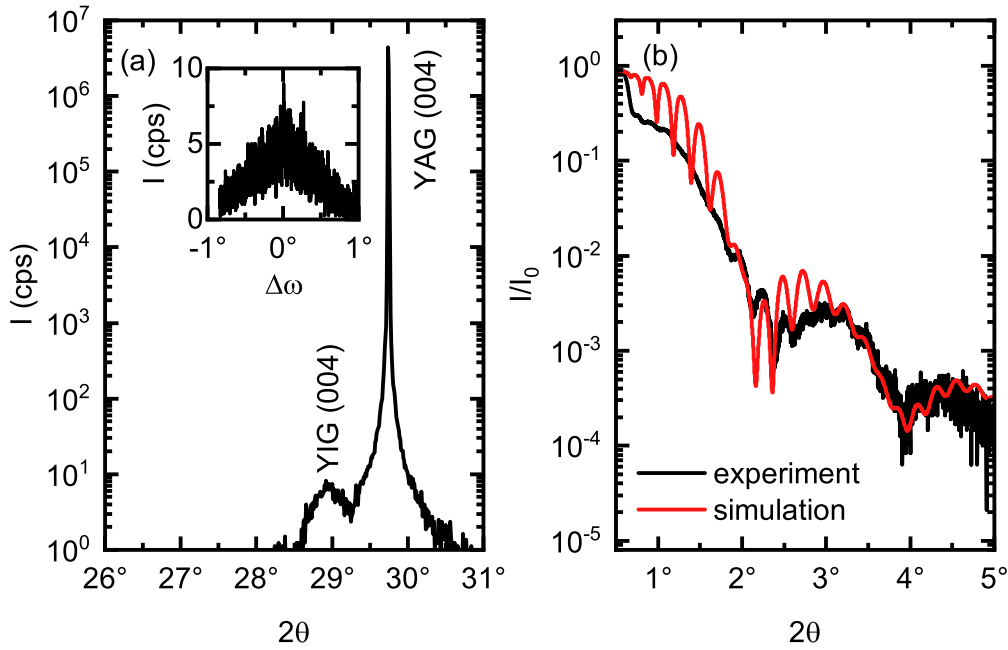


Figure 5.1.5.: Structural properties of a patterned Pt/YIG/Ru/Pt/Ru/YAG heterostructure. Panel (a) shows the out-of-plane $2\theta - \omega$ scan. The inset displays the rocking curve around the YIG (004) reflection. In (b) the x-ray reflectometry scan (black curve) as well as the simulated data (red curve) are plotted against the 2θ angle. For the simulation a Pt/YIG/Ru/Pt/Ru/YAG heterostructure is assumed.

smaller than the sample without any Ru layer. Therefore, the additional Ru layers introduced in the heterostructures might reduce the crystalline quality of the YIG layer. This is also visible in the broad rocking curve around the YIG (004) reflection with a FWHM of $w_{FWHM} = (0.863 \pm 0.019)^\circ$ shown in the inset of Fig. 5.1.1 (a). The thickness and roughness of the YIG layer are determined by an XRR measurement (see Fig. 5.1.5 (b)). For the simulation of the reflectometry data the complete Pt/YIG/Ru/Pt/Ru/YAG layer sequence is assumed since this gave the best match with the experimental data and because the top Pt layer and the bottom Ru/Pt/Ru trilayer cover the same area of the sample surface for this sample. Moreover the density of the YIG thin film had to be increased to $(7.5 \pm 0.1) \text{ g cm}^{-3}$. The simulation fits the experimental data well for $2\theta > 3^\circ$. However, at small 2θ angles there is a discrepancy between both curves due to the small fringes being much more pronounced in the simulated data. Moreover the sharp intensity decrease in the experimental data at $2\theta \approx 0.6^\circ$ can't be described by the simulation. This can be understood by the fact that the simulation assumes a non-patterned heterostructure. Thus simulating a larger contribution from the Pt and Ru layers. However the width of the fringes of the simulation data and the experimental data is a good match. Moreover the determined values fit well to the expected values of $t_{Pt} = 5 \text{ nm}$ and $t_{Ru} = 1 \text{ nm}$ as well as to the expected thickness of the YIG layer between 20 nm and 30 nm (see Table 5.1.1).

Additionally to the structural properties the magnetic properties of the Pt/YIG/Ru/Pt/Ru

layer	thickness	roughness
top Pt	(4.7 ± 0.1) nm	(0.18 ± 0.05) nm
YIG	(28.3 ± 0.2) nm	(0.37 ± 0.05) nm
Ru	(0.9 ± 0.1) nm	(0.68 ± 0.05) nm
bottom Pt	(4.5 ± 0.2) nm	(0.73 ± 0.06) nm
Ru	(1.1 ± 0.1) nm	(0.50 ± 0.05) nm

Table 5.1.1.: Thickness and roughness values obtained from the simulation of the XRR data of a patterned Pt/YIG/Ru/Pt/Ru//YAG heterostructure.

heterostructure are investigated at 300 K and at 10 K.

Magnetic properties

The magnetic properties of the Pt/YIG/Ru/Pt/Ru sample are investigated by SQUID magnetometry (see Appendix A.4.4).

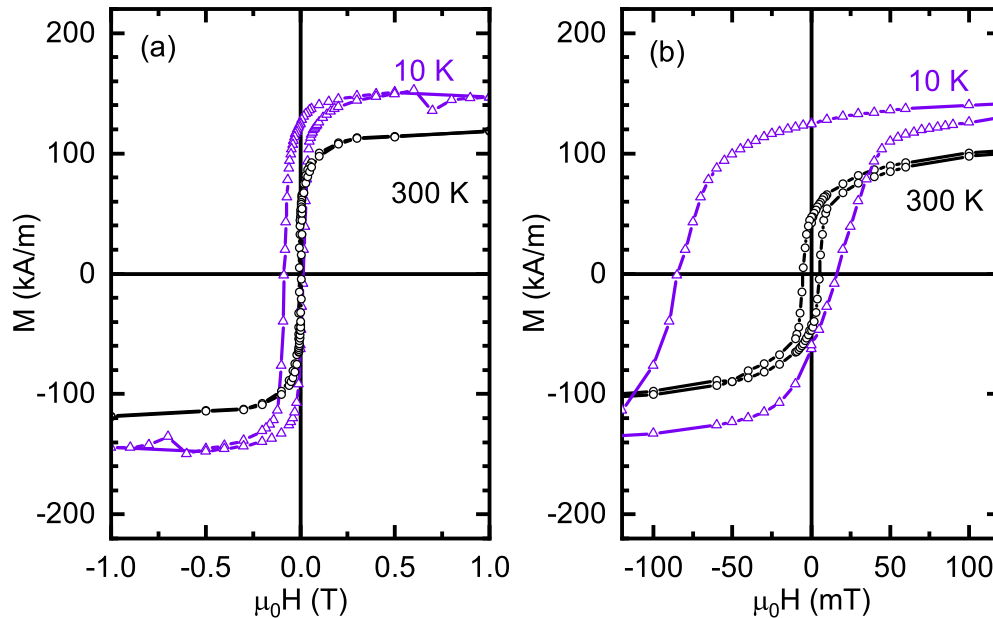


Figure 5.1.6.: (a), (b) In-plane magnetization hysteresis loops of the Pt/YIG/Ru/Pt/Ru//YAG sample. The curves are recorded at 300 K (black curve) and 10 K (purple curve). The diamagnetic contribution of the YAG substrate is subtracted.

In Fig. 5.1.6 the magnetization hysteresis loops of the patterned Pt/YIG/Ru/Pt/Ru//YAG heterostructure at 10 K (purple triangles) as well as at 300 K (black circles) are shown after subtracting the diamagnetic contribution from the YAG substrate. At 10 K the saturation magnetization is determined to $M_{S, 10 K} = (146 \pm 3)$ kA m⁻¹ whereas at 300 K the saturation magnetization is found to be $M_{S, 300 K} = (116 \pm 2)$ kA m⁻¹. The saturation magnetization at 300 K is in agreement with previously reported values for YIG grown on YAG substrates [57, 63, 68], while at 10 K it is decreased when compared to previous results [68] and to the

reported value for bulk YIG [69]. More important, the large M_S -value found at 10 K for the Pt/YIG/Ru/Pt//YAG sample without the additional Ru layer is reduced, which might be due to a reduced intermixing at the Pt/YAG interface. Fig. 5.1.6 (b) shows a zoomed in view around zero field. At 300 K the hysteresis is centered around 0 T and the coercive field is determined to $\mu_0 H_{c, 300 K} = (5 \pm 2)$ mT which is similar to the previous results (compare Fig. 4.3.7). However the hysteresis of the heterostructure is again broadened and shifted to negative applied fields at 10 K with an exchange bias of $\mu_0 H_{ex} = (34 \pm 5)$ mT. This is even larger than the value obtained for the respective Pt/YIG/Ru/Pt//YAG sample (compare Fig. 5.1.2). Therefore, the additional Ru layer between the YAG substrate and the Pt layer could not reduce the large exchange bias at 10 K observed in Pt/YIG/Pt as well as Pt/YIG/Ru/Pt heterostructures. An additional possibility to the aforementioned intermixing of the YIG layer and the YAG substrate for the exchange bias here, could be RuO_x , since an antiferromagnetic ordering could be found recently in oxidized Ru [75].

Magnetotransport properties of the bottom Ru/Pt/Ru layers

Next the magnetotransport properties of the bottom Ru/Pt/Ru trilayer are investigated and compared to the result of the bottom Pt layer and a Ru/Pt bilayer of the respective Pt/YIG/Pt and Pt/YIG/Ru/Pt heterostructures. This is done by ADMR measurements as described in Chapter 4.3.2. In Fig. 5.1.7 the ADMR data of the bottom Ru/Pt/Ru trilayer of a vertical Pt/YIG/Ru/Pt/Ru//YAG heterostructure are shown. A current of 20 μ A is applied along a 200 μ m long and 1 μ m wide Ru/Pt/Ru strip. The applied magnetic field with a magnitude of 7 T is rotated in the ip (a), oopj (b) and oopt (c) rotation planes as shown in the top part of Fig. 5.1.7. The longitudinal voltage is measured via a 4-point measurement and the electrical contribution (see Appendix A.2) calculated into the longitudinal resistivity ρ_{long} . This is then normalized to ρ_0 . The calculated resistivity at 300 K is $\rho = 3.98 \times 10^{-7} \Omega m$. Comparing this to the values of the bottom Pt layer of the heterostructure without Ru layers (see Chapter 4.3.2) as well as to the Ru/Pt layer of the respective Pt/YIG/Ru/Pt heterostructure (see Chapter 5.1.1), a reduction of the resistivity is observed due to the additional, second Ru layer. This seems counterintuitive since through the introduction of the first Ru buffer layer the specific resistivity increased compared to the single Pt layer. However, this might be due to the fact that roughness effects might play a smaller role in the Ru layer between the YAG substrate and the Pt layer since this layer is better protected from the PLD process. Furthermore, the first Ru layer is covered by the Pt layer minimizing oxidation of the Ru layer. However, the resistivity is still slightly larger compared to the value of $\rho_{estimated} = 2.36 \times 10^{-7} \Omega m$ calculated by assuming a parallel circuit and literature values of Pt and Ru [14, 76]. Therefore, finite oxidation effects of the second Ru layer can be assumed.

The longitudinal resistivity ρ_{long} shown in Fig. 5.1.7 exhibits a distinct angle-dependence while rotating the magnetic field in the ip, oopj and oopt rotation planes. These are fitted by \cos^2 functions according to Chapter 2.3.1 and Chapter 2.3.3 and the determined MR

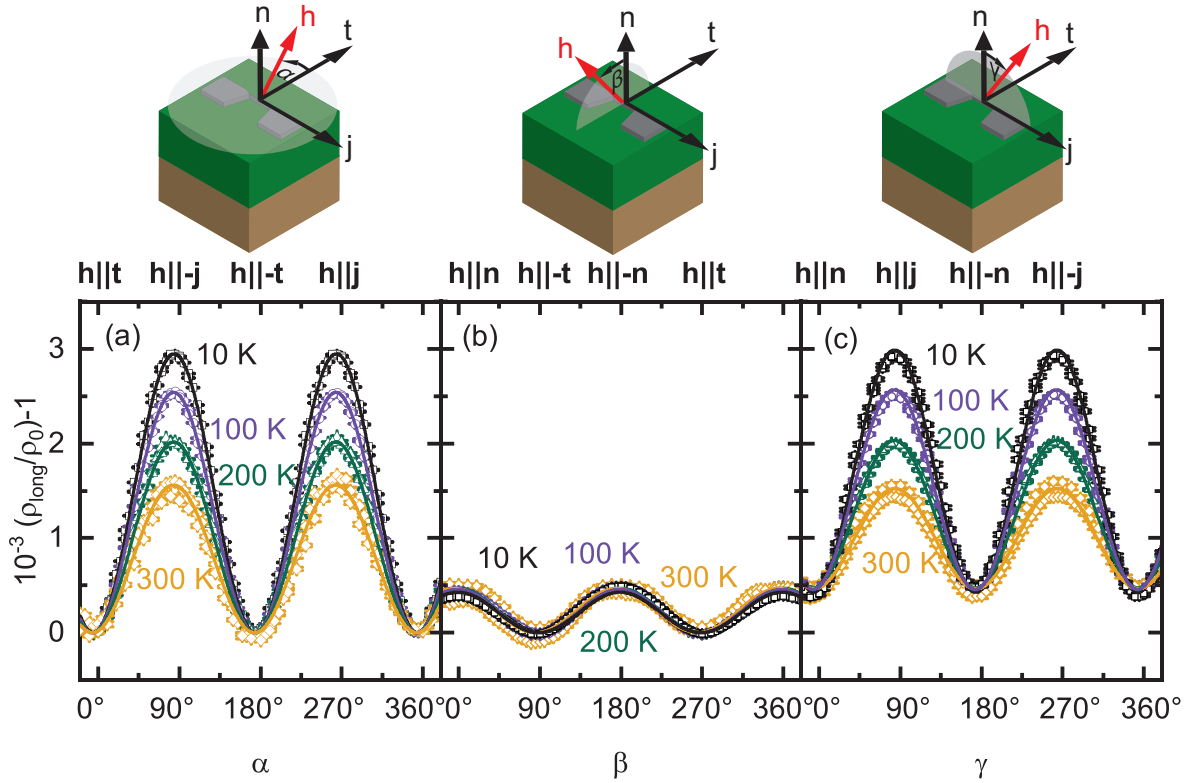


Figure 5.1.7.: Angle dependent magnetotransport (ADMR) measurements of a Pt/YIG/Ru/Pt/Ru//YAG heterostructure measured on the patterned Ru/Pt/Ru strip at 10 K (black squares), 100 K (purple circles), 200 K (green triangles) and 300 K (orange rhombus). The magnitude of the applied magnetic field is $\mu_0 H = 7$ T. The magnetic field is rotated (a) in the film plane (ip), (b) out-of-plane perpendicular to the current direction j (oopj), and (c) out of plane perpendicular to the transverse direction t (oopt) as shown above.

amplitudes $\Delta\rho/\rho_0$ are plotted in Fig. 5.1.8.

The MR amplitude (red circles) of the ADMR measurement, using the oopj rotation plane, shows contrary to the previous results no temperature dependence and stays approximately constant. Moreover, the amplitude is significantly smaller compared to the respective amplitude of the Ru/Pt bilayer shown in Fig. 5.1.4. This might be due to the Ru layer covered by Pt, which has a higher conductivity leading to an electrical shunt of the electrical current. The MR amplitude of the oopt ADMR measurement (purple triangles) shows a linear increase with decreasing temperature and therefore fits the expected behavior for a finite AMR. However, contrary to the almost vanishing AMR amplitude at 300 K of the Ru/Pt layer of the Pt/YIG/Ru/Pt heterostructure (see Fig. 5.1.4), the MR amplitude has a large value at 300 K. The temperature dependence of the MR amplitude of the ip ADMR measurement can be understood by a superposition of the MR amplitudes of the oopj- and oopt-ADMR measurements. However, no clear sign of a finite SMR contribution is visible in the temperature dependence of the MR amplitudes, which would be identifiable by a kink at around 150 K (see Fig. 4.3.10 (b) and Fig. 5.1.4). Therefore, the Ru layer deposited on the YAG substrate and in-situ covered by the Pt layer may result in an

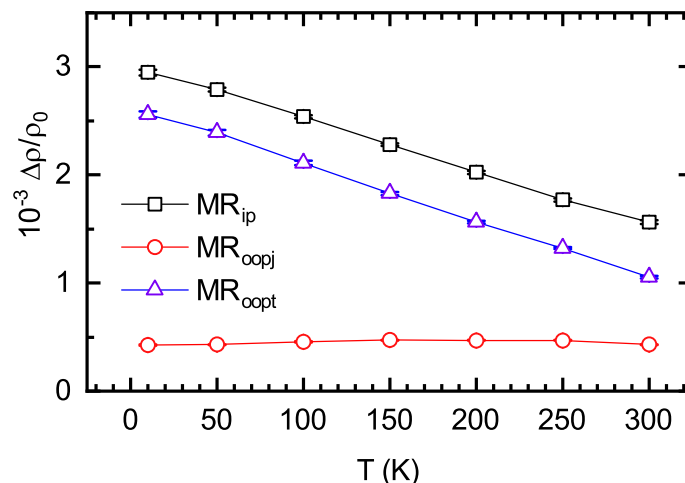


Figure 5.1.8: MR amplitudes extracted from ADMR measurements performed on a patterned Ru/Pt/Ru strip of a Pt/YIG/Ru/Pt/Ru//YAG heterostructure at different temperatures using a magnetic field magnitude of 7 T. The magnetic field is rotated in ip (black squares), oopj (red circles) and oopt (purple triangles) rotation planes. The lines are guides to the eye.

electrical shunt of the current leading to a non-SMR like behavior.

5.2. Addressing electrical shorts between the bottom and top Pt layers

Additional to the observed finite AMR at the YIG/Pt interface, electrical shorts occurred between the bottom and top Pt layers most likely due to growth defects such as nodular defects, pinholes, pores, and other coating discontinuities of the interjacent YIG layer (see Chapter 4.3). To increase the resistivity of the YIG layer, first a thicker YIG layer is deposited. Second, the Pt strips are shortened to reduce the lateral area of the Pt/YIG/Pt trilayer.

5.2.1. Increasing the thickness of the YIG layer

By increasing the thickness of the YIG layer the distance between the Pt strips is increased and therefore the likelihood of an electrical short through pinholes reduced. Thus the number of pulses for the PLD process is doubled. This leads to an expected thickness of the YIG layer of approximately $t_{\text{YIG, expected}} = 70$ nm. The Pt/YIG/Pt//YAG heterostructure with thicker YIG layer is investigated regarding its structural and magnetic properties.

Fig. 5.2.1 shows the structural properties investigated by XRD and XRR measurements. The XRD data (Fig. 5.2.1 (a)) show the YAG (004) substrate as well as the YIG (004) reflection. Alongside the YIG film reflection Laue oscillations (indicated by arrows in Fig. 5.2.1) are observed, indicating a YIG layer with high crystalline quality. Moreover the data ob-

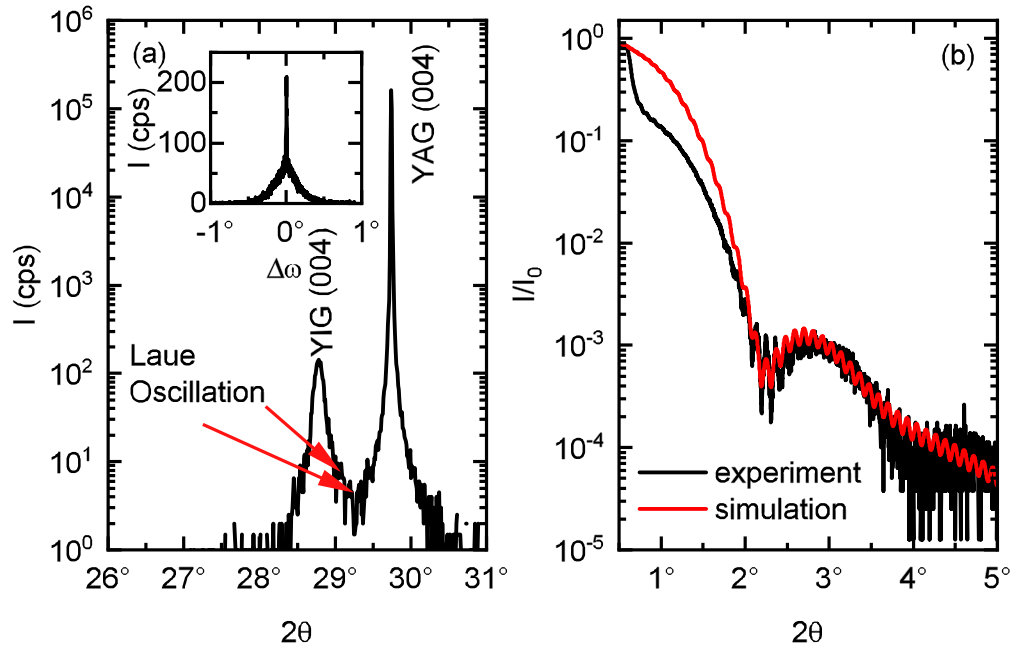


Figure 5.2.1.: Structural properties of a Pt/YIG/Pt//YAG heterostructure with a thicker YIG layer compared to the heterostructure discussed in Chapter 4.3. In (a) the out-of-plane $2\theta - \omega$ scan is shown. The inset displays the rocking curve around the YIG (004) reflection. In (b) the x-ray reflectometry scan (black line) as well as simulated data (red line) is plotted against the 2θ angle. For the simulation a Pt/YIG//YAG bilayer is assumed. From the simulation the thickness and roughness of the layers are determined.

tained from the rocking curve around the YIG (004) reflection (inset in Fig. 5.2.1 (a)) show a double peak structure. The broad peak has a FWHM of $w_{\text{FWHM, broad}} = (0.315 \pm 0.013)^\circ$ indicating a high mosaic spread. This might come from the first few strained monolayers due to the large lattice mismatch of 3%. The other very thin peak has a much higher intensity with a FWHM of $w_{\text{FWHM, thin}} = (0.014 \pm 0.001)^\circ$. Thus indicating a high quality crystalline YIG thin film. Compared to the XRD data of a patterned, vertical Pt/YIG/Pt//YAG heterostructure with a thinner YIG layer, the sharp peak in the rocking curve (compare inset of Fig. 4.3.5 (a)) is much more pronounced. This indicates that a higher crystalline quality can be achieved by increasing the thickness of the YIG thin film. The 2θ angle of the YIG (004) reflection is determined by a Gaussian fit. From the 2θ angle the lattice constant of the YIG thin film is calculated to $a_{\text{YIG}} = (1.239 \pm 0.002)$ nm. This is within the margin of error to the literature value $a_{\text{YIG, lit}} = 1.237$ nm [64]. In Fig. 5.2.1 (b) the XRR data of the patterned Pt/YIG/Pt//YAG heterostructure (black curve) as well as simulated data (red curve) are shown. For the simulation a Pt/YIG//YAG bilayer is assumed. The discernible Pt fringes are due to the hallbar mesa structures of the top Pt layer leading to 5.4% of the area covered by the top Pt layer whereas the bottom Pt layer only covers 1.4% of the sample surface. Moreover, in order to get a good match to the experimental data the density of the YIG film was increased in the simulation to $\rho_{\text{YIG}} = (6.9 \pm 0.2)$ g cm $^{-3}$. At small angles

the simulation data does not fit the experiment well. This can again be attributed to the simulation of non-patterned layer sequences by the LEPTOS software. Thus leading to an increased contribution from the Pt layer. However, apart from this deviation at small 2θ angles the simulation data fit the experimental data well and the thickness and roughness of the YIG layer and top Pt layer can be extracted. The determined thickness of the Pt layer is $t_{\text{Pt}} = (4.5 \pm 0.3)$ nm with a roughness of $R_{\text{Pt}} = (0.84 \pm 0.04)$ nm. This matches the set thickness of 5 nm for the sputtering process. The YIG layer is $t_{\text{YIG}} = (77.3 \pm 0.3)$ nm with a roughness of $R_{\text{YIG}} = (0.23 \pm 0.03)$ nm. Therefore the YIG layer matches the expected thickness and is approximately double the thickness as compared to the respective Pt/YIG/Pt//YAG heterostructure discussed in Chapter 4.3.

The magnetic properties of the Pt/YIG/Pt//YAG heterostructure with the 77 nm thick YIG layer are investigated by measuring the magnetization hysteresis loop at 300 K as well as at 10 K in a SQUID magnetometer (see Appendix A.4.4). The external magnetic field is applied in the film plane (ip). The measured hysteresis loops are shown in Fig. 5.2.2 after

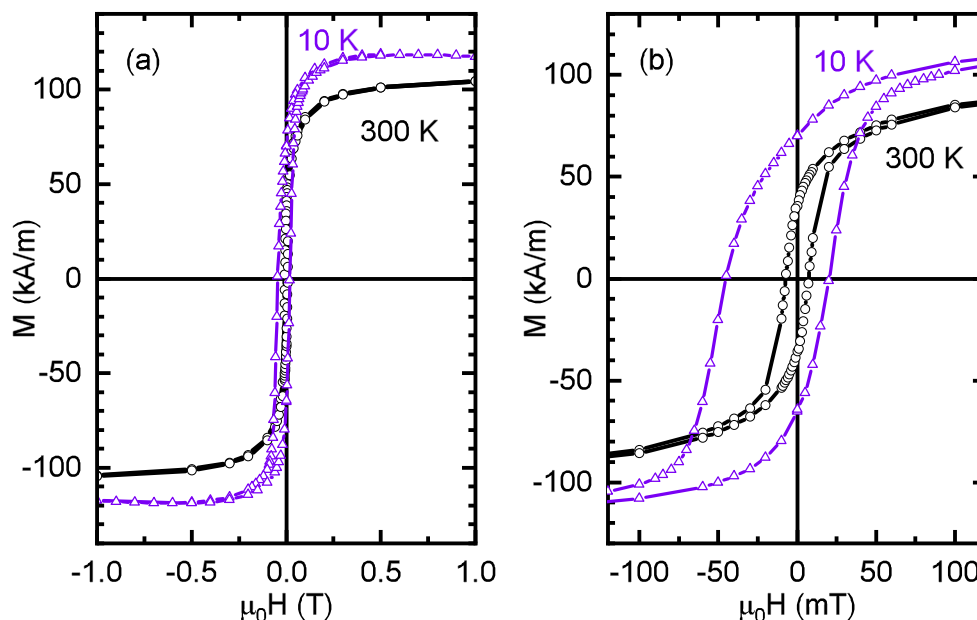


Figure 5.2.2.: (a), (b) Magnetization curves of a Pt/YIG/Pt//YAG heterostructure with a approx. 77 nm thick YIG layer. The field is applied in the film plane and the diamagnetic contribution of the YAG substrate is subtracted.

subtraction of the diamagnetic signal from the YAG substrate. Fig. 5.2.2 (a) shows the range from -1 T to 1 T from which the saturation magnetization is determined. Fig. 5.2.2 (b) shows a zoomed in view around zero magnetic field from which the coercive field is obtained. At 300 K the saturation magnetization is $M_{\text{sat}, 300 \text{ K}} = (102 \pm 1) \text{ kA m}^{-1}$. This is significantly lower than the literature value for bulk-YIG of $M_{\text{S, lit}} = 143 \text{ kA m}^{-1}$ at room temperature [69]. However, it is in agreement with the in this work achieved results (compare Fig. 4.3.7) as well as with previously reported values for YIG thin films deposited

on YAG substrates [57, 63, 68]. The coercive field is $\mu_0 H_{c, 300\text{ K}} = (7.2 \pm 0.1)$ mT. This is in agreement with the previously determined values. At 10 K (purple curve) the saturation magnetization increases to $M_{\text{sat}, 10\text{ K}} = (118.0 \pm 0.2)$ kA m⁻¹ due to less disorder of the magnetic moments through thermal effects. However, previously reported saturation magnetizations for bulk YIG at 10 K are significantly larger with $M_{\text{S, YIG sphere}} = 194$ kA m⁻¹ [70]. The coercive field at 10 K is $\mu_0 H_{c-, 10\text{ K}} = (84.6 \pm 2)$ mT for negative applied fields and $\mu_0 H_{c+, 10\text{ K}} = (16.4 \pm 2)$ mT for positive applied magnetic fields leading to a coercive field of $\mu_0 H_{c, 10\text{ K}} = (33 \pm 1)$ mT of the not shifted hysteresis and an exchange bias of $\mu_0 H_{\text{ex}} = (12 \pm 1)$ mT. These values are larger than previously reported by S. Altmannshofer [68]. This might be due to the fabrication technique of the two step rapid annealing process which might introduce more crystalline defects such as grain boundaries. Moreover the hysteresis at 10 K is again shifted towards negative fields, which might be again explained by interdiffusion of Al into the first monolayers of the YIG thin film creating a Y₃Fe_{5-x}Al_xO₁₂ phase [71]. As discussed already in Chapter 4.3.1, another possibility might be the formation of a Pt₃Fe alloy by interdiffusion of the bottom Pt and YIG which has been reported to show an antiferromagnetic order at low temperatures [72]. However, one should keep in mind that the bottom Pt layer only covers 1.5% of the sample. Therefore, this is expected to have a rather small effect on the magnetic response of the whole YIG thin film.

Electrical properties

The patterned Pt/YIG/Pt//YAG heterostructure with an approx. 77 nm thick YIG layer is connected via Al wire bonding and the resistance along the Pt strips as well as between the top and bottom Pt strips is measured. The resistivity of the bottom Pt layer is $\rho_{\text{bottom Pt}} = 7.36 \times 10^{-7}$ Ω m whereas the resistivity of the top Pt layer is $\rho_{\text{top Pt}} = 2.69 \times 10^{-7}$ Ω m. This is in agreement with previously reported values for 5 nm thick Pt layers [13, 14]. However, measuring the resistance between the bottom and top Pt layer gives a resistance in the kΩ range, which is in the same order as the resistance of the Pt strips. Therefore, solely increasing the thickness of the YIG thin film does not solve the issue of electrical shorts between the bottom and top Pt layer.

5.2.2. Reducing the lateral area of the bottom and top Pt layers

In the next step, we reduced the lateral area of the top and bottom Pt strips. To this end, the length of the strips is reduced from initially 400 μm to a range from 1 μm to 8 μm.

Structural properties

The patterned vertical Pt/YIG/Pt//YAG heterostructure with short Pt strips is investigated by XRD and XRR measurements shown in Fig. 5.2.3.

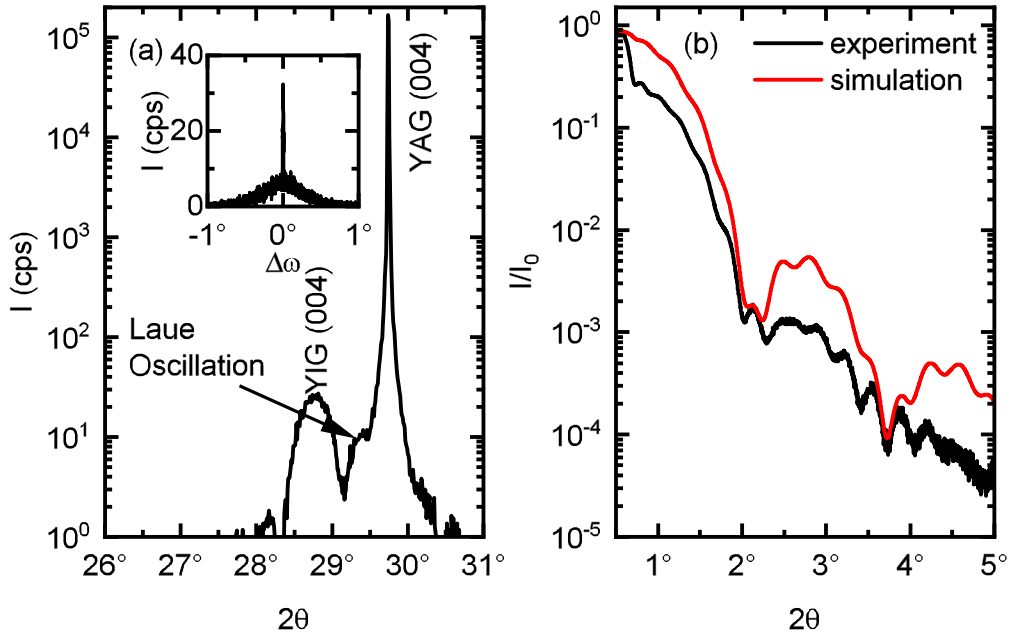


Figure 5.2.3.: Structural properties of Pt/YIG/Pt//YAG heterostructure with short Pt strips. (a) shows the out-of-plane 2θ - ω scan. The inset displays the rocking curve around the YIG (004) reflection. In (b) the x-ray reflectometry data (black curve) and simulated data (red curve) are plotted against the 2θ angle. For the simulation a Pt/YIG//YAG bilayer is assumed. From the simulation (red line) the thickness and roughness of the layers are determined.

The XRD data (Fig. 5.2.3 (a)) show the YAG (004) substrate reflection as well as the YIG (004) film peak. Moreover, Laue oscillations (indicated by the arrow) are clearly visible, which indicates a good crystalline quality of the YIG layer. The YIG (004) peak is fitted by a Gaussian function and the 2θ angle of the YIG (004) reflection is extracted. With the thus obtained 2θ -angle the lattice constant of the YIG thin film is calculated to $a_{\text{YIG}} = (1.240 \pm 0.005)$ nm which is within the margin of error of the literature value [64]. In the inset of Fig. 5.2.3 (a) the rocking curve around the YIG (004) peak is shown. There is a double peak visible with a broad and a shallow peak similar to the heterostructures on YAG substrates discussed before. The FWHM of the broad peak is $w_{\text{FWHM, broad}} = (0.516 \pm 0.06)^\circ$ originating from the first few monolayers of YIG which are strained due to the large lattice mismatch of 3% of YIG to the YAG substrate. The shallow peak has a FWHM of $w_{\text{FWHM, thin}} = (0.013 \pm 0.001)^\circ$. Thus indicating a YIG thin film with high crystalline quality. In Fig. 5.2.3 (b) the XRR data (black curve) as well as simulated data (red curve) are shown. For the simulation a Pt/YIG//YAG bilayer is assumed due to the larger area of Pt covering the top part of the YIG layer compared to the bottom Pt layer (9.8% for the top layer and 5.9% for the bottom Pt layer). In the simulation the density of the YIG thin film had to be increased to $\rho_{\text{YIG}} = (7.5 \pm 0.1)$ g cm $^{-3}$ in order to fit the data from the experiment. The simulated data fit the experiment well apart from the sharp decrease at small 2θ angles and the larger intensity compared to the experimental data. This might again

be explained by the patterned Pt layers compared to the continuous YIG layer. From the simulation the thickness of the YIG layer is determined to $t_{\text{YIG}} = (19.3 \pm 0.2)$ nm with a roughness of $R_{\text{YIG}} = (0.35 \pm 0.03)$ nm whereas the thickness of the Pt layer is determined to $t_{\text{Pt}} = (4.9 \pm 0.1)$ nm with a roughness of $R_{\text{Pt}} = (0.17 \pm 0.03)$ nm. The thickness of the Pt layer matches well with the set thickness for the sputter process of 5 nm. However the determined thickness of the YIG layer is slightly lower than we would expect from the number of pulses used in the PLD process (see Chapter 4.1).

The patterned vertical Pt/YIG/Pt//YAG heterostructure with the short Pt strips is then connected via Al wire bonding and the resistance is measured. For the bottom Pt layer we obtain a resistivity of $\rho_{\text{Pt, bot}} = 7.97 \times 10^{-7} \Omega \text{ m}$ and for the top Pt layer of $\rho_{\text{Pt, top}} = 4.74 \times 10^{-7} \Omega \text{ m}$. Measuring the resistance between the bottom and top Pt layer now gives rise to a resistance in the order of a few M Ω . Therefore decreasing the lateral Pt area improved the issue regarding electrical shorts between the top and bottom Pt layers. Additionally magnetotransport properties of this patterned vertical Pt/YIG/Pt//YAG heterostructure with short Pt strips are investigated.

Magnetotransport properties

The magnetotransport properties are investigated by ADMR measurements (see Fig. 5.2.4). The ADMR measurements are performed on the bottom as well as on the top Pt layer. Therefore a current of 20 μA is applied on the 8 μm long and 1 μm wide Pt strips. As mentioned before the dc current reversal technique is utilized to separate the electrical from the thermal contributions (see Appendix A.2). The voltage is measured via a four-point measurement using a Keithley 2182 nanovoltmeter. A constant magnetic field of $\mu_0 H = 7 \text{ T}$ is applied and rotated in the ip (Fig. 5.2.4 (a,d)), oopj (Fig. 5.2.4 (b,e)) and oopt (Fig. 5.2.4 (c,f)) rotation plane. The electrical contribution of the measured longitudinal voltage is calculated into the longitudinal resistivity ρ_{long} and normalized to $\rho_0 = \rho_{\text{long, H} \parallel \text{t}}$. At 300 K the resistivity of the bottom Pt layer is $\rho = 7.26 \times 10^{-7} \Omega \text{ m}$. This is slightly increased compared to previously reported resistivities by Meyer *et. al* [13]. However, this slight increase might be attributed to roughness effects. On the top Pt layer the resistivity is $\rho_{\text{top}} = 4.32 \times 10^{-7} \Omega \text{ m}$ which is agreement with previously reported values [13, 14]. The ADMR data of the top Pt strips (Fig. 5.2.4 (a-c)) reveal an angle-dependence of ρ_{long} in all three rotation planes. The finite ADMR in ip and oopj rotations (Figs. 5.2.4 (a), (b)) is in accordance with the SMR model from Chapter 2.3.1. However, in contrast to the ADMR of the top Pt layer of Pt/YIG/Pt heterostructures with 400 μm long strips discussed in Chapter 4.3.2, a finite angle-dependence of ρ_{long} is also observable in the oopt-measurement geometry. The angle-dependence in the oopt rotation is therefore not in agreement with the SMR model. It can moreover not be explained by an AMR effect since the angle dependence here has a phase shift of 90° compared to the expected AMR behaviour (see Chapter 2.3.3).

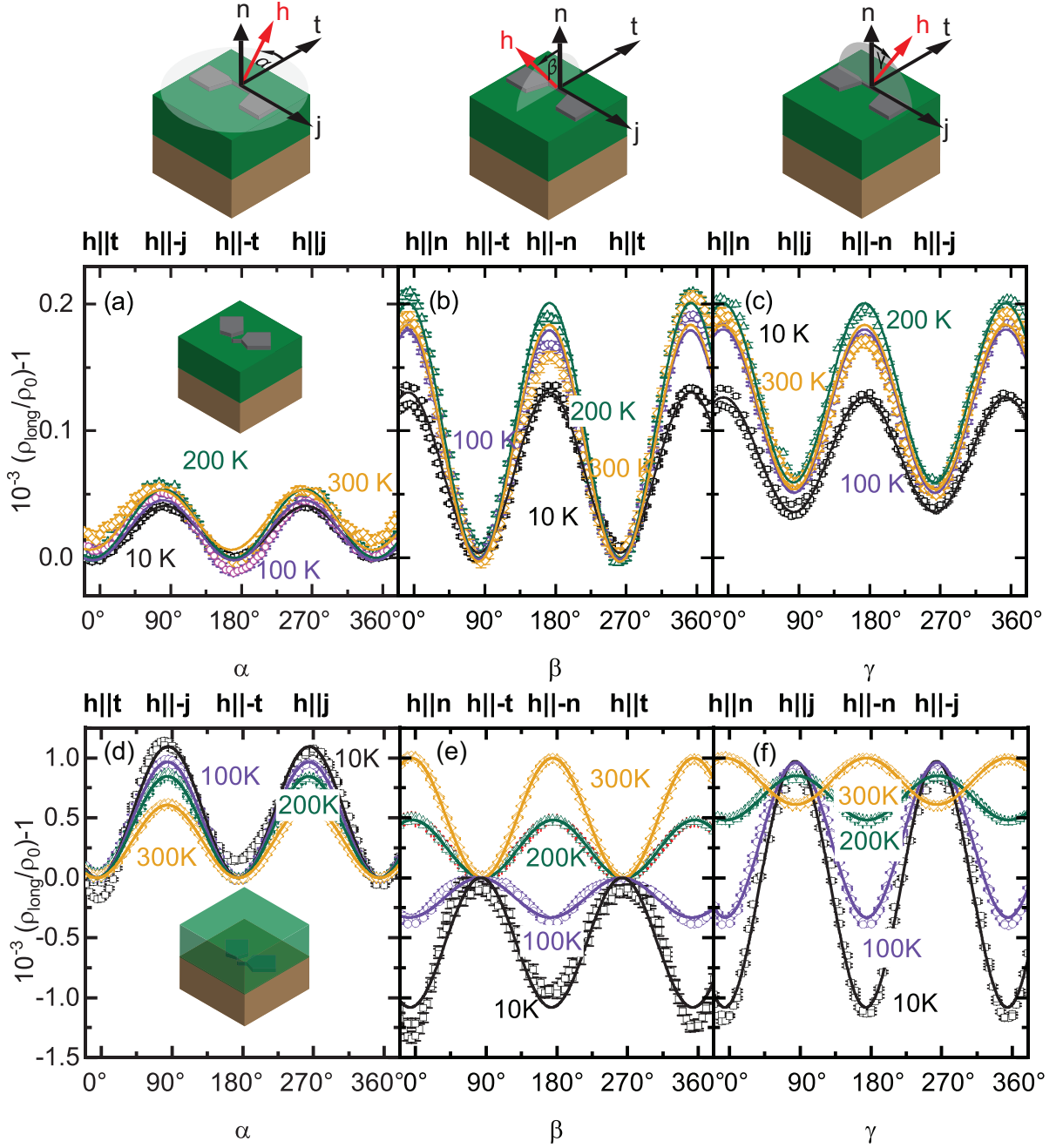


Figure 5.2.4.: Angle-dependent magnetotransport (ADMR) measurements of a patterned Pt/YIG/Pt/YAG heterostructure measured on a 8 μm long and 1 μm wide top Pt strip (a-c) and bottom Pt strip (d-f) at 10 K (black squares), 100 K (purple circles), 200 K (green triangles) and 300 K (orange rhombus). The applied external magnetic field is $\mu_0 H = 7 \text{ T}$. The magnetic field is rotated in the film plane (ip) (a), (d), out-of-plane perpendicular to the current direction j (oopj) (b), (e) and out-of-plane perpendicular the transverse direction t (oopt) (c), (f) as shown above.

To obtain the MR amplitudes $\Delta\rho/\rho_0$ the data are fitted by \cos^2 functions (solid lines in Figs. 5.2.4 (a)-(c)). The MR amplitudes are plotted in Fig. 5.2.5 (a) as a function of temperature. A decrease in amplitude is observed for the oopj (red circle) and oopt (purple triangles) measurement geometry with decreasing temperature. This temperature depen-

dence is similar to the temperature dependence of the SMR amplitude [13]. However, the amplitudes are quite different. The amplitude extracted from ADMR measurements in the oopj rotation plane is larger than the amplitude in oopt rotation. The MR amplitude of the ip measurement geometry (black squares) decreases slightly with decreasing temperature, but show a significantly smaller amplitude compared to that of the oopj and oopt measurements.

The ADMR data of the bottom Pt strips reveal a distinct angle-dependence of ρ_{long} in the ip, oopj and oopt measurements. Moreover a phase shift of the angle-dependence of ρ_{long} is observed between 100 K and 200 K as well as between 200 K and 300 K in oopj and oopt measurements, respectively. A similar behavior in oopj measurement geometry has been observed by Geprägs *et. al* [57] for a YIG/Pt//YAG bilayer, which was attributed to the combined action of SMR and AMR caused by a finite intermixing at the YIG/Pt interface. This might result in a complex resistance network of conducting paths, causing a finite AMR visible in oopj and oopt ADMR measurements. The curves are again fitted by \cos^2 functions and the extracted amplitudes $\Delta\rho/\rho_0$ are shown in Fig. 5.2.5 (b). The MR amplitudes of the oopj measurement (red circles) decrease for decreasing temperatures. However below 150 K, after the phase shift occurs, the amplitude increases again. The MR amplitude extracted from the oopt measurement (blue triangles) shows an increase in the amplitude for decreasing temperature. However, caused by the phase shift the amplitude has a minimum around 250 K. The amplitude in the ip rotation shows an increase for decreasing temperature. Comparing this data with the data obtained by the patterned Pt/YIG/Pt/YAG heterostructure discussed in Chapter 4.3.2 shows a rather big discrepancy between the data measured on the short Pt strips and the data obtained for long Pt strips even though they are expected to perform similarly. However the amplitudes in the ip rotation of the bottom Pt strips (Fig. 4.3.9 (b) and Fig. 5.2.5 (b) purple triangles) show the same temperature dependence. Moreover the MR amplitudes in the ip (black squares) and oopj (red circles) rotation planes in Fig. 5.2.5 (a) show a similar temperature dependence compared to Fig. 4.3.10 (a). Thus seeming that both heterostructures perform similar in some respects. Therefore, we take a closer look on the strip design used for the heterostructure with short Pt strips (see Fig. 5.2.6). There the bonding pads are connected to the main strip via connecting Pt strips. These connecting strips have an angle of 45° to the main strip and 90° to each other. Therefore a constant contribution from the connecting strips is expected in the ip rotation plane. However, when rotating the magnetic field in the oopj and oopt rotation planes, there is always a finite contribution to the ADMR from the connection strips. With this in mind, the ADMR data shown in Fig. 5.2.4 can be understood. The angle-dependence of ρ_{long} of the top and bottom Pt strips in the ip measurement geometry only shows a contribution of the main Pt strip since the connecting strips only contribute to ρ_0 . In the oopj and oopt measurement geometry, the Pt connecting strips will lead to an additional angle dependence of ρ_{long} . Therefore, also in the framework of the SMR theory, we expect a finite angle-dependence of ρ_{long} in the oopt-measurement geom-

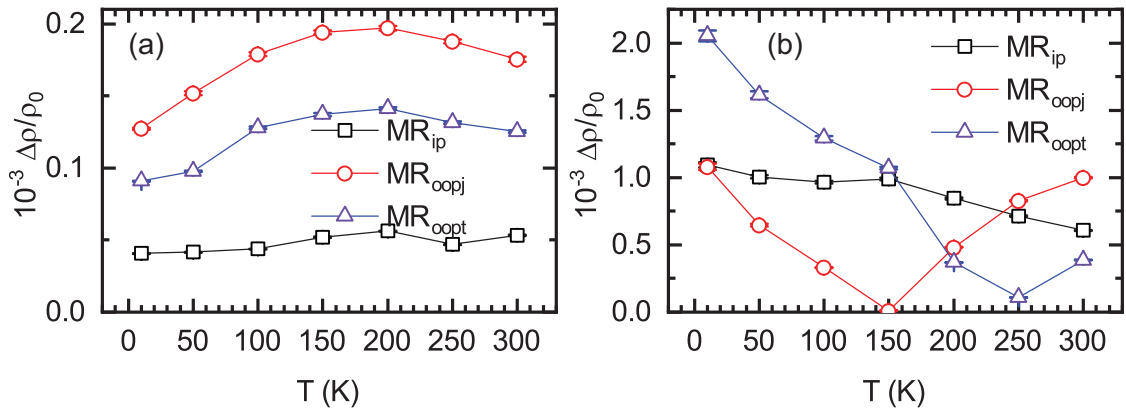


Figure 5.2.5: MR amplitudes extracted from ADMR measurements performed on a $8\ \mu\text{m}$ long (a) top and (b) bottom Pt strip of a patterned Pt/YIG/Pt//YAG heterostructure at $\mu_0 H = 7\ \text{T}$ at different temperatures. The magnetic field is rotated in ip (black squares), oopj (red circles) and oopt (blue triangles) rotation planes. The lines are a guide to the eye.

etry using the design shown in Fig. 5.2.6. This is supported by the MR amplitudes shown in Fig. 5.2.5 (a) since adding the amplitudes of the ip rotation (black squares) to that of the oopt rotation (purple triangles) matches the amplitudes found in the oopj-measurement geometry (red circles). Therefore, the angle-dependence of ρ_{long} of the top Pt layer can be explained solely by the SMR theory. At the bottom Pt layer we expect an SMR as well as AMR signal assuming a finite intermixing between YIG and Pt (compare Fig. 4.3.10 (b)). Therefore a contribution of both effects can be observed in the connecting strip in the oopj as well as oopt rotation plane. Keeping this in mind the temperature dependence of the

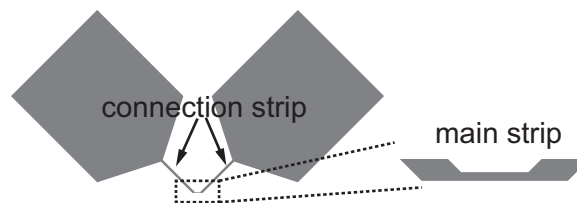


Figure 5.2.6: Design of the Pt strips used for the Pt/YIG/Pt//YAG heterostructure with short Pt strips.

MR amplitude extracted from measurements in oopj- and oopt-geometries as well as the phase shift can be explained. We can attribute the change in phase at approximately 150 K of the ADMR in the oopj measurement (Fig. 5.2.4 (e)) to the AMR contribution from the connecting strip surpassing the magnitude of the SMR amplitude of the connecting strip and the main Pt strip at lower temperatures. The same behavior is seen in the ADMR oopt measurements (Fig. 5.2.4 (f)). There the change in phase at approximately 250 K can be attributed to the SMR contribution from the connecting strips surpassing the AMR effect of the connecting strip and the main strip for higher temperatures.

5.3. Conclusion

In this chapter possibilities for further optimization of the quality of the bottom YIG/Pt interface to minimize the observed AMR and thus interdiffusion into the Pt layer were discussed. The AMR effect could be reduced by introducing a Ru buffer layer between the Pt and YIG layer. However, there is still a finite AMR detectable in the measured temperature range using angle-dependent magnetoresistance measurements. A second Ru buffer layer between Pt and the YAG substrate lead to a non SMR-like temperature dependence of the MR amplitudes, which might be due to an electric shunt by the bottom Ru layer. Therefore a single Ru layer seems favorable. However, unfortunately, the additional Ru layers have no influence on the magnetic properties of YIG at low temperatures. In particular, a large exchange bias is still visible at 10 K. Due to the lack of time, this could not be further investigated in the framework of this thesis.

The issue regarding electrical shorts between the bottom and top Pt strips has been tackled first by increasing the YIG thickness. This results in an increase of the crystalline quality of the YIG layer, but did not increase the resistance between the top and bottom Pt layer. However, by significantly reducing the length of the Pt strips the resistance between the two Pt layer could be significantly increased. This sample therefore is a good candidate for magnon-mediated magnetoresistance measurements in vertical Pt/YIG/Pt structures.

6. Magnon-mediated magnetoresistance measurements

In this chapter the fabricated heterostructures are investigated regarding their magnon-mediated magnetoresistance (MMR) properties. The results are compared to data obtained from a well-established horizontal, two-strip MMR structure of a Pt/YIG bilayer, with the YIG layer fabricated by using the two step rapid annealing process described in Chapter 4.1. The MMR is obtained using in-plane angle-dependent magnetoresistance (ADMR) measurements, where the current is applied in one Pt strip (magnon injector) and the voltage is measured in the second Pt strip (magnon detector).

6.1. Magnon-mediated magnetoresistance measurements on the Pt/YIG/Pt heterostructure with short Pt strips

As the vertical Pt/YIG/Pt heterostructure with short Pt strips has promising electrical properties with high resistance between the top and bottom Pt strip (see Chapter 5.2.2), it is investigated regarding its MMR behaviour. Therefore, first, the temperature dependence of the leakage voltage $V_{\text{top, off}}$ between the top and bottom Pt strip is measured in the top Pt strip, which serves as detector strip for the MMR measurements. Ideally, $V_{\text{top, off}}$ should be 0 V assuming a highly insulating YIG layer. For this a current of 20 μA is applied at the bottom Pt strip while on the top Pt strip the voltage is measured. The temperature is ramped up from 50 K to 300 K at a rate of 5 K min^{-1} . The temperature dependence of $V_{\text{top, off}}$ measured on the 8 μm long and 1 μm wide Pt strip is shown in Fig. 6.1.1. Starting from $V_{\text{top, off}} \approx 1 \mu\text{V}$ at 50 K, the leakage voltage first decreases slightly for increasing temperatures. It reaches its minimum of $V_{\text{top, off}} = 0.5 \mu\text{V}$ at approximately 185 K. Then it increases slightly reaching $V_{\text{top, off}} = 0.8 \mu\text{V}$ at 225 K. Increasing the temperature further significantly increases the offset voltage up to approximately 6 μV at 300 K. Thus, measurements below 250 K seem favorable. For the investigation regarding MMR, in-plane ADMR measurements are performed. Contrary to the investigation of the magnetotransport properties in the previous chapters (see Chapter 4.3.2), the voltage is now measured on the Pt strip, where no current is applied. First a current of $I_{\text{bot}} = 100 \mu\text{A}$ is applied along the bottom Pt strip (injector) using the current reversal technique, while the voltage is measured on the top Pt strip (detector). Due to the high current and therefore a high current density of $2 \times 10^{10} \text{ A m}^{-2}$, heating effects are present. This requires a careful anal-

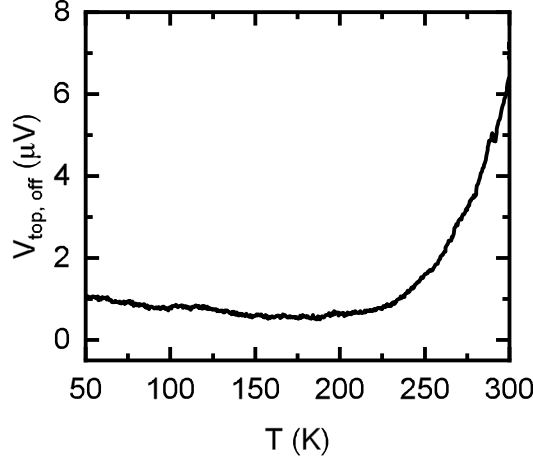


Figure 6.1.1.: Temperature dependent leakage voltage $V_{\text{top,off}}$ measured at the top $8 \mu\text{m}$ long Pt strip, which serves as detector strip for MMR measurements, while applying a current of $20 \mu\text{A}$ to the bottom Pt strip in the Pt/YIG/Pt heterostructure.

ysis of the measured voltages. As shown in Appendix A.2, the current reversal technique allows for voltage extraction odd in current (electrical voltage contribution) and even in current (thermal voltage contribution). The measurement is performed at 100 K, 150 K, 200 K and 250 K. A magnetic field magnitude of $\mu_0 H = 50 \text{ mT}$ is applied and rotated in the film plane (ip). This magnetic field magnitude is large enough to saturate the YIG layer (compare Fig. 4.3.7). In Fig. 6.1.2 the extracted electrical voltage contributions at different temperatures using a $8 \mu\text{m}$ long top Pt strip of a Pt/YIG/Pt heterostructure are shown.

At 100 K (Fig.6.1.2 (a)) the voltage shows no angle-dependence and is very noisy. Similar behavior is observed at 150 K (Fig. 6.1.2 (b)) and at 200 K (Fig. 6.1.2 (c)). At 250 K (Fig. 6.1.2 (d)) a finite angle-dependence is observed between -20° and 150° , but at larger α angles the data are dominated by noise. Moreover the offset voltage is relatively high with $V_{\text{off}} \approx 7.36 \mu\text{V}$ suggesting a finite leakage current across the intermediate YIG layer. For further investigation the detector and injector strip are exchanged. Thus, the current is applied in the top Pt layer, whereas the voltage is measured in the bottom Pt layer. Moreover the applied magnetic field magnitude is increased to $\mu_0 H = 2 \text{ T}$, which reduced the noise level. Furthermore the applied current is increased from $100 \mu\text{A}$ to $300 \mu\text{A}$ and to $500 \mu\text{A}$, which corresponds to a current density of $2 \times 10^{10} \text{ A m}^{-2}$, $6 \times 10^{10} \text{ A m}^{-2}$ and $1 \times 10^{11} \text{ A m}^{-2}$, respectively. The resistivity related voltage contribution of the ADMR data of a $3 \mu\text{m}$ long Pt strip with a width of $w = 2 \mu\text{m}$ at 280 K are shown in Fig. 6.1.3 (a)-(c). When applying $I_{\text{top}} = 100 \mu\text{A}$ at the top Pt strip (see Fig. 6.1.3 (a)) a similar behavior as before in Fig. 6.1.2 (d) is observed. However, the offset voltage $V_{\text{off}} \approx 3.94 \mu\text{V}$ is lower. This can be attributed to the shorter strip length of the here investigated structure. Increasing the current to $I_{\text{top}} = 300 \mu\text{A}$ gives rise to a distinct angle dependence (see Fig. 6.1.3 (b)). To extract the amplitude, the data are fitted by a \cos^2 function. This gives an amplitude of $\Delta V_{\text{bot}} = (11 \pm 1) \text{ nV}$. However, the angle dependence observed here does not fit the expected angle dependence of the MMR (compare Chapter 2.3.2). Comparing this to the

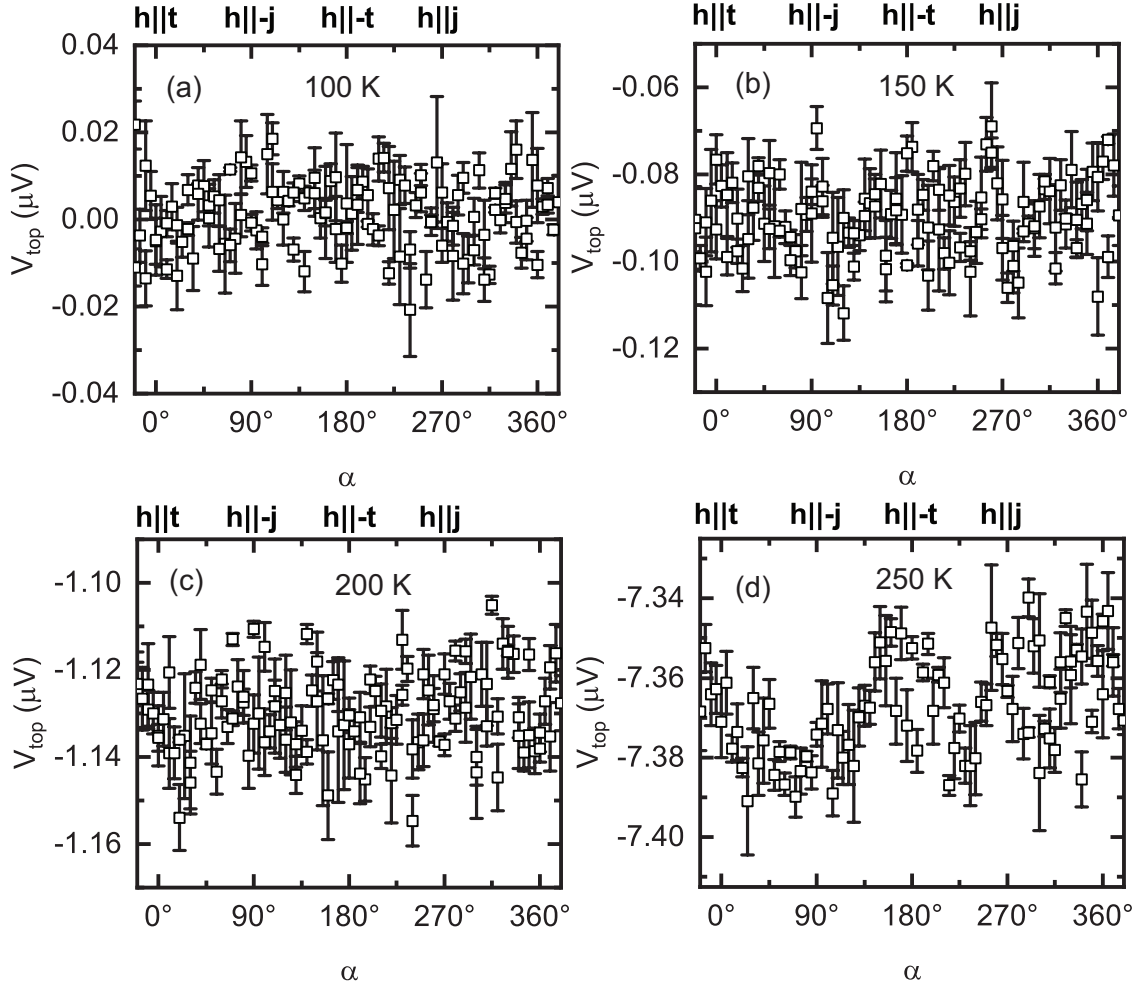


Figure 6.1.2.: Electrical contribution of the measured voltages V_{top} at the top Pt strip (detector) at an applied magnetic field magnitude of 50 mT and an applied current at the bottom Pt strip (detector) of 100 μA . The temperatures at which the measurements are performed are (a) 100 K, (b) 150 K, (c) 200 K, and (d) 250 K, respectively.

observed MR angle dependence of the bottom Pt layer (compare Fig. 5.2.4 (d)) gives rise to the same angle dependence. Moreover the offset voltage significantly increases by one order of magnitude to $V_{\text{off}} \approx 12.36 \mu\text{V}$. Therefore, the finite angle-dependence visible in Fig. 6.1.3 (b) can be attributed to an SMR or AMR signal in the bottom Pt layer arising through a leakage current from the top to the bottom Pt layer. Increasing the current in the top Pt layer further to $I_{\text{top}} = 500 \mu\text{A}$ shows no angle-dependence of the measured voltage in the bottom Pt layer V_{bot} . Moreover the offset voltage increased by almost a factor of 2 to $V_{\text{off}} \approx 22.35 \mu\text{V}$. Due to the high current densities applied to the top Pt layer, we expect Joule heating in the top Pt strip. Fig. 6.1.3 (d) shows the extracted thermal contribution of the measured voltage in the bottom Pt layer $V_{\text{bot, therm}}$. A clear angle-dependence is visible for currents of $I_{\text{top}} = 300 \mu\text{A}$ and $I_{\text{bot}} = 500 \mu\text{A}$ applied at the top Pt strips. At an applied current of $I_{\text{top}} = 100 \mu\text{A}$ a very small modulation is observed. These modulations show the angle dependence expected for the Spin Seebeck effect as discussed in Chapter

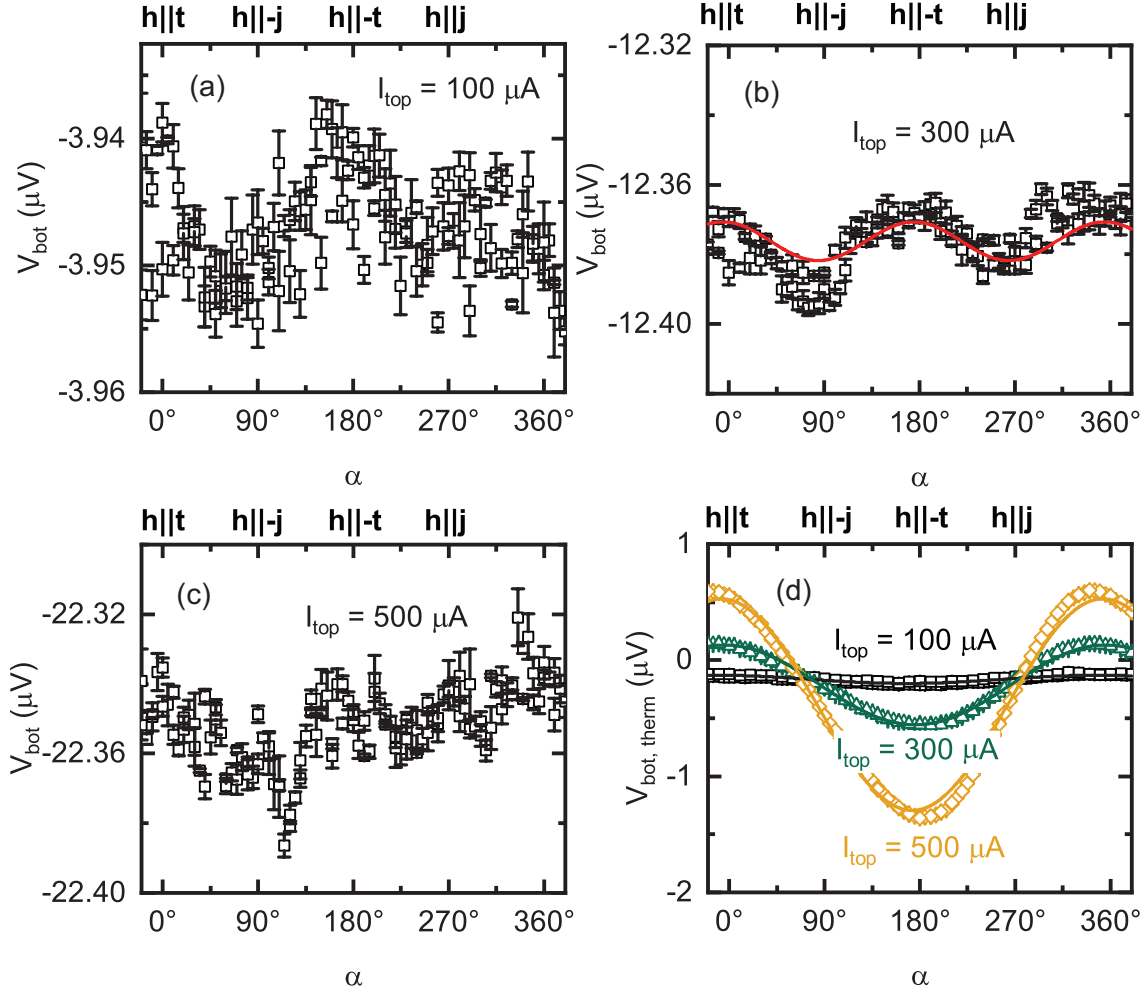


Figure 6.1.3.: Electrical and thermal contribution of the measured voltages at the bottom Pt strip at an applied magnetic field of 50 mT, which is rotated in the film plane (ip). (a)-(c) shows the electrical signal at an applied current at the top Pt strip of (a) 100 μA , (b) 300 μA , and (c) 500 μA . (d) shows the thermal signal measured at the bottom Pt strip with a current of 100 μA (black squares), 300 μA (green triangles) and 500 μA (orange rhombus). The measurements are performed at 280 K.

2.4 and are therefore fitted by \cos functions. From these fittings the amplitudes ΔV_{SSE} are extracted to $\Delta V_{\text{SSE}, 100 \mu\text{A}} = (0.035 \pm 0.001) \mu\text{V}$, $\Delta V_{\text{SSE}, 300 \mu\text{A}} = (0.343 \pm 0.002) \mu\text{V}$ and $\Delta V_{\text{SSE}, 500 \mu\text{A}} = (0.911 \pm 0.006) \mu\text{V}$, respectively. Compared to previously reported values of the SSE amplitude by Ganzhorn *et. al* [46] measured at 300 K in Pt strips separated horizontally by 20 nm the amplitude here is decreased, even when applying a larger current density than in their work. This might be due to a poor interface quality of the bottom Pt strip due to a finite intermixing, as discussed in Chapter 4.3.2. This reduces the spin current transparency and reduces the spin Seebeck voltage. Unfortunately, the Pt strips are destroyed after applying the high current of 500 μA , which prevents measurements of the temperature gradient across the YIG layer to analyse the data in detail. Therefore, further investigation of the SSE of vertical Pt/YIG/Pt heterostructures is needed.

6.2. Magnon-mediated magnetoresistance measurements on Pt/YIG/Ru/Pt heterostructures

Additionally to the Pt/YIG/Pt sample a Pt/YIG/Ru/Pt heterostructure is investigated regarding its MMR properties. The investigated strips have a length of $l_{\text{bot}} = 200 \mu\text{m}$ on the bottom Ru/Pt layer and $l_{\text{top}} = 25 \mu\text{m}$ on the top Pt layer. The width of these strips is $w = 1 \mu\text{m}$. ADMR measurements are performed analogously to Chapter 6.1.

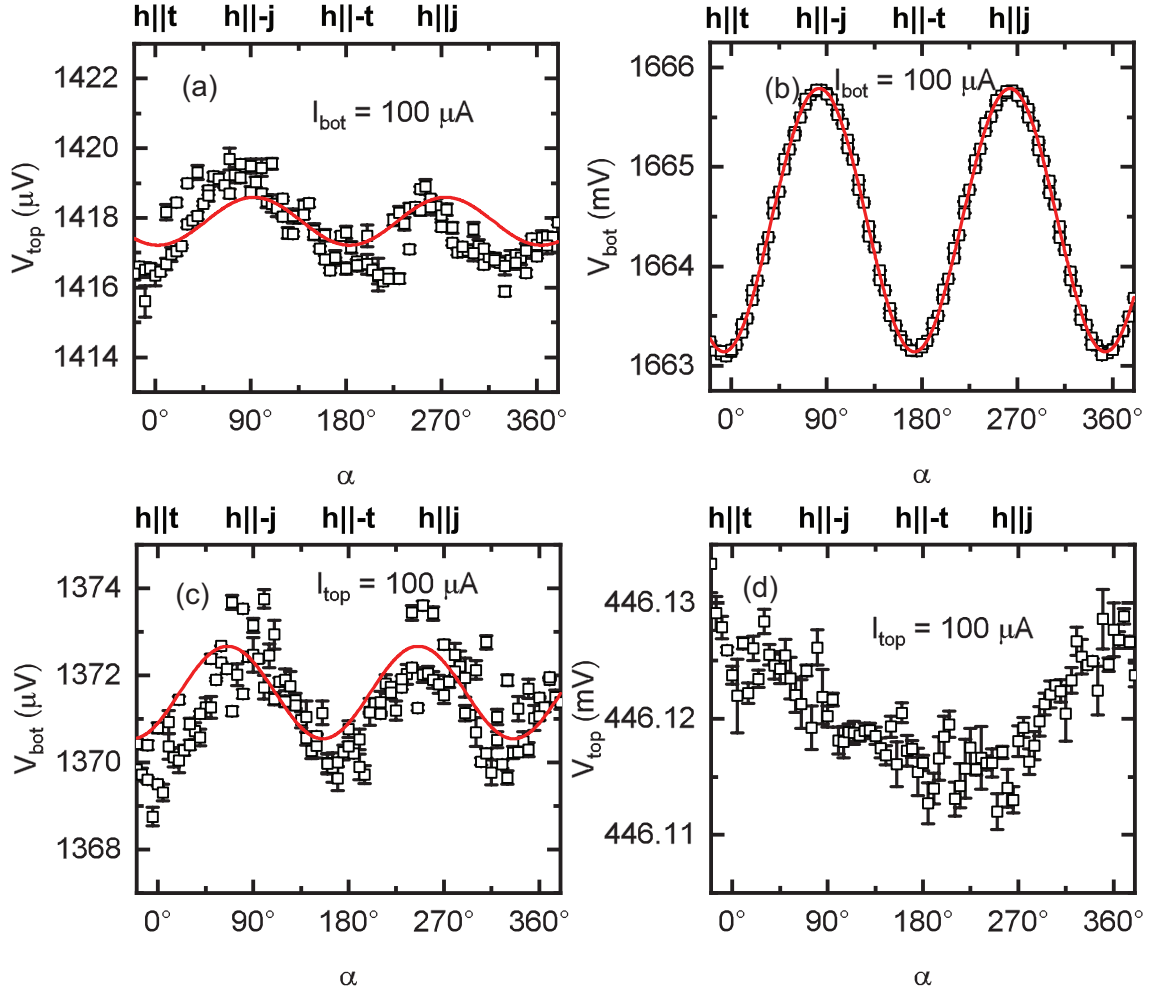


Figure 6.2.1: Electrical contribution of the measured voltages of the top Pt and bottom Ru/Pt strips of a patterned Pt/YIG/Ru/Pt/YAG heterostructure as function of the in-plane magnetic field orientation at 280 K using a magnetic field magnitude of 1 T. The top Pt strip is $25 \mu\text{m}$ long with a width of $1 \mu\text{m}$. The separation between the strips is $t_{\text{YIG}} = (24.3 \pm 0.3) \text{ nm}$. (a) The electrical voltage contribution at the top Pt strip and (b) at the bottom Ru/Pt strip when applying a current of $100 \mu\text{A}$ on the bottom Ru/Pt strip. (c) The electrical voltage contribution at the bottom Ru/Pt strip and (d) at the top Pt strip when applying a current of $100 \mu\text{A}$ on the top Pt strip.

Therefore, a current of $I_{\text{bot}} = 100 \mu\text{A}$ corresponding to a current density of $2 \times 10^{10} \text{ A m}^{-2}$ is applied first on the bottom Pt strip and the voltage V_{top} on the top Pt strip as well as the

voltage V_{bot} on the bottom Pt strip are measured. Here a magnetic field magnitude of $\mu_0 H = 1$ T is applied and rotated in the film plane (ip). The electrical contribution of the measured voltage on the top Pt strip and bottom Ru/Pt strip is shown in Fig. 6.2.1 (a) and Fig. 6.2.1 (b), respectively. The same angle-dependence is observed in both Pt strips. However, a phase shift of 90° compared to the local voltage signal is expected for the MMR (see Chapter 2.3.1 and Chapter 2.3.2). Moreover, the offset voltage $V_{\text{top, off}} = 1.42$ mV is very high, indicating a large leakage current across the YIG layer. Both datasets are fitted by \cos^2 functions and the amplitudes ΔV_{bot} and ΔV_{top} are extracted. Comparing the normalized amplitude $\Delta V_{\text{top}}/V_{\text{top, } H\parallel t} = (9 \pm 3) \times 10^{-4}$ to the MR amplitude obtained for the ip rotation of the top Pt layer (see Fig. 4.3.10 (a)) reveals a slightly increased but still similar amplitude. This further indicates that the observed angle-dependence is due to a leakage current from the bottom to the top Pt strip. Thus, the measured angle-dependence might be attributed to the SMR or AMR in the top Pt strip.

The same measurement is performed again, but the current is now applied to the top Pt strip and the voltage is measured on the top (V_{top}) and on the bottom (V_{bot}) Pt strip. In Fig. 6.2.1 (c) the electrical contribution of the measured voltage at the bot Pt strip is shown. This reveals the same angle dependence as before and therefore, again, does not match the expected MMR signature (compare Chapter 2.3.2). Moreover, the offset voltage $V_{\text{off}} \approx 1.37$ mV is again very large. The normalized amplitude gives $\Delta V_{\text{bot}}/V_{\text{bot, } H\parallel t} = (9.6 \pm 5) \times 10^{-4}$. The value is very similar to the MR amplitude extracted from ip rotation of the bottom Ru/Pt layer (see Fig. 5.1.4). Additionally, it is nearly equal to the amplitude of the ADMR measurements on the top Pt strip when applying a current at the bottom Pt strip. Interestingly, the electrical voltage contribution measured on the top Pt strip (see Fig. 6.2.1 (d)) shows an angle dependence that cannot be described within the theory of SMR nor AMR (compare Chapter 2.3.1 and Chapter 2.3.3). The \cos -like angle-dependence might be due to a finite tilting of the sample with respect to the rotation plane of the magnetic field, but needs to be investigated in the future. However, the ADMR measurements in the Pt/YIG/Ru/Pt heterostructure is dominated by leakage currents across the YIG layer and no clear MMR signal could be found.

6.3. Magnon-mediated magnetoresistance measurements on a Pt/YIG bilayer

In order to get a better understanding of the encountered issues from MMR measurements on Pt/YIG/Pt trilayers the MMR properties of a Pt/YIG//YAG bilayer with conventional, horizontal Pt-strips is investigated. The YIG layer is fabricated via the two-step annealing process using the same parameters as for the Pt/YIG/Pt//YAG heterostructure discussed in Chapter 4.3.2. For the Pt layer the well established horizontal two strip design is used [17, 21] and is fabricated by lift-off technique after performing electron beam lithography (see Appendix A.4.3). In this design one strip serves as magnon injector and the other

horizontally separated Pt-strip as magnon detector. For a more detailed description see Chapter 2.3.2.

The magnetic field is rotated in the film plane using a magnetic field magnitude of 50 mT. The strips have a length of 15 μm , a width of 100 nm and are separated by 300 nm. The applied current in the injector strip is $I_{\text{inj}} = 100 \mu\text{A}$, 300 μA and 500 μA corresponding to a current density of $2 \times 10^{11} \text{ A m}^{-2}$, $6 \times 10^{11} \text{ A m}^{-2}$ and $1 \times 10^{12} \text{ A m}^{-2}$, respectively. Fig. 6.3.1 (a)

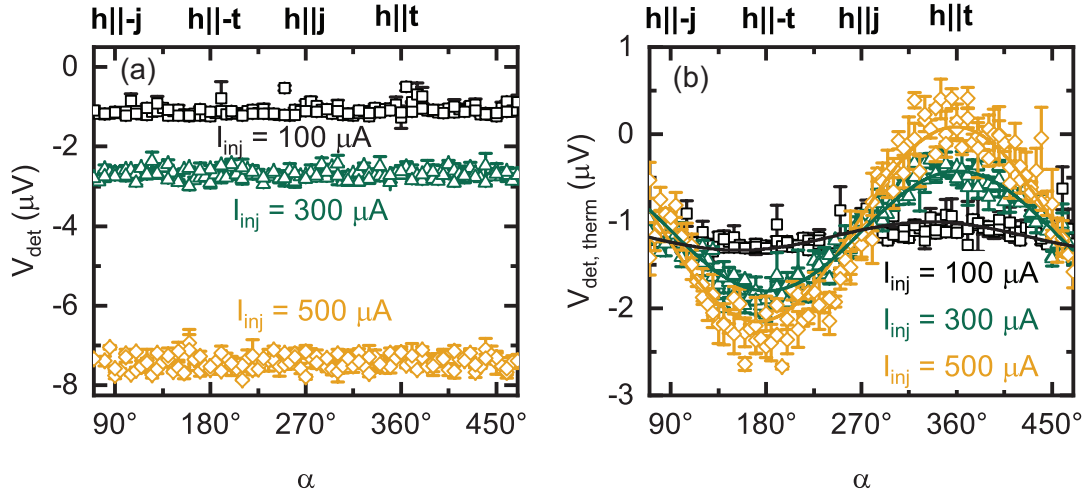


Figure 6.3.1: In-plane ADMR measurements on a Pt/YIG bilayer using a horizontal, two Pt strip design with a current of 100 μA (black squares), 300 μA (green triangles) and 500 μA (orange rhombus) applied at the injector Pt strip. The measurements are performed at 280 K and with an applied magnetic field magnitude of $\mu_0 H = 50 \text{ mT}$. The strips are 100 nm wide and separated by 300 nm. (a) Resistive and (b) thermal voltage contribution of the measured voltage at the Pt detector strip.

shows the electrical contribution of the measured voltage of the detector strip V_{det} obtained by in-plane ADMR measurements. Over the whole used current range there is no angle dependence observable. Moreover, the noise level is rather high and increases for higher applied currents together with the offset voltage. Thus, no MMR could be measured in this sample. This might be due to a poor interface quality between Pt and YIG although the local voltage measurements reveal a SMR-like behavior. Fig. 6.2.1 (b) shows the thermal contribution $V_{\text{det,therm}}$ of the measured voltage on the detector strip from the in-plane ADMR measurements. There an angle-dependence is visible for all applied currents. However, the thermal voltage V_{therm} shows an offset voltage of around 1 μV , which might be due to a finite leakage current between the Pt strips. The observed angle-dependence is in agreement with the SSE (see Chapter 2.4) and is fitted with cos functions. From these fits, an amplitude of $\Delta V_{\text{therm}, 100 \mu\text{A}} = (0.37 \pm 0.06) \mu\text{V}$ at $I_{\text{inj}} = 100 \mu\text{A}$, $\Delta V_{\text{therm}, 300 \mu\text{A}} = (0.68 \pm 0.01) \mu\text{V}$ at $I_{\text{inj}} = 300 \mu\text{A}$ and $\Delta V_{\text{therm}, 500 \mu\text{A}} = (1.11 \pm 0.02) \mu\text{V}$ at $I_{\text{inj}} = 500 \mu\text{A}$, respectively, are extracted. The increase in amplitude for increasing applied currents in the injector strip is expected due to an increased Joule heating and therefore larger temperature gradients in the YIG thin film. Compared to the vertical Pt/YIG/Pt heterostructure with short Pt

strips (compare Fig. 6.1.3 (d)), the here extracted amplitudes are larger, but with higher applied current densities. This is expected due to the increased distance of 300 nm of the Pt strips. Compared to other SSE measurements on such two strip structures the determined amplitude ΔV_{SSE} is similar [46]. However, here, a higher current density is applied in the injector strip, leading to an increased Joule heating and therefore a larger temperature gradient. Moreover, when applying a similar current density in the injector strip as in the work by Ganzhorn *et. al* [46] no angle-dependence and therefore no SSE signal could be detected. Thus, this further indicates that the interface of the YIG to the top Pt might be of worse quality than expected from Chapter 4.3.2.

6.4. Conclusion

In summary, we are not able to measure a clear magnon-mediated magnetoresistance (MMR) in the patterned vertical Pt/YIG/Pt heterostructures within the framework of this thesis. The electric measurements are highly influenced by a leakage current across the YIG layer. Additionally, we could not find a clear MMR signal in a Pt/YIG bilayer using a well established, horizontal two strip design. However, we are able to measure an SSE in the vertical patterned Pt/YIG/Pt heterostructures as well as in the horizontal two strip design of the Pt/YIG bilayers. The amplitudes of the SSE are comparable to previous works, but higher current densities are necessary. Unfortunately, the Pt-strips are broken after applying the high current densities, which prevents a detailed SSE characterization of the devices. These findings together indicate that the resistance of the YIG layer as well as the Pt/YIG interfaces need to be further optimized although Chapter 5 showed promising results.

7. Summary and outlook

In this chapter a brief summary over the results of this thesis as well as an outlook for further research is given.

7.1. Summary

In this work we have optimized the fabrication of patterned, vertical Pt/YIG/Pt heterostructures on garnet substrates for magnon-mediated magnetoresistance measurements. To this end, first, the optical lithography process on transparent substrates using the laser writing system PicoMaster 200 has been implemented. Moreover, second, a lift-off technique together with thin films deposited by PLD at room temperature with subsequent annealing has been developed. This provides a high flexibility for the fabrication of future devices. However, the main task within the framework of this thesis is the fabrication of Pt/YIG/Pt heterostructures with excellent quality of the Pt/YIG interfaces regarding spin current transparency. This has been proven to be a challenging task [57, 58, 62, 63].

By starting from the Bachelor thesis by C. Mang [62], a first Pt/YIG/Pt trilayer was fabricated in-situ and patterned afterwards by optical lithography and Ar-ion milling. However, no electrical conductivity could be measured on the few μm -wide Pt strips. Furthermore, the YIG layer was amorphous. Therefore, several optimization steps were carried out resulting in Pt/YIG/Pt heterostructures with a high conductivity of the Pt layers as well as a crystalline YIG layer. In particular, the direct contact between the garnet substrate and the YIG thin film, led to high-crystalline YIG layers after a two step annealing process. Additionally, the used garnet substrate was changed from $\text{Gd}_3\text{Ga}_5\text{O}_{12}$ (GGG) to $\text{Y}_3\text{Al}_5\text{O}_{12}$ (YAG) which enables lower temperatures during the annealing process and therefore a better electrical conductivity of the Pt strips. These heterostructures exhibit good structural properties of the YIG layer although of the lattice mismatch of 3% between YIG and YAG. Moreover, a smooth surface with formation of few small grains has been revealed by AFM. The magnetic hysteresis loops at 300 K of the patterned vertical Pt/YIG/Pt//YAG heterostructures yield similar values of the saturation magnetization as well as coercive fields as previously reported. However, a by one order of magnitude larger exchange bias at 10 K, than previously reported for YIG thin films deposited on a YAG substrate was observed. Moreover, angle-dependent magnetoresistance (ADMR) measurements were performed to investigate the quality of the Pt/YIG interfaces. While the data suggest a good interface quality of the top Pt/YIG interface, the bottom Pt/YIG interface show indication a finite intermixing of the YIG and bottom Pt layer. Thus, a

1 nm thick Ru buffer layer was introduced between the YIG and the bottom Pt layer. With this Ru buffer layer a clear improvement of the YIG/Pt interface could be achieved. However, a reduction of the crystalline quality of the YIG layer, but an increase of the saturation magnetization as well as the width of the hysteresis loop at low temperatures could be observed. For a potential further improvement, a second Ru buffer layer was introduced between the Pt and the YAG substrate to prevent oxygen and aluminium diffusion from the substrate into the Pt thin film. The structural properties of the YIG layer improved compared to a single Ru buffer layer, but were still worse than for a respective Pt/YIG/Pt//YAG sample. The saturation magnetization was found to be decreased at low temperatures but no change of the width of the hysteresis as well as the observed exchange bias could be found. Moreover magnetotransport measurements revealed that the second Ru buffer layer led to a rather different temperature dependence than observed before and also expected from the temperature dependence of the spin Hall magnetoresistance. This was attributed to an electrical shunt by the bottom Ru layer.

Additionally to intermixing effects at the bottom YIG/Pt interface, electrical shorts between the bottom and top Pt strips have been observed. To solve this issue, we first doubled the YIG layer thickness, which resulted in a better crystalline quality of the YIG layer but did not solve the underlying issue. Second, we decreased the length of the Pt strips and thus the lateral, overlapping area between Pt and YIG. In this Pt/YIG/Pt heterostructure, a high resistance between the top and bottom Pt strips could be measured, which enables further investigation with respect to the magnon-mediated magnetoresistance (MMR) effect in these vertical heterostructures.

Further angle-dependent magnetotransport measurements on the patterned, vertical Pt/YIG/Pt as well as the Pt/YIG/Ru/Pt heterostructures using the bottom and top Pt strips as magnon injector and detector, respectively, showed no sign of a finite MMR effect. To further investigate the absence of the MMR in the Pt/YIG/Pt trilayer, a Pt/YIG//YAG bilayer was fabricated using the two step rapid annealing process for crystallization of the YIG layer. A well established horizontal, two Pt-strip design was patterned on top of the YIG layer by sputtering on this bilayer as well. Unfortunately, no MMR signal could be found on this bilayer as well. However, the vertical Pt/YIG/Pt heterostructure as well as the Pt/YIG bilayer with the horizontal Pt-strip design showed a finite spin Seebeck effect (SSE) due to current heating. The SSE amplitude was smaller than previously reported values at similar current densities measured on Pt/YIG bilayers with horizontal Pt-strip designs. This can be attributed to a smaller spin current transparency at the Pt/YIG interfaces. Therefore, these interfaces might have a worse quality than expected.

7.2. Outlook

As demonstrated in this thesis, the MMR measurements of the vertical Pt/YIG/Pt heterostructures are highly dominated by leakage currents across the YIG layer. Therefore, also MMR transport measurements were performed at lower temperatures. In the Pt/YIG/Ru/Pt/Ru heterostructure, indeed, a sign of a finite MMR could be observed using angle-dependent (ADMR) measurements. The ADMR measurement was performed at 100 K with an applied current of $I_{\text{bot}} = 100 \mu\text{A}$ at the bottom Ru/Pt/Ru trilayer using a magnetic field magnitude of $\mu_0 H = 2 \text{ T}$. The electrical voltage contribution of the measured voltage in the top Pt strip is shown in Fig. 7.2.1. A clear \cos^2 angle-dependence

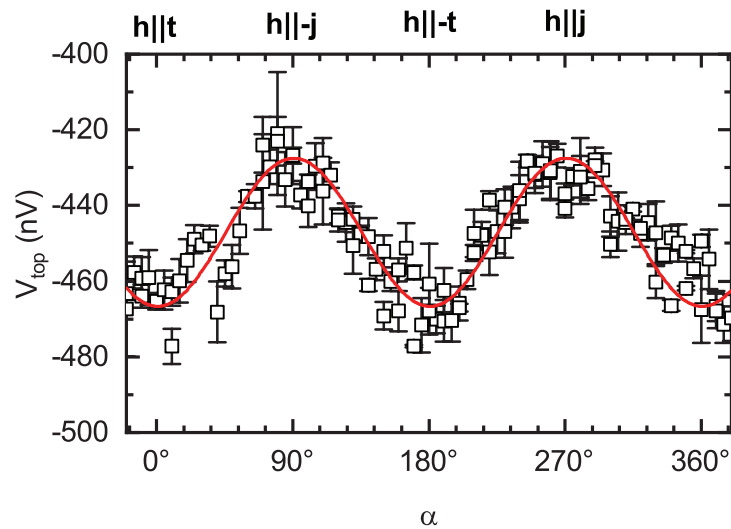


Figure 7.2.1: Electrical contribution of the voltage measured in the top Pt layer of a patterned Pt/YIG/Ru/Pt/Ru heterostructure at 100 K. The current $I_{\text{bot}} = 100 \mu\text{A}$ is applied in the bottom Ru/Pt/Ru layer stack. The magnetic field magnitude of $\mu_0 H = 2 \text{ T}$ is rotated in the film plane.

is observed and fits the in Chapter 2.3.2 described angle-dependence for a MMR effect. Moreover, the offset voltage is relatively small, suggesting a small leakage current across the YIG layer. This indicates that, indeed, a finite MMR can be observed in the vertical heterostructures fabricated in this work. However, further investigations, e.g. magnetic field and temperature dependent measurements as well as magnetic field rotations in the oopj and oopt planes, are necessary to fully confirm the MMR effect. Additionally, the interface quality of the bottom YIG/Pt layer has to be further improved by increasing the thickness of the Ru buffer layer introduced in Chapter 5.1.1. This might further reduce the intermixing between the YIG and the bottom Pt layer. Furthermore, a surface treatment by e.g. dipping the sample in Piranha solution shortly before the deposition of the top Pt layer might increase the quality of the top Pt/YIG interface. Moreover, due to the observed leakage currents across the YIG layer the electrical properties of the YIG layers need to be further investigated. For better electrical properties, a higher oxygen partial pressure in the process gas during the PLD and/or annealing process might decrease oxygen vacancies in

the YIG thin film, which were found to be closely intertwined with the electrical properties of the YIG thin films [77]. By solving these issues, the vertical Pt/YIG/Pt sample geometry might lead to a miniaturization of currently used horizontal, three Pt-strip devices and may lead to further insight to the spin transport in a magnetic insulator with zero effective damping [21, 24]. Moreover, this vertical geometry allows overall for more complex structure designs and a higher degree of manipulation of the spin transport in magnetic insulators.

Additionally to the electrical issues found in the Pt/YIG/Pt heterostructures a large exchange bias has been observed in the measurements of the magnetization hysteresis of these samples at 10 K, which needs further investigations. Therefore, a heterostructure fabricated with the same parameters, but on different substrates could be investigated to re-evaluate how large the influence of a finite intermixing between the YIG layer and the YAG substrate actually is. Moreover, the area covered with Pt, Ru/Pt and Ru/Pt/Ru could be varied in order to determine the influence these layers have on the magnetic properties of YIG at low temperatures. Additionally, local measurements of the magnetic properties of the YIG layer might be beneficial to determine and possibly improve the quality of the YIG thin film in between the bottom and top Pt layers.

The finite observed SSE in the vertical Pt/YIG/Pt heterostructure (c.f. Chapter 6.1) enables further research in particular on the dependence of the SSE on the YIG thickness. Furthermore, as the Pt layer is only used as a heater in SSE experiments, a material which has the same crystalline structure and therefore a smaller lattice mismatch to YIG would be more appropriate for SSE measurements.

Moreover, the in this work developed lift-off technique together with pulsed-laser deposition enables freestanding high-crystalline, complex oxide materials such as YIG. This might provide the opportunity to transfer them to arbitrary substrates and integrate them into Si-based electrical devices.

A. Appendix

This appendix explains some details of the used deposition techniques, the measurement setups, the analysis methods and gives a list of all samples fabricated in the course of this work.

A.1. List of samples

sample ID	layer sequence	performed measurements
YIG 322	Pt/YIG/Pt//GGG	XRD
YIG 325	Pt/YIG/Pt//GGG	
YIG 326	Pt/YIG/Pt//GGG	
YIG 327	Pt/YIG/Pt//GGG	
YIG 328	Pt/YIG/Pt//GGG	XRD
YIG 329	Pt/YIG/Pt//GGG	XRD
YIG 330	Pt/YIG/Pt//GGG	XRD
YIG 331	Pt/YIG/Pt//GGG	XRD
YIG 332	Pt/YIG/Pt//YAG	XRD
YIG 333	Pt/YIG/Pt//YAG	XRD
YIG 334	Pt/YIG/Pt//YAG	XRD, SQUID
YIG 335	Pt/YIG/Pt//YAG	XRD, SQUID, ADMR, AFM
YIG 339	Pt/YIG/Pt//YAG	XRD, SQUID, ADMR
YIG 340	Pt/YIG/Pt//YAG	XRD, SQUID, ADMR
YIG 345	Pt/YIG/Pt//YAG	XRD, ADMR
YIG 347	Pt/YIG/Ru/Pt//YAG	XRD, ADMR
YIG 348	Pt/YIG//YAG	XRD, SQUID, ADMR, FMR
YIG 349	Pt/YIG/Ru/Pt//YAG	XRD
YIG 350	YIG//YAG	XRD, SQUID, FMR
YIG 351	YIG//YAG	XRD
YIG 352	Pt/YIG/Ru/Pt//YAG	XRD, SQUID, ADMR
YIG 353	YIG//YAG	XRD, SQUID, FMR
YIG 358	Pt/YIG/Ru/Pt/Ru//YAG	XRD
YIG 359	Pt/YIG/Ru/Pt/Ru//YAG	XRD, SQUID, ADMR, AFM

Table A.1.1.: List of all YIG samples fabricated in the framework of this thesis. The horizontal lines indicate the change of the deposition technique of the Pt layers from EVAP to sputtering depositions. The first line indicates the change for the top Pt layer and the second one for to the bottom Pt layer. For all samples, substrates with crystallographic (001)-orientation are used. The right column shows the measurements performed for each sample. XRD corresponds to XRD and XRR measurements, SQUID stands for magnetization hysteresis measurements.

sample ID	layer sequence	crystallographic orientation	GdIG thickness
GdIG 1	Pt/GdIG//GGG	(001)	65.4 nm
GdIG 2	Pt/GdIG//GGG	(001)	44.3 nm
GdIG 3	Pt/GdIG//GGG	(001)	88.3 nm
GdIG 4*	Pt/GdIG//GGG	(011)	58.8 nm
GdIG 5	GdIG/YIG//GGG	(001)	8.02 nm
GdIG 6	Pt/GdIG//GGG	(011)	82.2 nm
GdIG 7	Pt/GdIG//GGG	(111)	24.4 nm
GdIG 8	Pt/GdIG//GGG	(111)	-
GdIG 9*	Pt/GdIG//GGG	(001)	76.3 nm
GdIG 10*	Pt/GdIG//GGG	(111)	72.9 nm

Table A.1.2.: Fabricated GdIG samples for nano-scattering measurements at the ID01 beam-line of the European Synchrotron Radiation Facility (ESRF). Three samples were shipped to the ESRF (indicated by *). The others served as test samples for the Ar-ion milling process as well as optical lithography. The Pt layer is deposited via sputtering.

A.2. Current reversal method

In the ADMR measurements a positive ($+I$) and negative ($-I$) current is alternately applied and the corresponding voltage is measured for each. This allows for extraction of the electrical V_{el} and thermal V_{therm} voltage contributions, since the electrical voltage contribution switches sign under current reversal whereas the thermal contribution does not change the sign. Thus the contributions can be calculated by

$$V_{\text{el}} = \frac{V^+ - V^-}{2} \quad (\text{A.1})$$

$$V_{\text{therm}} = \frac{V^+ + V^-}{2}. \quad (\text{A.2})$$

A.3. Deposition techniques

In this section the used deposition techniques, namely the pulsed laser deposition, electron beam evaporation and dc magnetron sputtering are briefly discussed.

A.3.1. Pulsed laser deposition (PLD)

During the pulsed laser deposition (PLD) a polycrystalline target (YIG) ablated by short laser pulses with a wavelength of $\lambda = 248$ nm and a frequency of $f = 10$ Hz. Moreover the number of pulses is divided into multiple smaller packages of 250 pulses per package. In between those packages the laser is turned off for $t_r = 10$ s, which gives the particles time to relax on the sample surface as well as prevents excessive heating of the target. This ionizes a small part of the target and a plasma plume is created. A part of the ionized material diffuses to the substrate and is deposited on the substrate. The energy density used for the laser is $\rho = 2$ J cm $^{-2}$. The sample can be heated by an infrared heating laser, which

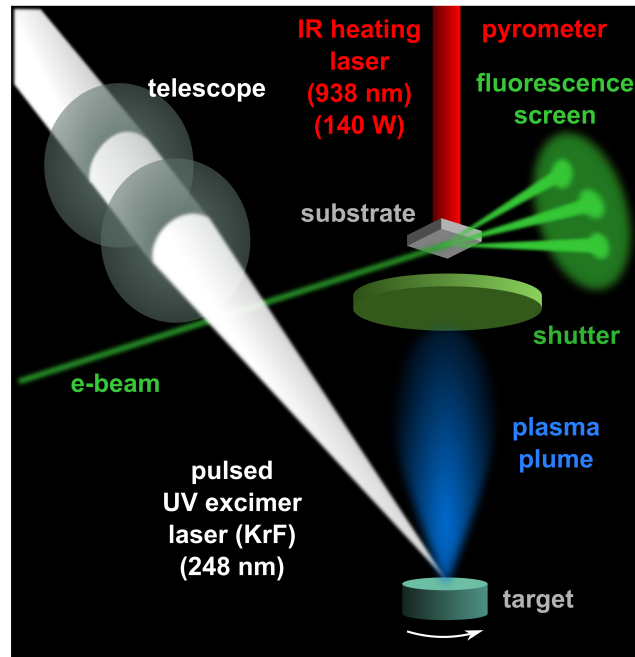


Figure A.3.1.: Schematic functioning principle of the pulsed laser deposition. The pulsed UV KrF laser is focused on the rotating target. The resulting plasma plume reaches the substrate that can be heated by an infrared heating laser. Figure taken from Ref. [63].

was used for the two step rapid annealing process discussed in Chapter 4.1. Therefore, the back of the substrate is covered with 180 nm platinum to ensure a better absorption of the infrared light from the heating laser. Before the actual deposition process the target is ablated for a total of 2000 pulses. This removes some possibly non-stoichiometric layers on the top of the target to ensure a clean deposition material. During this the sample is protected from unwanted deposition with a shutter.

A.3.2. Electron beam evaporation (EVAP)

During the electron beam evaporation of platinum the Pt-target is heated and evaporated by an electron beam, which originates from a filament and is accelerated by $U = 7.5 \text{ kV}$. The beam is focused on the target by magnetic fields. The emission current of the electron beam is $A \approx 135 \text{ mA}$. The deposition rate of the Pt is set to 0.4 \AA s^{-1} and controlled via an oscillating crystal in the EVAP chamber. In the chamber there is a pressure of $p \approx 5 \times 10^{-7} \text{ mbar}$ during the evaporation process.

A.3.3. Magnetron sputtering

Additional to electron beam evaporation Pt films were deposited using magnetron sputtering in the SUPERBOWL ultra high vacuum (UHV) system in the framework of this thesis. The principle of sputtering is that charged ions are accelerated towards the target material. This leads to collisions with the target. The first collision leads to more collisions inside

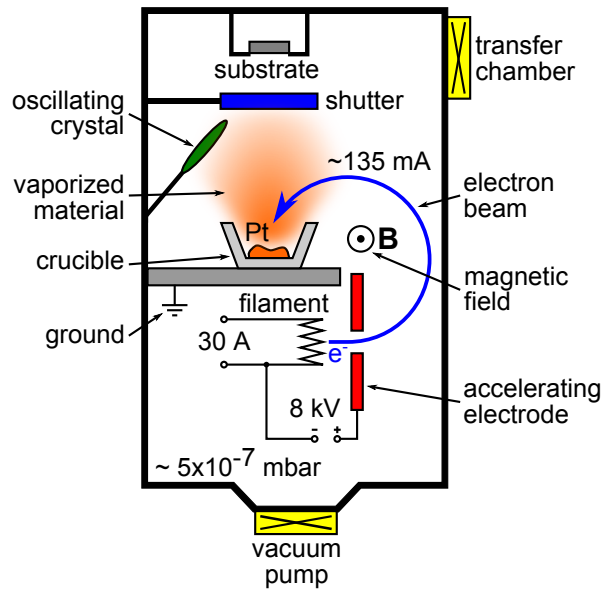


Figure A.3.2.: Schematic of the EVAP chamber. The filament emits an electron beam, that is focused on the Pt target via magnetic fields. This vaporizes the Pt and deposits it on the sample. To control the thickness of the deposited material as well as the deposition rate, an oscillating crystal is used. Figure taken from Ref. [63].

the target resulting in a collision cascade. The collisions lead to secondary electrons and surface atoms, which eventually leave the target. The atoms can then diffuse to the sample placed above the target. In Fig. A.3.3 (a) a schematic of this process is shown. There are several ways to realize such a sputtering process like ion-beam sputtering and reactive sputtering. However, in this work only dc-magnetron sputtering is used. Therefore, we will restrict the discussion to this method. In Fig. A.3.3 (b) a schematic of the magnetron is shown. In the magnetron sputtering technique a magnetic field traps electrons in a helical motion. This greatly increases the distance they need to cover before reaching the anode. On their way they scatter with gas atoms, which ionizes them and creates a plasma. These ions are accelerated to the target and the aforementioned process will take place.

A.4. Analysis methods

In this section, the used analysis methods are explained as well as further details on the measurements are given.

A.4.1. X-ray diffraction

The structural properties of the thin films in this thesis were investigated by using a 4-circle x-ray diffractometer D8 Discover from Bruker. As an x-ray source a copper (Cu) x-ray tube is used with an applied voltage of 40 kV and a current of 40 mA. A Göbel mirror and a 4-bounce Ge-channel cut monochromator are used to achieve monochromatic light with a wavelength of $\lambda = 0.15406$ nm as well as a high intensity. The intensity of the scattered x-

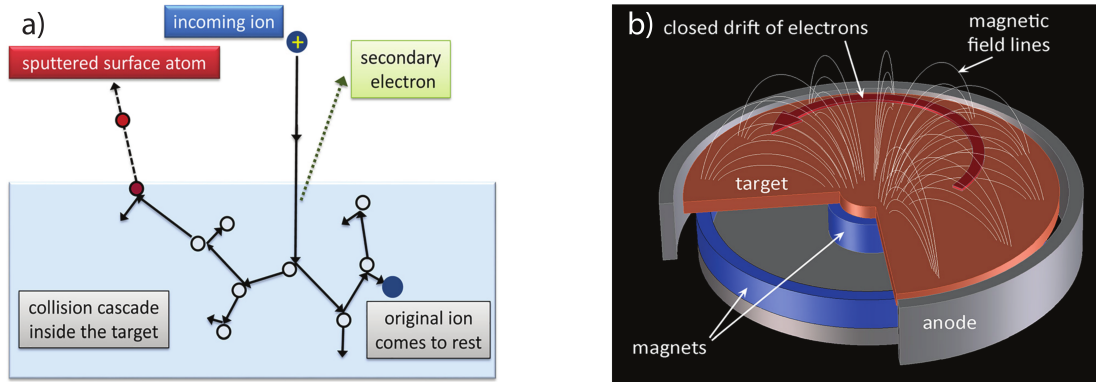


Figure A.3.3.: (a) Illustration of the collision cascade in the sputter target produced by collisions from incident ions. This cascade produces secondary electrons as well as sputtered surface atoms. Figure taken from Ref. [49].

rays is measured by a detector with an angular resolution of 0.001° . The sample is held by a vacuum chuck and can be rotated in all spatial directions (ω , χ and ϕ). ω corresponds to the angle between the sample surface and the incoming x-rays, ϕ is the angle of the in-plane rotation and χ the out of plane rotation. Another important angle for the measurements is 2θ which is the angle between the incoming and reflected x-rays and can be calculated by $2\theta = 2\omega + \alpha$. The angle α takes into account a finite tilting of the lattice planes with

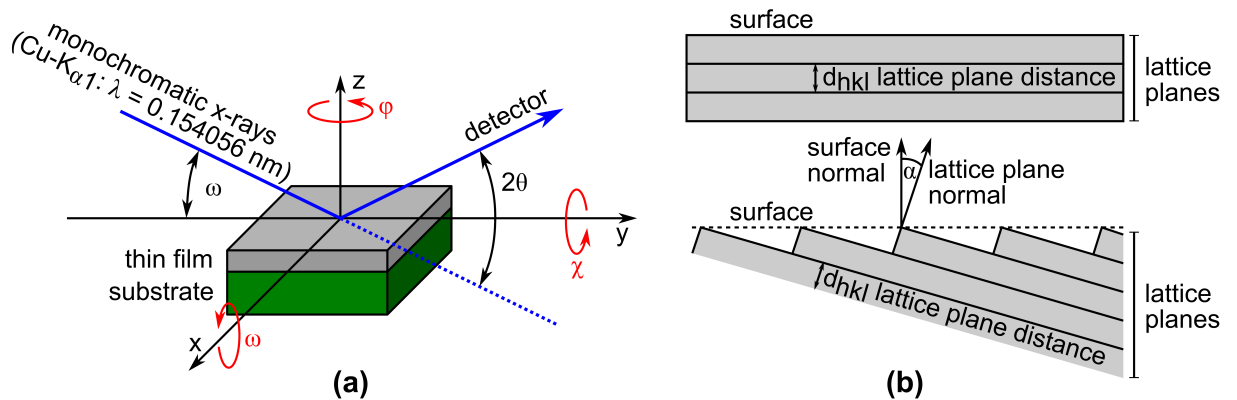


Figure A.4.1.: (a) Monochromatic x-rays from the $\text{Cu-K}_{\alpha 1}$ hit the substrate at an angle ω with respect to the x - y plane. The diffracted intensity is collected with a scintillation detector at an angle 2θ with respect to the incident beam. The sample can be turned in all directions as well as moved in x , y and z direction. (b) Finite tilting α of the lattice planes in real crystals. Figure taken from Ref. [63].

respect to the sample surface. The angles ω at which constructive interference is achieved are given by the Bragg equation [78]

$$2d_{hkl} \sin(\omega) = \lambda \quad (\text{A.3})$$

with the lattice plane distance d_{hkl} , where h , k and l denote the Miller indices. Equivalent to this is the Laue condition [78]

$$\mathbf{k}' - \mathbf{k} = \Delta\mathbf{k} = \mathbf{G} \quad (\text{A.4})$$

where \mathbf{G} is the reciprocal lattice vector and $\Delta\mathbf{k}$ denotes the scattering vector with \mathbf{k}' the scattered beam and \mathbf{k} the incident beam. In this thesis 3 different measurements are performed, namely x-ray diffraction (XRD), rocking curve measurements around a specific reflection and x-ray reflectometry (XRR). Before those measurements an alignment is performed in order to align the x-ray beam with respect to the sample.

For the XRD measurement and rocking curve an additional alignment on the lattice planes is carried out to account for a finite tilt α as well as an out-of-plane tilt by χ . For the 2θ - ω scans (XRD measurements), the x-ray beam is reflected from the sample surface and the 2θ angle is changed in between a range of 10° to 130° . This measurement allows for investigation of the crystalline quality of the respective thin film growth, impurity phases and the determination of the lattice plane distance d_{hkl} . Moreover, from the 2θ -angle of the crystal reflection and d_{hkl} the lattice constant can be calculated with

$$d_{hkl} = \frac{a}{\sqrt{h^2 + k^2 + l^2}} \quad (\text{A.5})$$

assuming a cubic lattice symmetry. Next to reflections of the thin film, finite thickness fringes might be visible. These fringes are called Laue oscillations and indicate a thin film with high crystalline quality and coherent growth of the lattice planes, since the intensity of these are highly dependent on the roughness of the lattice planes.

The rocking curve is a tool to measure the crystalline quality of thin films. In this measurement the 2θ -angle of the detector is fixed to the crystal reflection and ω is varied from $2\theta/2 - 1^\circ$ to $2\theta/2 + 1^\circ$. The crystalline quality can be extracted by the full width at half maximum (FWHM) of the measured peak. Therefore, the narrower the peak, the better the crystalline quality since a broader peak indicates a mosaic spread of the lattice planes.

The XRR measurement is in principle the same measurement as the XRD measurement with the main difference being the range of the 2θ angle. In the reflectometry the 2θ -angle is only varied between 0.5° and 5° . Thus, the x-ray beam is reflected from the interfaces with different refractive indices of the sample rather than the crystallographic planes as in the XRD measurement. The reflections of the interfaces interfere with each other and the resulting intensity profile shows so called Kiessig fringes. The period of these fringes depends on the thickness of the layers, whereas the exponential intensity decay is proportional to the surface roughness. Thus, by fitting the data with the LEPTOS software package the thickness and roughness values of the layers of the investigated samples can be extracted.

A.4.2. Atomic force microscopy

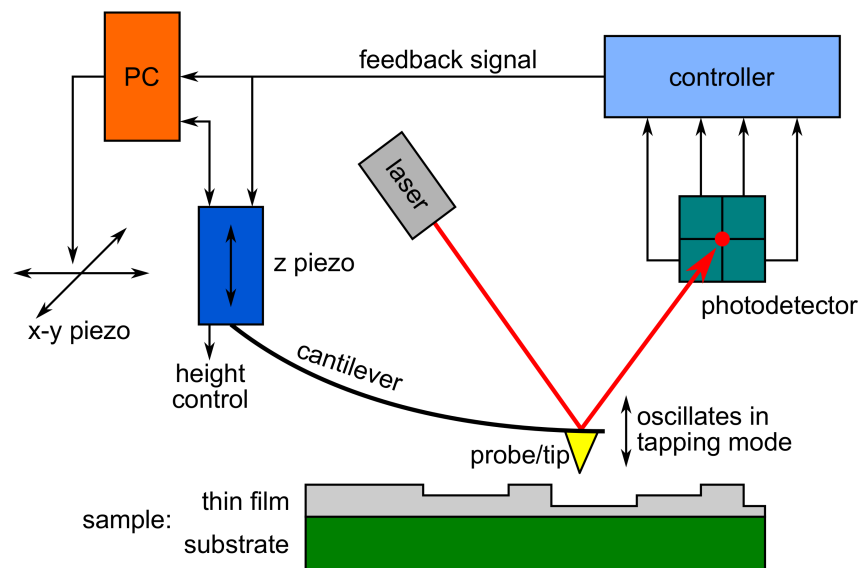


Figure A.4.2.: Schematic of an atomic force microscope (AFM). The tip of the cantilever moves over the sample surface and the deflection is measured by a photodetector which gives a feedback signal to the height control. The data are analyzed with the PC. Figure taken from Ref. [63].

With the atomic force microscopy (AFM) the roughness of a sample can be precisely determined. In this thesis the AFM from Nanosurf is used. Moreover, very small distances between different structures can be measured using such a device. In Fig. A.4.2 the experimental setup of an AFM is shown. It consists of a cantilever, which is connected to a height control. Moreover, a laser spot is focused on the backside of the tip of the cantilever. The reflection of the laser is measured by a photodetector. The sample is placed on a movable stage. For the measurement the stage is moved by the x - y piezo and thus the sample moves underneath the cantilever. The maximal measurement area is $100 \times 100 \mu\text{m}^2$. Due to the slight height differences on the sample surface, the cantilever is deflected. This deflection is measured in the photodetector as a change in phase and amplitude. Moreover the height plot is done with the data of the z -piezo, which readjusts the height of the cantilever to match the so called set point of the amplitude. In this thesis two different modes were used. Tapping mode, where the cantilever is not actually touching the sample surface, but oscillates above the sample due to attractive and repulsive forces. The other mode is the contact mode. In this mode as the name suggests, the tip of the cantilever touches the surface of the sample. Therefore, the contact mode is much more accurate when determining the roughness of a sample. However, if there are large steps expected on the sample and the difference in height is too large, the cantilever might get damaged. Therefore, in this case the tapping mode is beneficial.

A.4.3. Electron-beam lithography

The principle of the fabrication of structures using the electron-beam lithography is very similar to the optical lithography discussed in Chapter 3. The main difference is the electron beam used as exposure of the resist. Therefore, we used in this thesis a resist stack of PMMA-Electra92/PMMA 950K/PMMA 600K. All layers are spin coated at 4000 rpm for 1 min with subsequent baking step at 170 °C for 5 min for the 600 K and 900 K resist, whereas a temperature of 90 °C for 2 min is used for the Electra 92 resist layer. For the writing process a base dose of 5.6 Cm⁻² is used. The development time is 120 s.

A.4.4. SQUID-magnetometry

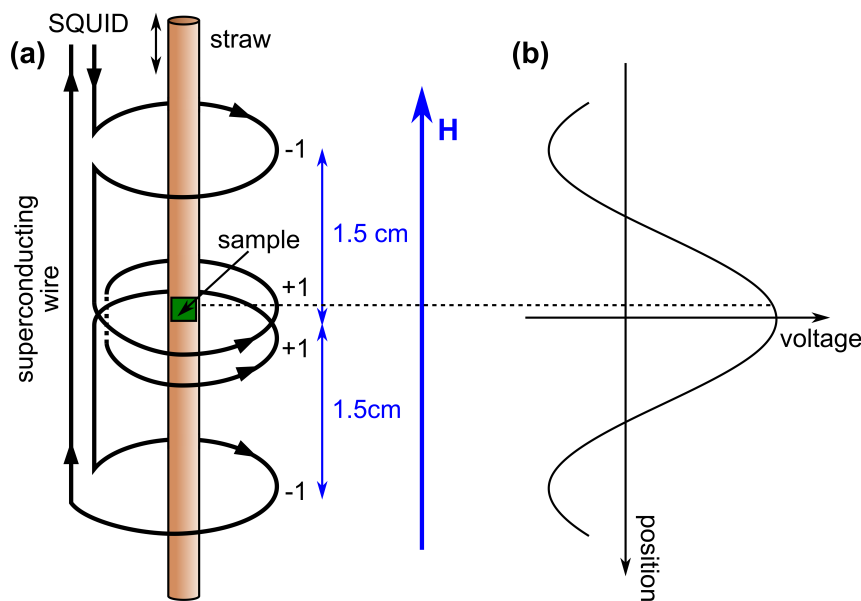


Figure A.4.3.: (a) Illustration of the detection coils of the SQUID magnetometry setup. The outer coils are wound clockwise, whereas the center one is counter-clockwise (second order gradiometer). During the measurement the sample is moved up and down in the coil setup. The applied magnetic field \mathbf{H} is always parallel to the straw. (b) Induced voltage of a paramagnetic or ferromagnetic sample with respect to its position. From this the magnetic moment is determined by fitting the voltage versus position curve. Figure taken from Ref. [63].

The magnetization hysteresis curves are measured using a superconducting quantum interference device (SQUID) magnetometer from Quantum Design. A schematic of the detection setup is shown in Fig. A.4.3. The sample is glued into a straw. This is moved in between the superconducting detection coils. There the outer coils have only one turn and the coil in the middle has two turns. Moreover, the turns on the outside are oriented opposite to the ones in the middle (second order gradiometer). The sample induces a current in the coils, which is converted into a voltage. The magnetic moment is determined by fitting the voltage versus position curve by the software from Quantum design. The

magnetization is then calculated by

$$M = \frac{m}{V} \quad (\text{A.6})$$

where V is the volume of the magnetic material. The magnetic field in the system can be swept from $\mu_0 H = 7 \text{ T}$ to $\mu_0 H = -7 \text{ T}$ at temperatures between 1.8 K and 400 K.

A.4.5. Ferromagnetic resonance (FMR) measurements

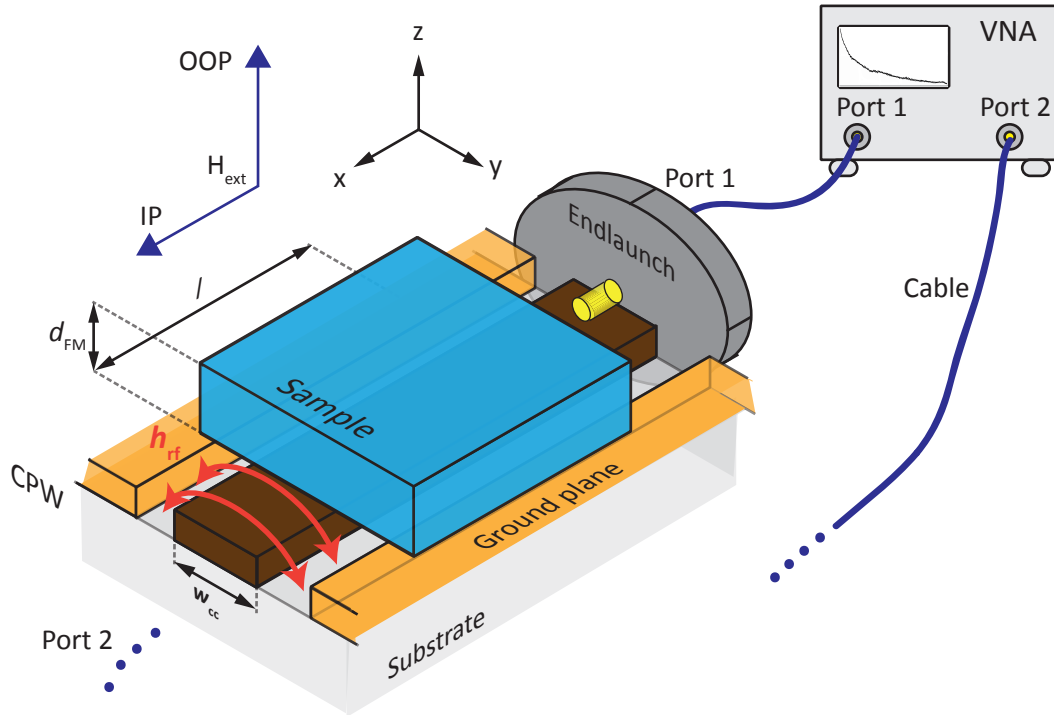


Figure A.4.4.: Schematic of the setup used for the FMR measurement. The oscillatory field \mathbf{h}_{rf} is applied on the middle conductor. The external magnetic field \mathbf{H}_{ext} can be applied in the film plane (ip) or out of the film plane (oop). The VNA is connected to the middle conductor and the absorbed energy is measured. Figure taken from Ref. [49].

For the measurement of the broadband FMR response, the sample is placed on a coplanar waveguide (CPW), as depicted in Fig. A.4.4. The CPW is connected to a vector network analyzer (VNA), which allows to determine amplitude as well as phase information. The CPW is placed in an external magnetic field \mathbf{H} and the necessary oscillatory field \mathbf{h}_{rf} is created by the conductor in the middle of the CPW. This middle conductor is connected to port 1 of the VNA, whereas the end of it is connected to port 2. The measured quantity in this experiment is the complex transmission S_{21} , which represents the voltage between port 1 and port 2 of the VNA. For a detailed description of the data processing refer to Ref. [49]. The experiments in this work were done with the external magnetic field \mathbf{H}_{ext} pointing in the out-of-plane (oop) direction.

Bibliography

- [1] J. Bardeen and W. Brattain, "The Transistor, A Semiconductor Triode", *Proceedings of the IEEE*, vol. 86, no. 1, pp. 29–30, Jan. 1998. DOI: 10.1109/JPROC.1998.658753.
- [2] G. E. Moore, "Cramming more components onto integrated circuits, Reprinted from *Electronics*, volume 38, number 8, April 19, 1965, pp.114 ff.", *IEEE Solid-State Circuits Society Newsletter*, vol. 11, no. 3, pp. 33–35, Sep. 2006. DOI: 10.1109/N-SSC.2006.4785860.
- [3] F. Ulaby, "The Legacy of Moore's Law", *Proceedings of the IEEE*, vol. 94, no. 7, pp. 1251–1252, Jul. 2006. DOI: 10.1109/JPROC.2006.876941.
- [4] Y. Liu, C. Zeng, J. Zhong, J. Ding, Z. M. Wang, and Z. Liu, "Spintronics in Two-Dimensional Materials", en, *Nano-Micro Letters*, vol. 12, no. 1, p. 93, Dec. 2020. DOI: 10.1007/s40820-020-00424-2.
- [5] R. Shankar, *Principles of quantum mechanics*, 2nd ed. New York: Plenum Press, 1994.
- [6] G. Binasch, P. Grünberg, F. Saurenbach, and W. Zinn, "Enhanced magnetoresistance in layered magnetic structures with antiferromagnetic interlayer exchange", en, *Physical Review B*, vol. 39, no. 7, pp. 4828–4830, Mar. 1989. DOI: 10.1103/PhysRevB.39.4828.
- [7] M. N. Baibich, J. M. Broto, A. Fert, F. N. Van Dau, F. Petroff, P. Etienne, G. Creuzet, A. Friederich, and J. Chazelas, "Giant Magnetoresistance of (001)Fe/(001)Cr Magnetic Superlattices", en, *Physical Review Letters*, vol. 61, no. 21, pp. 2472–2475, Nov. 1988. DOI: 10.1103/PhysRevLett.61.2472.
- [8] P. Khunkitti, K. Pituso, N. Chaiduangstri, and A. Siritaratiwat, "Optimal Sizing of CPP-GMR Read Sensors for Magnetic Recording Densities of 1–4 Tb/in²", *IEEE Access*, vol. 9, pp. 130758–130766, 2021. DOI: 10.1109/ACCESS.2021.3114598.
- [9] C. Kittel, "On the Theory of Ferromagnetic Resonance Absorption", en, *Physical Review*, vol. 73, no. 2, pp. 155–161, Jan. 1948. DOI: 10.1103/PhysRev.73.155.
- [10] M. Farle, "Ferromagnetic resonance of ultrathin metallic layers", *Reports on Progress in Physics*, vol. 61, no. 7, pp. 755–826, Jul. 1998. DOI: 10.1088/0034-4885/61/7/001.

-
- [11] K. Ganzhorn, J. Barker, R. Schlitz, B. A. Piot, K. Ollefs, F. Guillou, F. Wilhelm, A. Rogalev, M. Opel, M. Althammer, S. Geprägs, H. Huebl, R. Gross, G. E. W. Bauer, and S. T. B. Goennenwein, "Spin Hall magnetoresistance in a canted ferrimagnet", en, *Physical Review B*, vol. 94, no. 9, p. 094 401, Sep. 2016, Number: 9. DOI: 10 . 1103 / PhysRevB . 94 . 094401.
- [12] Y.-T. Chen, S. Takahashi, H. Nakayama, M. Althammer, S. T. B. Goennenwein, E. Saitoh, and G. E. W. Bauer, "Theory of spin Hall magnetoresistance", en, *Physical Review B*, vol. 87, no. 14, p. 144 411, Apr. 2013. DOI: 10 . 1103 / PhysRevB . 87 . 144411.
- [13] S. Meyer, M. Althammer, S. Geprägs, M. Opel, R. Gross, and S. T. B. Goennenwein, "Temperature dependent spin transport properties of platinum inferred from spin Hall magnetoresistance measurements", en, *Applied Physics Letters*, vol. 104, no. 24, p. 242 411, Jun. 2014, Number: 24. DOI: 10 . 1063 / 1 . 4885086.
- [14] M. Althammer, S. Meyer, H. Nakayama, M. Schreier, S. Altmannshofer, M. Weiler, H. Huebl, S. Geprägs, M. Opel, R. Gross, D. Meier, C. Klewe, T. Kuschel, J.-M. Schmalhorst, G. Reiss, L. Shen, A. Gupta, Y.-T. Chen, G. E. W. Bauer, E. Saitoh, and S. T. B. Goennenwein, "Quantitative study of the spin Hall magnetoresistance in ferromagnetic insulator/normal metal hybrids", en, *Physical Review B*, vol. 87, no. 22, p. 224 401, Jun. 2013, Number: 22. DOI: 10 . 1103 / PhysRevB . 87 . 224401.
- [15] H. Nakayama, M. Althammer, Y.-T. Chen, K. Uchida, Y. Kajiwara, D. Kikuchi, T. Ohtani, S. Geprägs, M. Opel, S. Takahashi, R. Gross, G. E. W. Bauer, S. T. B. Goennenwein, and E. Saitoh, "Spin Hall Magnetoresistance Induced by a Nonequilibrium Proximity Effect", en, *Physical Review Letters*, vol. 110, no. 20, p. 206 601, May 2013. DOI: 10 . 1103 / PhysRevLett . 110 . 206601.
- [16] E. Saitoh, M. Ueda, H. Miyajima, and G. Tatara, "Conversion of spin current into charge current at room temperature: Inverse spin-Hall effect", en, *Applied Physics Letters*, vol. 88, no. 18, p. 182 509, May 2006. DOI: 10 . 1063 / 1 . 2199473.
- [17] S. T. B. Goennenwein, R. Schlitz, M. Pernpeintner, K. Ganzhorn, M. Althammer, R. Gross, and H. Huebl, "Non-local magnetoresistance in YIG/Pt nanostructures", en, *Applied Physics Letters*, vol. 107, no. 17, p. 172 405, Oct. 2015, Number: 17. DOI: 10 . 1063 / 1 . 4935074.
- [18] V. Cherepanov, I. Kolokolov, and V. L'vov, "The Saga of YIG: Spectra, Thermodynamics, Interaction and Relaxation of Magnons in a Complex Magnet", vol. Physics reports, no. North-Holland, 1993.
- [19] L. J. Cornelissen, J. Liu, R. A. Duine, J. B. Youssef, and B. J. van Wees, "Long-distance transport of magnon spin information in a magnetic insulator at room temperature", en, *Nature Physics*, vol. 11, no. 12, pp. 1022–1026, Dec. 2015. DOI: 10 . 1038 / nphys3465.

- [20] C. Y. Guo, C. H. Wan, W. Q. He, M. K. Zhao, Z. R. Yan, Y. W. Xing, X. Wang, P. Tang, Y. Z. Liu, S. Zhang, Y. W. Liu, and X. F. Han, “A nonlocal spin Hall magnetoresistance in a platinum layer deposited on a magnon junction”, en, *Nature Electronics*, vol. 3, no. 6, pp. 304–308, Jun. 2020. DOI: 10.1038/s41928-020-0425-9.
- [21] J. Gückelhorn, T. Wimmer, M. Müller, S. Geprägs, H. Hübl, R. Gross, and M. Althammer, “Magnon transport in $\text{Y}_3\text{Fe}_5\text{O}_{12}$ /Pt nanostructures with reduced effective magnetization”, en, *arXiv:2108.03263 [cond-mat]*, Aug. 2021, arXiv: 2108.03263.
- [22] J. Gückelhorn, T. Wimmer, S. Geprägs, H. Huebl, R. Gross, and M. Althammer, “Quantitative comparison of magnon transport experiments in three-terminal YIG/Pt nanostructures acquired via dc and ac detection techniques”, en, *Applied Physics Letters*, vol. 117, no. 18, p. 182401, Nov. 2020. DOI: 10.1063/5.0023307.
- [23] K. S. Das, F. Feringa, M. Middelkamp, B. J. van Wees, and I. J. Vera-Marun, “Modulation of magnon spin transport in a magnetic gate transistor”, en, *Physical Review B*, vol. 101, no. 5, p. 054436, Feb. 2020. DOI: 10.1103/PhysRevB.101.054436.
- [24] T. Wimmer, M. Althammer, L. Liensberger, N. Vlietstra, S. Geprägs, M. Weiler, R. Gross, and H. Huebl, “Spin Transport in a Magnetic Insulator with Zero Effective Damping”, en, *Physical Review Letters*, vol. 123, no. 25, p. 257201, Dec. 2019. DOI: 10.1103/PhysRevLett.123.257201.
- [25] N. Thiery, V. V. Naletov, L. Vila, A. Marty, A. Brenac, J.-F. Jacquot, G. de Loubens, M. Viret, A. Anane, V. Cros, J. Ben Youssef, N. Beaulieu, V. E. Demidov, B. Divinskiy, S. O. Demokritov, and O. Klein, “Electrical properties of epitaxial yttrium iron garnet ultrathin films at high temperatures”, en, *Physical Review B*, vol. 97, no. 6, p. 064422, Feb. 2018. DOI: 10.1103/PhysRevB.97.064422.
- [26] K. Ganzhorn, S. Klingler, T. Wimmer, S. Geprägs, R. Gross, H. Huebl, and S. T. B. Goennenwein, “Magnon-based logic in a multi-terminal YIG/Pt nanostructure”, en, *Applied Physics Letters*, vol. 109, no. 2, p. 022405, Jul. 2016. DOI: 10.1063/1.4958893.
- [27] A. V. Chumak, A. A. Serga, and B. Hillebrands, “Magnon transistor for all-magnon data processing”, en, *Nature Communications*, vol. 5, no. 1, p. 4700, Dec. 2014. DOI: 10.1038/ncomms5700.
- [28] A. Hamadeh, O. d’Allivy Kelly, C. Hahn, H. Meley, R. Bernard, A. H. Molpeceres, V. V. Naletov, M. Viret, A. Anane, V. Cros, S. O. Demokritov, J. L. Prieto, M. Muñoz, G. de Loubens, and O. Klein, “Full Control of the Spin-Wave Damping in a Magnetic Insulator Using Spin-Orbit Torque”, en, *Physical Review Letters*, vol. 113, no. 19, p. 197203, Nov. 2014. DOI: 10.1103/PhysRevLett.113.197203.

- [29] H. Yu, O. d'Allivy Kelly, V. Cros, R. Bernard, P. Bortolotti, A. Anane, F. Brandl, R. Huber, I. Stasinopoulos, and D. Grundler, "Magnetic thin-film insulator with ultra-low spin wave damping for coherent nanomagnonics", en, *Scientific Reports*, vol. 4, no. 1, p. 6848, May 2015. DOI: 10.1038/srep06848.
- [30] F. Czeschka, "Spin Currents in Metallic Nanostructures", de, Ph.D. dissertation, TU Munich, 2011.
- [31] T. Wimmer, "Control and Manipulation of Magnonic Spin Currents in Magnetic Insulators", en, PhD thesis, TU Munich, 2021.
- [32] T. Wimmer, "Spin Transport in Magnetic Nanostructures", en, M.S. thesis, TU Munich, 2016.
- [33] M. Schreier, G. E. W. Bauer, V. I. Vasyuchka, J. Flipse, K.-i. Uchida, J. Lotze, V. Lauer, A. V. Chumak, A. A. Serga, S. Daimon, T. Kikkawa, E. Saitoh, B. J. van Wees, B. Hillebrands, R. Gross, and S. T. B. Goennenwein, "Sign of inverse spin Hall voltages generated by ferromagnetic resonance and temperature gradients in yttrium iron garnet platinum bilayers", *Journal of Physics D: Applied Physics*, vol. 48, no. 2, p. 025001, Jan. 2015. DOI: 10.1088/0022-3727/48/2/025001.
- [34] Michael Victor Berry, "Quantal phase factors accompanying adiabatic changes", en, *Proceedings of the Royal Society of London. A. Mathematical and Physical Sciences*, vol. 392, no. 1802, pp. 45–57, Mar. 1984. DOI: 10.1098/rspa.1984.0023.
- [35] J. Smit, "The spontaneous hall effect in ferromagnetics I", en, *Physica*, vol. 21, no. 6-10, pp. 877–887, Jan. 1955. DOI: 10.1016/S0031-8914(55)92596-9.
- [36] J. Smit, "The spontaneous hall effect in ferromagnetics II", en, *Physica*, vol. 24, no. 1-5, pp. 39–51, Jan. 1958. DOI: 10.1016/S0031-8914(58)93541-9.
- [37] L. Berger, "Side-Jump Mechanism for the Hall Effect of Ferromagnets", en, *Physical Review B*, vol. 2, no. 11, pp. 4559–4566, Dec. 1970. DOI: 10.1103/PhysRevB.2.4559.
- [38] S. R. Marmion, M. Ali, M. McLaren, D. A. Williams, and B. J. Hickey, "Temperature dependence of spin Hall magnetoresistance in thin YIG/Pt films", en, *Physical Review B*, vol. 89, no. 22, p. 220404, Jun. 2014. DOI: 10.1103/PhysRevB.89.220404.
- [39] C. Hahn, G. de Loubens, O. Klein, M. Viret, V. V. Naletov, and J. Ben Youssef, "Comparative measurements of inverse spin Hall effects and magnetoresistance in YIG/Pt and YIG/Ta", en, *Physical Review B*, vol. 87, no. 17, p. 174417, May 2013. DOI: 10.1103/PhysRevB.87.174417.
- [40] M. Aldosary, J. Li, C. Tang, Y. Xu, J.-G. Zheng, K. N. Bozhilov, and J. Shi, "Platinum/yttrium iron garnet inverted structures for spin current transport", en, *Applied Physics Letters*, vol. 108, no. 24, p. 242401, Jun. 2016. DOI: 10.1063/1.4953454.
- [41] F. P. Witek, "Spin Hall Magnetoresistive Noise", M.S. thesis, TU Munich, 2013.

- [42] N. Vlietstra, J. Shan, V. Castel, B. J. van Wees, and J. Ben Youssef, "Spin-Hall magnetoresistance in platinum on yttrium iron garnet: Dependence on platinum thickness and in-plane/out-of-plane magnetization", en, *Physical Review B*, vol. 87, no. 18, p. 184421, May 2013. DOI: 10.1103/PhysRevB.87.184421.
- [43] L. J. Cornelissen, K. J. H. Peters, G. E. W. Bauer, R. A. Duine, and B. J. van Wees, "Magnon spin transport driven by the magnon chemical potential in a magnetic insulator", en, *Physical Review B*, vol. 94, no. 1, p. 014412, Jul. 2016. DOI: 10.1103/PhysRevB.94.014412.
- [44] T. McGuire and R. Potter, "Anisotropic magnetoresistance in ferromagnetic 3d alloys", en, *IEEE Transactions on Magnetics*, vol. 11, no. 4, pp. 1018–1038, Jul. 1975. DOI: 10.1109/TMAG.1975.1058782.
- [45] J. Xiao, G. E. W. Bauer, K.-c. Uchida, E. Saitoh, and S. Maekawa, "Theory of magnon-driven spin Seebeck effect", en, *Physical Review B*, vol. 81, no. 21, p. 214418, Jun. 2010. DOI: 10.1103/PhysRevB.81.214418.
- [46] K. Ganzhorn, T. Wimmer, J. Cramer, R. Schlitz, S. Geprägs, G. Jakob, R. Gross, H. Huebl, M. Kläui, and S. T. B. Goennenwein, "Temperature dependence of the non-local spin Seebeck effect in YIG/Pt nanostructures", en, *AIP Advances*, vol. 7, no. 8, p. 085102, Aug. 2017, Number: 8. DOI: 10.1063/1.4986848.
- [47] M. Schreier, A. Kamra, M. Weiler, J. Xiao, G. E. W. Bauer, R. Gross, and S. T. B. Goennenwein, "Magnon, phonon, and electron temperature profiles and the spin Seebeck effect in magnetic insulator/normal metal hybrid structures", en, *Physical Review B*, vol. 88, no. 9, p. 094410, Sep. 2013. DOI: 10.1103/PhysRevB.88.094410.
- [48] M. Schreier, N. Roschewsky, E. Dobler, S. Meyer, H. Huebl, R. Gross, and S. T. B. Goennenwein, "Current heating induced spin Seebeck effect", en, *Applied Physics Letters*, vol. 103, no. 24, p. 242404, Dec. 2013. DOI: 10.1063/1.4839395.
- [49] L. Flacke, "Spin-Pumping and Spin Wave Damping in Co₂₅Fe₇₅ Thin-Film Heterostructures", en, M.S. thesis, TU Munich, 2018.
- [50] T. Gilbert, "Classics in Magnetism A Phenomenological Theory of Damping in Ferromagnetic Materials", en, *IEEE Transactions on Magnetics*, vol. 40, no. 6, pp. 3443–3449, Nov. 2004. DOI: 10.1109/TMAG.2004.836740.
- [51] H. Maier-Flaig, S. T. B. Goennenwein, R. Ohshima, M. Shiraishi, R. Gross, H. Huebl, and M. Weiler, "Note: Derivative divide, a method for the analysis of broadband ferromagnetic resonance in the frequency domain", en, *Review of Scientific Instruments*, vol. 89, no. 7, p. 076101, Jul. 2018. DOI: 10.1063/1.5045135.
- [52] S. P. Pati and Y. Endo, "Enhanced Low-Temperature Interfacial Gilbert Damping in Pt/YIG/Pt Trilayer Structures", en, *IEEE Transactions on Magnetics*, vol. 55, no. 2, pp. 1–4, Feb. 2019. DOI: 10.1109/TMAG.2018.2863678.

- [53] M. Akyol, N. Demiryurek, O. Iloglu, K. U. Tumen, F. Karadag, and A. Ekicibil, "Structural, magnetic and optical properties of Au/YIG, YIG/Au and Au/YIG/Au multilayer thin film stacks", en, *Journal of Magnetism and Magnetic Materials*, vol. 493, p. 165704, Jan. 2020. DOI: 10.1016/j.jmmm.2019.165704.
- [54] R. Ramos, T. Kikkawa, A. Anadón, I. Lucas, T. Niizeki, K. Uchida, P. A. Algarabel, L. Morellón, M. H. Aguirre, M. R. Ibarra, and E. Saitoh, "Interface-induced anomalous Nernst effect in Fe_3O_4 /Pt-based heterostructures", en, *Applied Physics Letters*, vol. 114, no. 11, p. 113902, Mar. 2019. DOI: 10.1063/1.5063553.
- [55] T. Nozue, T. Kikkawa, T. Watamura, T. Niizeki, R. Ramos, E. Saitoh, and H. Murakami, "Fabrication of yttrium-iron-garnet/Pt multilayers for the longitudinal spin Seebeck effect", en, *Applied Physics Letters*, vol. 113, no. 26, p. 262402, Dec. 2018. DOI: 10.1063/1.5046977.
- [56] J. Li, Y. Xu, M. Aldosary, C. Tang, Z. Lin, S. Zhang, R. Lake, and J. Shi, "Observation of magnon-mediated current drag in Pt/yttrium iron garnet/Pt(Ta) trilayers", en, *Nature Communications*, vol. 7, no. 1, p. 10858, Apr. 2016, Number: 1. DOI: 10.1038/ncomms10858.
- [57] S. Geprägs, C. Klewe, S. Meyer, D. Graulich, F. Schade, M. Schneider, S. Francoual, S. P. Collins, K. Ollefs, F. Wilhelm, A. Rogalev, Y. Joly, S. T. B. Goennenwein, M. Opel, T. Kuschel, and R. Gross, "Static magnetic proximity effects and spin Hall magnetoresistance in Pt / $\text{Y}_3\text{Fe}_5\text{O}_{12}$ and inverted $\text{Y}_3\text{Fe}_5\text{O}_{12}$ / Pt bilayers", en, *Physical Review B*, vol. 102, no. 21, p. 214438, Dec. 2020. DOI: 10.1103/PhysRevB.102.214438.
- [58] P. Schwenke, "Schnelles thermisches Tempern von Pt | $\text{Y}_3\text{Fe}_5\text{O}_{12}$ Heterostrukturen", de, Bachelor's thesis, TU Munich, Jul. 2019.
- [59] T. E. Gage, P. Dulal, P. A. Solheid, D. J. Flannigan, and B. J. H. Stadler, "Si-integrated ultrathin films of phase-pure $\text{Y}_3\text{Fe}_5\text{O}_{12}$ (YIG) via novel two-step rapid thermal anneal", en, *Materials Research Letters*, vol. 5, no. 6, pp. 379–385, Nov. 2017, Number: 6. DOI: 10.1080/21663831.2017.1295285.
- [60] C. Koch and T. J. Rinke, *Fotolithografie: Grundlagen der Mikrostrukturierung*, ger, 1. Auflage, M. GmbH, Ed. Ulm: MicroChemicals GmbH, 2017.
- [61] P. G. Evans, S. D. Marks, S. Geprägs, M. Dietlein, Y. Joly, M. Dai, J. Hu, L. Bouchenoire, P. B. J. Thompson, T. U. Schüllli, M.-I. Richard, R. Gross, D. Carbone, and D. Mannix, "Resonant nanodiffraction x-ray imaging reveals role of magnetic domains in complex oxide spin caloritronics", en, *Science Advances*, vol. 6, no. 40, eaba9351, Oct. 2020. DOI: 10.1126/sciadv.aba9351.
- [62] C. Mang, "Spinstromexperimente mit vertikalen Platin | Yttrium-Eisen-Granat Heterostrukturen", de, Bachelor's thesis, TU Munich, 2020.

- [63] F. M. Schade, "Fabrication and Characterization of Y₃Fe₅O₁₂|Pt|Y₃Fe₅O₁₂ Trilayers for Spin Current Based Experiments", en, Bachelor's thesis, TU Munich, 2013.
- [64] S. Geller and M. Gilleo, "The crystal structure and ferrimagnetism of yttrium-iron garnet, Y₃Fe₂(FeO₄)₃", en, *Journal of Physics and Chemistry of Solids*, vol. 3, no. 1-2, pp. 30–36, Jan. 1957, Number: 1-2. DOI: 10.1016/0022-3697(57)90044-6.
- [65] S. Matsuura, "Investigation of Magnetoresistance Tuned by Interface States of YIG/Pt Heterostructures", en, M.S. thesis, TU Munich, 2017.
- [66] T. Kikkawa, M. Suzuki, R. Ramos, M. H. Aguirre, J. Okabayashi, K. Uchida, I. Lucas, A. Anadón, D. Kikuchi, P. A. Algarabel, L. Morellón, M. R. Ibarra, and E. Saitoh, "Interfacial ferromagnetism and atomic structures in high-temperature grown Fe₃O₄/Pt/Fe₃O₄ epitaxial trilayers", en, *Journal of Applied Physics*, vol. 126, no. 14, p. 143903, Oct. 2019. DOI: 10.1063/1.5125761.
- [67] R. Tiggelaar, R. Sanders, A. Groenland, and J. Gardeniers, "Stability of thin platinum films implemented in high-temperature microdevices", en, *Sensors and Actuators A: Physical*, vol. 152, no. 1, pp. 39–47, May 2009. DOI: 10.1016/j.sna.2009.03.017.
- [68] S. Altmannshofer, "Epitaxie und Charakterisierung von dünnen Schichten des ferromagnetischen Isolators Y₃Fe₅O₁₂", M.S. thesis, Hochschule München, Oct. 2012.
- [69] P. Hansen, P. Röschmann, and W. Tolksdorf, "Saturation magnetization of gallium-substituted yttrium iron garnet", en, *Journal of Applied Physics*, vol. 45, no. 6, pp. 2728–2732, Jun. 1974, Number: 6. DOI: 10.1063/1.1663657.
- [70] I. H. Solt, "Temperature Dependence of YIG Magnetization", en, *Journal of Applied Physics*, vol. 33, no. 3, pp. 1189–1191, Mar. 1962, Number: 3. DOI: 10.1063/1.1728651.
- [71] E. Popova, N. Keller, F. Jomard, L. Thomas, M.-C. Brianso, F. Gendron, M. Guyot, and M. Tessier, "Exchange coupling in ultrathin epitaxial yttrium iron garnet films", *The European Physical Journal B - Condensed Matter*, vol. 31, no. 1, pp. 69–74, Jan. 2003, Number: 1. DOI: 10.1140/epjb/e2003-00010-2.
- [72] V. V. Krishnamurthy, I. Zoto, G. J. Mankey, J. L. Robertson, S. Maat, E. E. Fullerton, I. Nwagwu, and J. K. Akujieze, "Antiferromagnetic phase transitions in an ordered Pt₃Fe (111) film studied by neutron diffraction", en, *Physical Review B*, vol. 70, no. 2, p. 024424, Jul. 2004, Number: 2. DOI: 10.1103/PhysRevB.70.024424.
- [73] E. Popova, N. Keller, F. Gendron, L. Thomas, M.-C. Brianso, M. Guyot, M. Tessier, and S. S. P. Parkin, "Perpendicular magnetic anisotropy in ultrathin yttrium iron garnet films prepared by pulsed laser deposition technique", en, *Journal of Vacuum Science & Technology A: Vacuum, Surfaces, and Films*, vol. 19, no. 5, pp. 2567–2570, Sep. 2001, Number: 5. DOI: 10.1116/1.1392395.

- [74] H. Yuasa, F. Nakata, R. Nakamura, and Y. Kurokawa, "Spin Seebeck coefficient enhancement by using Ta₅₀W₅₀ alloy and YIG/Ru interface", en, *Journal of Physics D: Applied Physics*, vol. 51, no. 13, p. 134002, Apr. 2018, Number: 13. DOI: 10.1088/1361-6463/aaaf89.
- [75] Z. H. Zhu, J. Stremper, R. R. Rao, J. Pelliciani, Y. Choi, T. Kawaguchi, H. You, J. F. Mitchell, Y. Shao-Horn, and R. Comin, "Anomalous Antiferromagnetism in Metallic RuO₂ Determined by Resonant X-ray Scattering", en, *Physical Review Letters*, vol. 122, no. 1, p. 017202, Jan. 2019, Number: 1 arXiv: 1806.02036. DOI: 10.1103/PhysRevLett.122.017202.
- [76] E. Milosevic, S. Kerdsonpanya, A. Zangiabadi, K. Barmak, K. R. Coffey, and D. Gall, "Resistivity size effect in epitaxial Ru(0001) layers", en, *Journal of Applied Physics*, vol. 124, no. 16, p. 165105, Oct. 2018, Number: 16. DOI: 10.1063/1.5046430.
- [77] V. Swamy, S. Mi, H. Huang, C. Mei, Y. Lu, D. Song, H. Du, and Y. Zhao, "Structural, Magnetic, and Low-Temperature Electrical Transport Properties of YIG Thin Films with Heavily Reduced Oxygen Contents", en, *ACS Applied Electronic Materials*, vol. 3, no. 8, pp. 3313–3320, Aug. 2021. DOI: 10.1021/acsaelm.1c00195.
- [78] R. Gross and A. Marx, *Festkörperphysik*, ger, 3. Auflage, ser. De Gruyter Studium. Berlin ; Boston: De Gruyter, 2018.

Acknowledgments

In the last year, while working on this thesis I learned a lot and got support in many different ways. Therefore, I would like to thank several people who made this work possible and gave me such a good time. In particular, I would like to thank:

Prof. Dr. Rudolf Gross, for giving me the opportunity to write my master's thesis at the Walther-Meißner Institut (WMI).

Dr. Stephan Geprägs as my advisor, for answering all my questions, no matter how stupid they seemed. The discussions with you helped me a lot to understand the physics behind the measurements and always pointed me in the right direction for the next steps. Your calm, kind and positive attitude even when things go wrong is one of a kind and significantly shaped the working atmosphere. Thank you for all the time and effort you invested in me and the repeated proof-reading of this thesis, even on weekends.

Manuel Müller, for showing me the FMR setup as well as performing the FMR measurements for me, the support regarding the SUPERBOWL system. Additionally, I would like to thank you for the physics and non-physics related discussions.

Janine Gückelhorn, for showing me how to use the SUPERBOWL system and helping me whenever I encountered any issues. Additionally, I would like to thank you for performing the electron-beam lithography step on one sample.

Moreover, I want to thank my fellow master colleagues, namely (in arbitrary order) Monika Scheufele, Niklas Bruckmoser, Leonhard Hölscher, Ramona Stumberger, Matthias Grammer, Johannes Schirk, Elisabeth Meidinger, Mayank Sharma, Maximilian Nägele, Korbinian Rubenbauer and Christopher Waas for all the fruitful discussions as well as joyful ice cream, cake, coffee and lunch breaks and even laughing at my really bad jokes, at least sometimes. It was a pleasure to work, laugh and at times get frustrated alongside you.

Andreas Haslberger, who took over some PLD and EVAP processes in his time as working student at WMI.

Leander Peis, for the morning and afternoon coffee "meetings".

Thomas Brenninger, for his fast technical support whenever a machine encountered issues.

All other unnamed members of WMI for the great and productive atmosphere.

My friends who did not necessarily contribute in any intellectual way but for reminding me at times that work is not everything in life and for supporting me in stressful times.

Last but definitely not least my family, especially my parents, for always supporting me emotionally and financially as well as encouraging me to follow my dreams and passion. I am very grateful for enabling me to study at the TU Munich.